ISSN 1068-3755, Surface Engineering and Applied Electrochemistry, 2008, Vol. 44, No. 5, pp. 343–352. © Allerton Press, Inc., 2008.
Original Russian Text © S.A. Silkin, E.A. Pasinkovskii, V.I. Petrenko, A.I. Dikusar, 2008, published in Elektronnaya Obrabotka Materialov, 2008, No. 5, pp. 4–14.

ELECTRICAL PRECISION TREATMENT OF MATERIALS

High Rate Anodic Dissolution in Chloride Solutions of Steel after Electrothermochemical Treatment

S. A. Silkin[a], E. A. Pasinkovskii[b], V. I. Petrenko[b], and A. I. Dikusar[a,b]

[a] *T.G. Shevchenko Dniestr State University, ul. 25 Oktyabrya 128, Tiraspol, Republic of Moldova*

[b] *Institute of Applied Physics, Academy of Sciences of Moldova, ul. Academiei 5, Kishinev, MD-2028 Republic of Moldova*

E-mail: dikusar@phys.asm.md

Received May 19, 2008

Abstract—High rate (up to 15 A/cm^2) anodic dissolution of St3 steel in chloride solutions (1–6 M NaCl) was investigated after its electrothermochemical al treatment (nitriding and thermal treatment). Various potential ranges (or current density ranges) can be emphasized: the region of anodic anion activation (sublimiting currents), the diffusion limitation area (caused by salt passivation), and the transpassive dissolution region. It is shown that the heat treatment influence is the most substantial in the region of salt passivation (or the limiting current region). The double role of the hydrodynamics is revealed during dissolution under these conditions: the influence of the ionic mass transfer rate in the solution and of the removal of the hard carbonaceous products produced as a result of the selective dissolution of the components of the nitrided steel. It is shown that, in sublimiting currents and transpassive dissolution ranges, the specific dissolution rate depends on the nitrogen content of the studied steel.

DOI: 10.3103/S1068375508050013

It is necessary to investigate the high rate anodic dissolution to control the processes of electrochemical machining (ECM) of metals and alloys [1, 2]. In most cases, this process occurs when a metal has previously been subjected to a specific thermal or chemical heat treatment. As is shown in some works (see, for example, [2–7]), such types of surface treatment substantially influence the ECM machinibility.

Anodic electrothermochemical treatment by the method of metal heating in electrolytes at rather high anodic potentials when the surface temperature ranges up to ~1000°C and saturating elements are transferred from the electrolyte into the treated electrode [5] is one of the types of thermal (and chemical heat) treatment.

The reasons for the interest in the regularities of the anodic dissolution of such objects are, first, the study of the regularities of the anodic dissolution of substances with the composition and properties changed with distance; second, the influence of the thermal treatment on the anodic dissolution rate; and, third, the effect of the saturating component (nitrogen, carbon, etc.) on the dissolution rate.

Ultimately, the results of such research permit one to solve the problems of controling the ECM processability (the treatment precision, the surface quality, and the process efficiency and power consumption) for surfaces treated previously using a certain kind of thermal or chemical heat treatment.

The results of investigation of the anodic dissolution of St3 steel in chloride solutions after electrothermochemical treatment in nitrate-containing electrolytes are presented in this work. It is known that, depending on the electrolyte composition and the regimes of the thermal treatment, it is possible both without nitriding and with nitriding [5]. It is evident that these results can be considered as modeling the process of anodic dissolution of both thermally treated (tempered) and nitrided steels. It should be particularly emphasized that, in the literature dedicated to the ECM processes, it is repeatedly noted that the rates of the anode treatment under the conditions of ECM of tempered steels, as a rule, exceed the rates of the untempered ones [6, p. 341].

EXPERIMENTAL TECHNIQUE

Electrothermochemical treatment. Electrothermochemical treatment (ETCT) of cylindrical specimens of St3 with a diameter of 4 mm and a height of ~50 mm is carried out using the *UHTO-5* installation manufactured by the experimental plant of the Institute of Applied Physics of the Academy of Sciences of Moldova in a 10% solution of NH_4Cl (thermal treatment) and in a 10% solution of NH_4Cl + 5% NH_4OH (nitriding).

In both cases, voltage from 150 to 180 V is applied to the specimen being worked, which is inserted into the electrolyte to a depth ~10 mm. A vapor-gas shell is generated with the temperature rising up to 650°C (U = 150 V), 700°C (U = 165 V), and 750°C (U = 180 V) with the treatment being conducted for 10 min. Then,

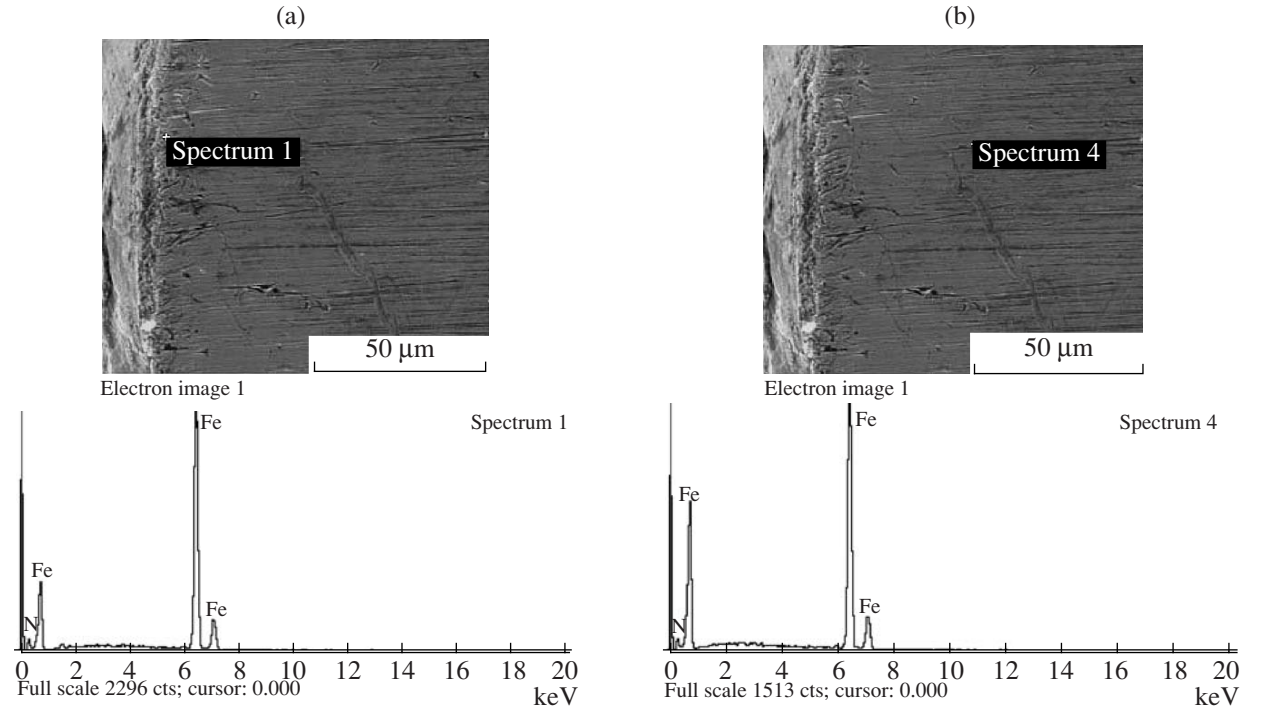

Element	wt, %	at %
N	1.55	5.90
Fe	98.45	94.10

Element	wt, %	at %
N	0.97	3.76
Fe	99.03	96.24

Fig. 1. Cut off of the surface of the steel nitrided at ETCT at a temperature of 700°C and the results of the EDX analysis of the surface layer. The analysis results correspond to distances from the surface of 3 (a) and 47 (b) μm.

the voltage is switched off, the shell collapses, and cooling occurs for 10 s.

The specimens were thermotreated at 750°C, whereas the nitriding was carried out under all the above mentioned conditions (650, 700, and 750°C).

Investigation of the anodic dissolution. Anodic dissolution of steel subjected to ETCT was studied by the method of a rotating disc electrode (RDE) in an electrochemical cell with a Lugin capillary in the variant used previously to research the processes of the high rate anodic dissolution [1, 7]. The anodic dissolution of the untreated St3, as well as the thermal processed and nitrided specimens, was performed in the range of current density from 0.1 to 15 A/cm^2 in 1–6 M solutions of NaCl at room temperature. With this aim, there were recorded the φ-τ curves (φ is the potential with relative to the saturated silver-chloride electrode, τ is the time) under galvanostatic conditions, potentiodynamic *i*-φ curves (*i* is the current density) at RDE rotation velocities of 260–2400 rev/min and potential change rate 100 mV/min as well as variation of the specific dissolution rate *q* (mg/C) potential (current density) changing under both potentiostatic and galvanostatic conditions. Values *q* were registered in accordance with the weight loss the given amount of electricity being passed. The obtained values were compared with the Faraday equivalent (0.29 mg/C at the dissolution of Fe with generation of Fe(II)).

The examination of the surface before and after treatment was conducted using scanning electron microscope TESCAN and the system of element composition estimation INCA Energy EDX.

A shear was made along the axis of the specimens subjected to nitriding and then the nitrogen content was measured at different distances from the surface with the help of the EDX-analysis (Fig. 1). The results of the nitrogen distribution in depth for different nitriding conditions are presented in Fig. 2.

The steel specimens before treatment contained of only Fe, after thermal treatment the surface was covered with oxide film of the approximate composition of the stochiometric one for Fe_2O_3 (Fig. 3). This film was friable and could be easily removed by grinding on the ordinary (non-rubbing) paper. Thus it was removed from the surface before the investigation of the anodic dissolution. The morphology and composition of the surface layer is presented in Fig. 4 as an example of the surface subjected to the anodic dissolution after minor mechanical processing (for the nitrided specimen).

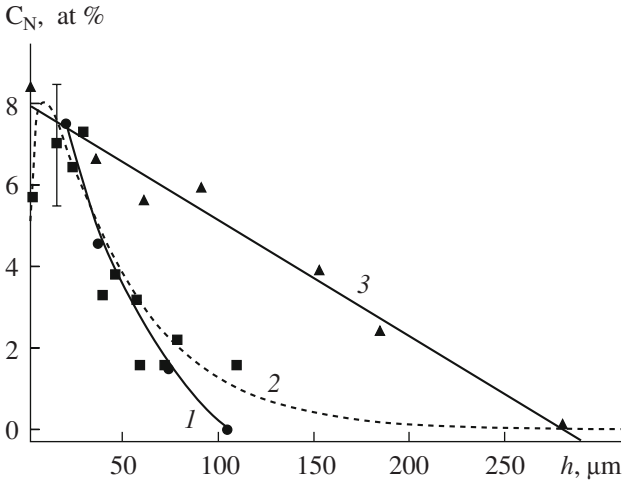

Fig. 2. Distribution of nitrogen through the depth of the specimen at different nitration regimes. *1*, 650; *2*, 700; *3*, 750°C.

RESULTS AND DISCUSSION

Peculiarities of Dissolution of Steel Not Subjected to Thermal Treatment and Nitriding

Potentiodynamic anodic polarization curves for treated and untreated steel are presented in Fig. 5. The presence of passivation (limiting current) range is typical for them. In the range of "sublimiting" current the dissolution rates for various specimens are similar, but they differ after reaching the limiting current. It is known (see for instance [1, 2, 4]) that the presence of the limiting current is caused by salt passivation attained at the equality of the dissolution product concentration and the saturation concentration in the ternary system: iron chloride–NaCl–H_2O. For RDE its value grows in proportion to $\sqrt{\omega}$ (ω is the RDE rotation velocity) and reduces in proportion to the growth of chloride ion concentration in the solution.

In [8] it is shown that it isn't influenced by the medium acidity. The relationship between the anode limiting current value $i_{\text{lim}}^{\text{a}}$ for Fe and chloride ion concentration in the solution is displayed in Fig. 6. This work results corrected for the RDE rotation velocity being 1000 rev/min and bulk temperature 25°C are presented in the same plot. The proper correction was carried out by reduction or increasing of the limiting current density in proportion to the quadratic root of the rotation velocity along with the temperature correction being about 5% of the limiting current density variation for 1°C of the bulk temperature change.

It is evident from the results, presented in Fig. 6, that St3 anodic dissolution limiting current density values are almost fully consistent with the results obtained previously for dissolution of Fe and Ni [8, 9].

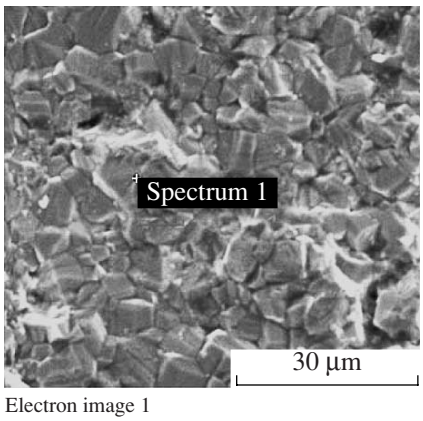

Electron image 1

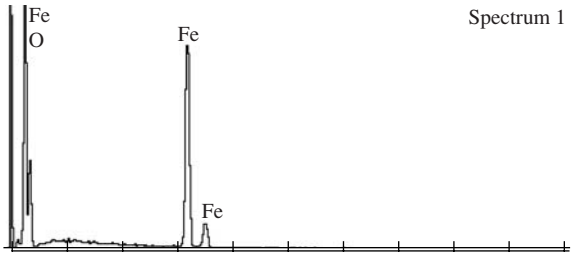

Full scale 1617 cts; cursor: 0.000

Element	wt, %	at %
O	31.17	61.25
Fe	68.83	38.75

Fig. 3. Micrograph (SEM) of the surface layer after ETCT (thermal treatment) and the surface layer composition.

The relationship between specific rate of the studied steel dissolution and the current density in the galvanostatic experiment is shown in Fig. 7.

It is seen that in the "sublimiting" current range the observed values completely correlate with faraday rate of dissolution 0.29 mg/C and at the transition into diffusion region and to transpassive dissolution there occurs the reduction of the rate (i.e. decrease current efficiency considering generation of Fe(II)). In other words in the "sublimiting" current range there is observed dissolution in conformity with the total electrode reaction

$$\text{Fe} \longrightarrow \text{Fe}^{2+} + 2\text{e} \qquad (1)$$

and $n_{\text{ef}} = 2$.

Equilibrium potential for reaction (1) $\varphi_{\text{eq}} = -0.44$ V (relatively saturated Ag/AgCl) [6]. The measured stationary potential was ~ –0.19 V testifying the potential being mixed (corrosive one). The increase of the current density caused the shift of the electrode potential into the anode region. In the diffusion region (the salt passivity region) the saturation concentration was reached in the system $FeCl_2$–NaCl– H_2O, and taking into account that φ for the reaction

$$\text{Fe} \longrightarrow \text{Fe}^{2+} + 3\text{e} \qquad (2)$$

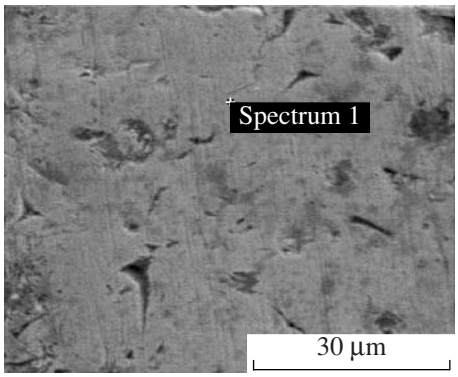

Electron image 1

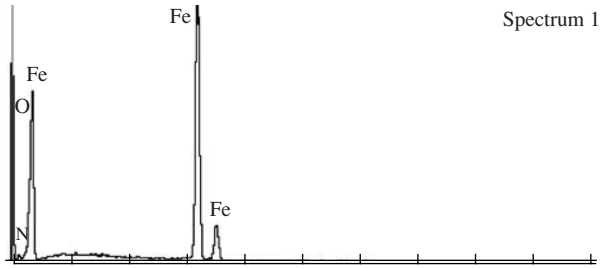

Full scale 2078 cts; cursor: 0.000

Element	wt, %	at %
N	0.50	1.98
O	0.11	0.38
Fe	99.38	97.64

Fig. 4. Micrograph (SEM) and results of the EDX analysis of the specimen after ETCT (nitration at 650°C) of the surface layer after the mechanical preparation of the surface.

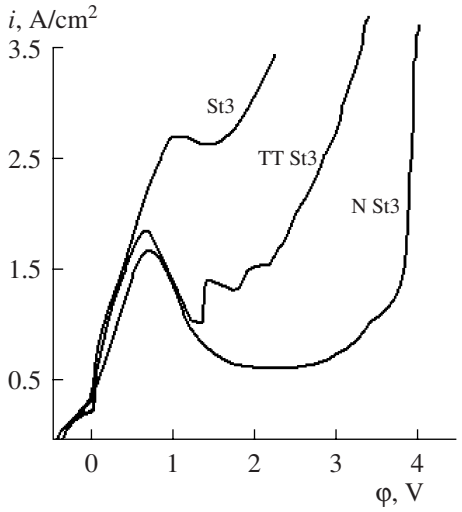

Fig. 5. Potentiodynamic polarization curves of dissolution of the initial thermally treated (TT) and nitrided (N) specimens in 2M NaCl at 20°C at an RDE rotation velocity of 1200 rev/min.

is –0.036 V [6] as well as the fact that $C^{sat}_{[FeCl_2–NaCl–H_2O]} < C^{sat}_{[FeCl_3–NaCl–H_2O]}$ [10] (C^{sat} is the saturation concentration in the respective ternary system with bi-and trivalent iron) the anodic potential being attained in the region of the dissolution diffusion control parallel with the ionization in accordance with scheme (1) it may be considered that there occurred also dissolution according to scheme (2) causing the reduction of the current efficiency (Fig. 7). This fact was observed repeatedly for such systems [1, 2, 4].

Along with the dissolution according to scheme (2) there was observed the generation of the surface oxides intensifying with the transition into the region of the transpassive dissolution as evidenced by the reduction of the latter specific rate (Fig. 7).

Galvanostatic Experiment. Generalized Polarization Curve

φ–τ relationships obtained for the nitrided steel dissolution (the ETCT first regime, saturation temperature 650°C) at RDE rotation velocity 2300 rev/min are presented in Fig. 8. It is seen that in the range of the "sublimiting" current the dissolution at $i = 0.2$ A/cm^2 occurs the constant potential ~ –0.1 V of relatively saturated Ag/AgCl electrode i.e. more negative than the equilibrium potential for reaction (2), and in the region of the oscillation control there are observed the potential oscillations the frequency of which decreases with

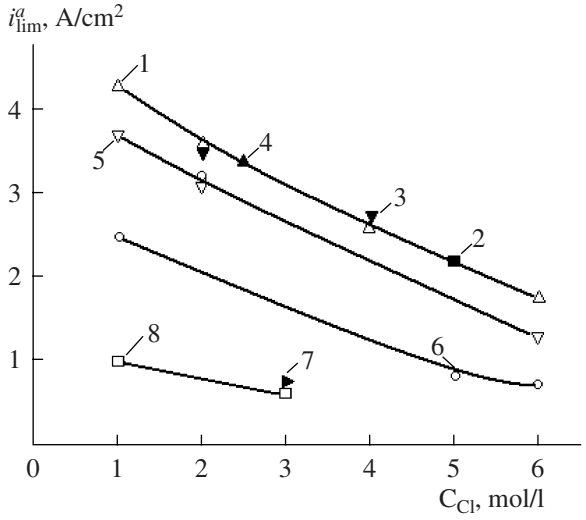

Fig. 6. Relationship between the limiting density of the anode current of the RDE at 1000 rev/min and 25°C and the concentration of chloride ion in the solution at anodic dissolution of Fe in HCl (*1*) [8], Fe in NaCl (*2*) [8], and Ni in NaCl (*4*) [9], as well as St3 (*3*, *5*–*8*) according to the results of this work: untreated (*3*), thermally treated (n = 2300 rev/min) (*5*), thermally treated (n = 280 rev/min) (*6*), freshly thermally treated (*7*) and freshly nitrided (*8*). Explanations are given in the text.

time, i.e. as moving away from the initial surface of the anodic dissolution and as the layer composition changes (see Fig. 2) (Fig. 8). For the observed oscillation process the measured potential growing up to the value ~3.0 V there happens its consequent abrupt drop accompanied by the separation of the black (carbonaceous [2, 11, 12]) film from the electrode surface.

Any noticeable effect of the thermal treatment and nitriding on the dissolution rate (current density) in the range of the "sublimiting" current (or the region of the anode activation by Cl^- ions according to [2]) is absent (Fig. 9). Similar result is realized in [11]. Yet in the region of the diffusion control it is substantial (Fig. 5).

In the range of the "sublimiting" current the nitrided steel dissolution rate can exceed faraday one (Fig. 10). And what is more there is observed distinctly pronounced dependence of the dissolution rate on the nitriding temperature (Fig. 10) testifying of the presence of a possible chemical reaction of the nitride dissolution in the acid medium (initiated by the anodic dissolution in conformity with scheme (1)). Dissolution according to scheme (1) suggests that acidation of the near-anode layer with formation of the hydrooxochlorocomplex takes place

$$Fe^{2+} + xH_2O + yCl^- = [Fe(OH)_xCl_y]^{2-x-y} + H^+. \quad (3)$$

In consequence of the near-electrode layer acidation it is possible the chemical reaction of the Fe nitride dissolution

$$FeN + 4H^+ \longrightarrow NH_4^+ + Fe^{3+}. \quad (4)$$

Obviously the presence of the chemical reaction (4) proceeding along with reaction (1) will increase the dissolution rate, and the more nitrogen concentration in steel the more is the rate; it is confirmed by the results, displayed in Fig. 10. Saturation temperature and hence nitrogen concentration in the surface layer influences the dissolution rate in the transpassive region too (Fig. 10).

Diffusion region. The Role of the Electrolyte Flow

In the region of diffusion control of the dissolution rate the thermal treatment and nitriding as a result of ETCT influence substantially the passivation current density (Fig. 5) with the increase (as it is evident from Fig. 11) of the RDE rotation velocity causing the growth of the salt passivation current value correlating qualitatively with the results of the previous investigations [1, 2, 4, 8, 9, 11, 12].

However more extended study of steel dissolution after ETCT at potentiostatic switching-on sat constant potential $\varphi = +1.4$ V in the wide range of chloride concentrations (1–6 M) and RDE rotation velocities showed the presence of significant peculiarities the influence of hydrodynamics both on the dissolution current density and the value of the material removal rate (the dissolution specific speed).

First, current values at $\varphi = 1.4$ V recorded at the ETCT initial dissolution (during preparation of the surface described above) and after several cycles of etching of the specimen (i.e. as the surface under working moves deep into the specimen) differ significantly (Fig. 12). It is observed that the limiting current density nearly doubled after removal about 100 μm of the preliminary ETCT treated surface. Second, dependence of i_{lim}^a on time differ greatly for relatively high and low speeds of

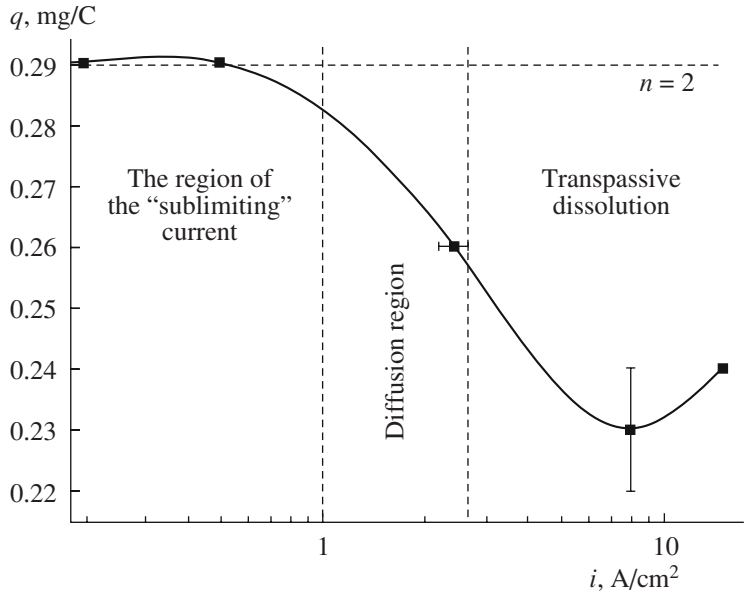

Fig. 7. The St3 specific dissolution rate—current density relationship in 2 M NaCl for different ranges of potentials (current densities).

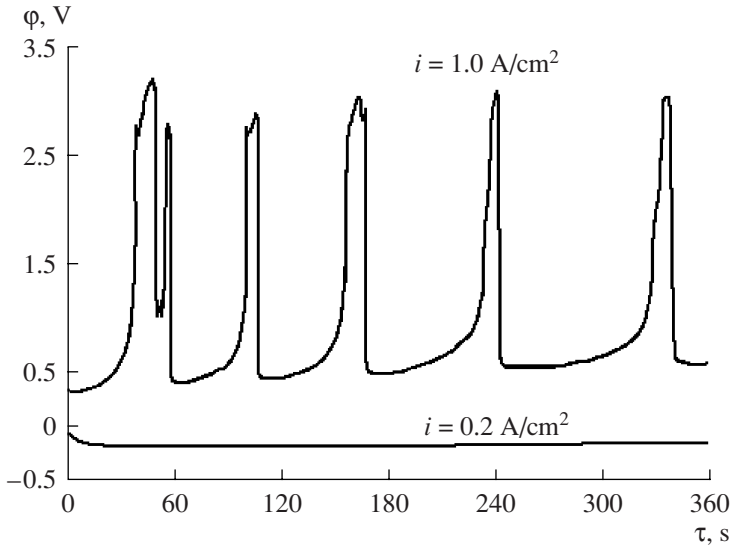

Fig. 8. The dissolution potential versus the time relationship for the nitrided St3 in 2 M NaCl at different current densities for the disc electrode rotating at 2300 rev/min and T = 18°C.

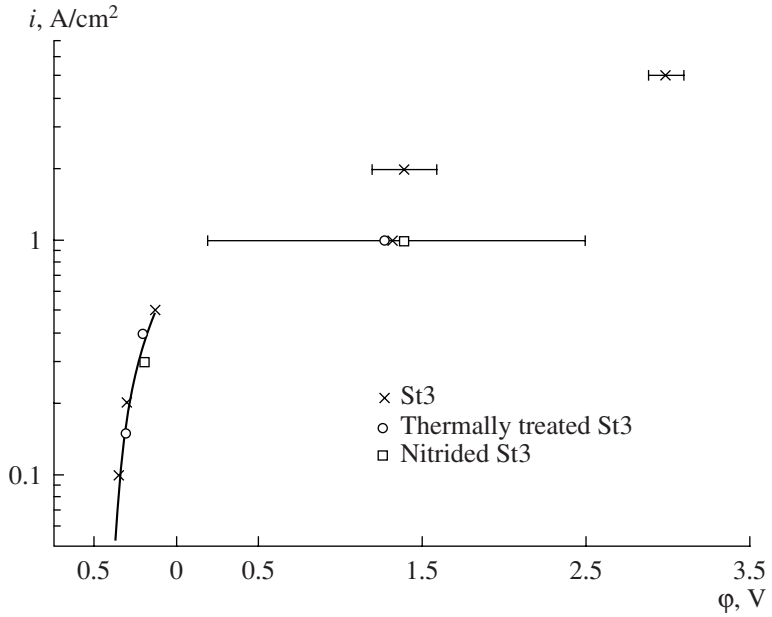

Fig. 9. Generalized galvanostatic polarization curve obtained in 2 M NaCl at 1000 rev/min and T = 18°C.

the RDE rotation (Fig. 13). At high speeds of mass transfer there occurs a pronounced oscillation process connected with repeating removal of the black carbonaceous film from the specimen surface with the respective current jump followed by its reduction (passivation). Data presented in Fig. 13 are obtained for 1 M solution but less pronounced similar effects of the hydrodynamics influence were observed for all concentrations of the solution except for 6 M solution not only for thermally treated specimens but nitrided too. At low speed of mass transfer the oscillation process didn't happen (Fig. 13) both for thermally treated (TT) and nitrided steels (NS).

Average values of a set of experiments after etching to the depth from ~30 to ~150 μm are presented in the

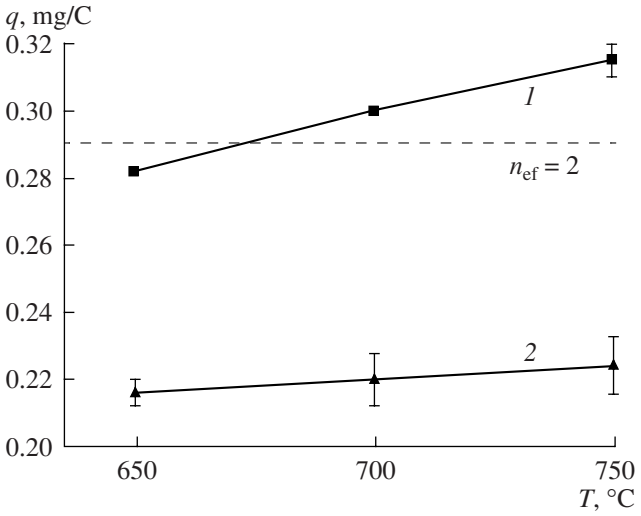

Fig. 10. Influence of the nitration temperature on the specific rate of dissolution of nitrided steels in 2 M NaCl at 260 rev/min and T = 18°C at dissolution in the range of "sublimiting" current (*1*) and in the transpassive region (5 A/cm^2) (*2*).

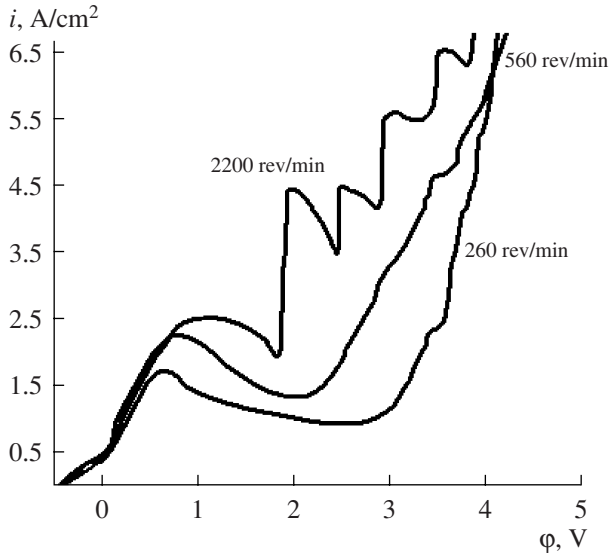

Fig. 11. Potentiodynamic polarization curves of anodic dissolution of thermally treated St3 in 1 M NaCl at different RDE rotation velocities.

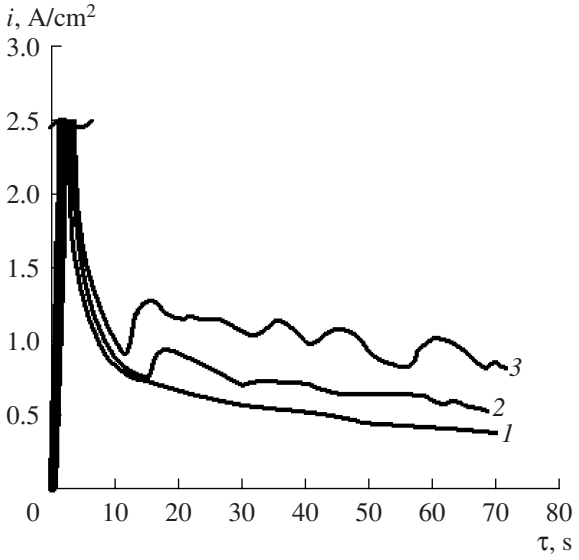

Fig. 12. Current density vs. time curver for the nitrided steel (T = 750°C) dissolution at φ = +1.4 V and an RDE rotation velocity of 260 rev/min in 1 M NaCl after the removal of a layer with a certain thickness, μm: *1*, 40, *2*, 80, and *3*, 120.

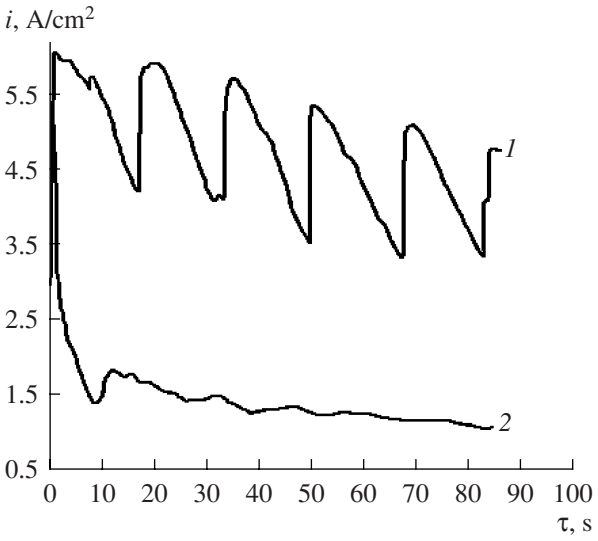

Fig. 13. Current density vs. time curver for the thermally treated St3 dissolution in 1 M NaCl at φ = + 1.4 V and an RDE rotation velocity of 280 rev/min (*1*) and 2300 rev/min (*2*) with T = 18°C.

table for NS. The average values of q for TT steels are obtained at the etching nearly to the same depth.

For the untreated steel in the diffusion control region the specific dissolution rate was ~0.26 mg/C (Fig. 7). Similar values of dissolution rates were observed for thermally treated and nitrided steels at φ = const in the diffusion region and RDE low rotation velocities (the table). At high rotation velocities the specific rate of the material removal grew in all cases (the table), that growth being outside the error of measurement.

It is ascertained that the diffusion current values for TT steels couldn't be corrected taking into account only

Specific dissolution rates q (mg/C) for the thermally treated steel and the nitrided one at different RDE rotation velocities under potentiostatic conditions (φ = 1.4 V)

Kind of material	n, rev/min	1 M NaCl	2 M NaCl	6 M NaCl	q_{av}, mg/C
TT	280	0.260	0.264	0.258	0.261 ± 0.002
	2300	0.281	0.291	0.292	0.288 ± 0.004
NS (750°C)	280	0.25 ± 0.01	–	–	–
	2300	0.30 ± 0.02	–	–	–

the relationship $i^a_{lim} = K\sqrt{\omega}$ with the constant magnitude of K (Fig. 6). In this case they "delaminate" the magnitudes of K being less for low velocities of mass transfer, i.e. when the oscillation process is absent.

More comprehensive examination of the deduced relationships (Fig. 6) shows that the magnitude of K depends not only on the mass transfer speed but on the etching depth (as for the nitrided specimens). Really the values i^a_{lim} for conditions marked as *5* and *6* in Fig. 6 differ from those marked as *7* and *8*. The last mentioned ones were obtained on "ETCT freshly worked" specimens and others on TT specimens a substantial part of which was removed by electrochemical etching and mechanical polishing. It is seen that the removal of a great part of the surface layer causes the growth of i^a_{lim} at the constant rotation velocity for the given chloride ion concentration in the solution.

It is significant that in the cases when the oscillation process is observed even at low rotation velocities the value of i^a_{lim} grows (Fig. 6, test for 2 M NaCl of TT specimen at 280 rev/min).

At the treatment under the oscillator conditions (the high speed of mass transfer) after dissolution there is seen a porous surface and at low rotation velocities the porosity is absent (Fig. 14).

The combination of all experimental data allows to suggest that the selectivity of dissolution of different phase components (specifically ferrite and cementite) at high mass transfer speeds and removal (disintegration) of a part of the layer because of the high tangential stresses at the intensive hydrodynamics is the cause of the observed effects.

The processes being relatively low intensive the surface salt film covers fully the electrode surface therefore the dissolution rate reduces as dissolution occurs only through the salt film.

In such cases, anomalous dependences of diffusion limiting current on the RDE rotation velocity (see for instance [13]) are possible and this is confirmed by the above described experiments. The partial desintegration of the specimen material under the oscillation mode is proved by the fact of an increase in the specific dissolution rate at intense hydrodynamics. This phenomenon is not observed in the range of sublimiting currents.

The analysis of the surface elemental composition after dissolution demonstrated significant distinctions at the dissolution under the conditions of the oscillation process and low rotation velocities. If the thermally

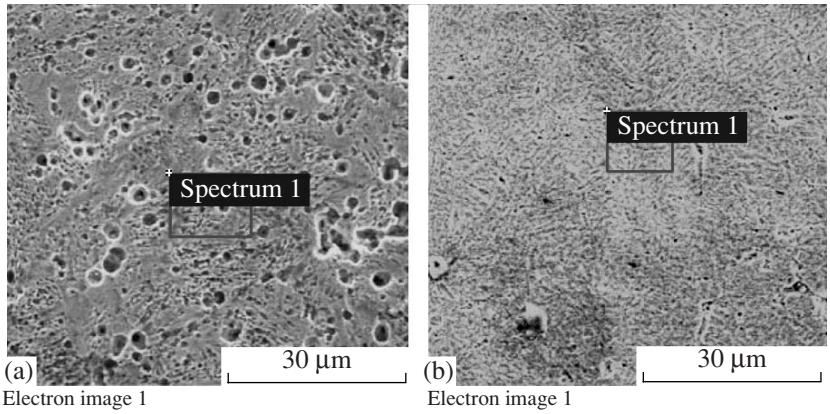

Fig. 14. Micrographs (SEM) of the TT specimen surface after anodic dissolution in 1 M NaCl under the conditions of the oscillation process (2300 rev/min) (a) and low (280 rev/min) velocities of the RDE rotation (b).

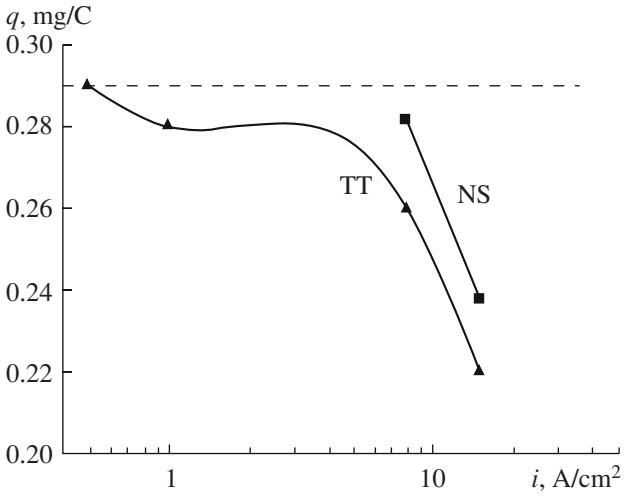

Fig. 15. The influence of the current density on the specific rate of dissolution of the thermally treated and nitrided (T = 750°C) St3 at dissolution in 2 M NaCl at 2300 rev/min. The intermittent line shows the specific dissolution rate under these conditions in the diffusion region.

worked St3 initial surface consisted of the oxide Fe(III) with the impurity of cementite (Fe_3C) then after dissolution under the conditions of the oscillation process (Fig 14a) the elemental analysis showed the presence of only cementite in the surface layer only 76.7 ± 1.0 at % Fe + 23.3 ± 1.0 at % C) being close to the stochiometric one for Fe_3C. Obviously under such conditions there occurs the accumulation of cementite in the surface layer repeatedly removed from the surface by the electrolyte flow.

Contrastingly if the dissolution takes place at low rotation velocities and low diffusion current density (Fig. 6, Fig 14b) in spite of the growth of the concentration of carbon and iron there presents oxide in the surface layer though its concentration being smaller (−12.8 at % of oxygen as compared with ~67 at % in the initial surface after thermal treatment).

Transpassive Dissolution

The specific dissolution rate versus current density relationship both for thermally worked and nitrided steel at the RDE maximum rotation velocity is presented in Fig. 15. It is seen the reduction of the dissolution rate the current density growing being caused by the surface oxidation. The elemental analysis data confirm this result. The points of the elemental composition measurement are shown in Fig. 16. Despite the different morphology of the surfaces, the measurements were carried out for, the surface composition was nearly the same. Its composition along with C and Fe included oxygen with very big concentration (45 ± 3 at %). It is evident that the decrease of the dissolution rates the current density increasing (Fig. 15) is due to the rise of the surface oxidability.

It should be noted that before the current densities ~8 A/cm^2 the difference of the dissolution rates at different hydrodynamic regimes remained the same as in the diffusion region but at higher (15 A/cm^2) it was absent. It is evident that at high current densities in the transpassive region oxidation of the surface layer plays the determinative role in the formation of its composition but dissolution selectivity causing the disintegration of the carbonaceous films is suppressed.

The comparison of specific dissolution rates for thermally untreated St3 and one subjected to ETCT shows that in the region of transpassive dissolution they are close to each other (Fig. 7, Fig. 15) being higher for the nitrided steel, obviously due to the possible chemical reaction of the nitride dissolution.

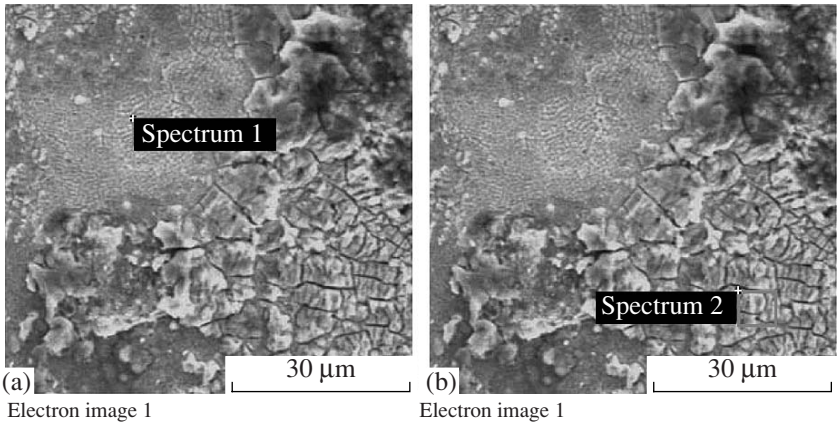

Fig. 16. The surface morphology (SEM) after dissolution of the nitrided steel (T = 650°C) in 2 M NaCl at 5 A/cm^2 with an RDE rotation velocity of 2300 rev/min. Explanations are given in the text.

CONCLUSIONS

The comparative analysis of the processes of anodic dissolution of steels after ETCT in various ranges of potentials (current densities) shows that, in the range of anode–anion activation ("sublimiting" currents), as well as transpassive dissolution, the differences in the rates of dissolution of the untreated steel and the thermally worked (nitrided) one are negligible. The exception is the insignificant rise of the metal removal rate for the nitrided steel as compared with the untreated and thermally worked one caused by the additional chemical reaction of the nitride dissolution initiated by the iron (ferrite) anodic dissolution.

A substantial difference is observed in the region of the diffusion control of the reaction rate. It is elicited by the selective dissolution of various phase components and partial disintegration of the surface layer at intensive hydrodynamic regimes of the treatment. In the studied range of potentials (current densities), the treatment hydrodynamic regime plays a twofold role. On the one hand, it ensures the removal of the soluble treatment products and thus determines the salt passivation currents (anode limiting currents) and, on the other hand (under intensive hydrodynamic conditions), results in the partial disintegration of the carbonaceous surface layers generated due to the selectivity of the dissolution of various phase components (cementite, ferrite) of the surface. Such an effect isn't observed at relatively low rates of hydrodynamic flows, as, in this case, the formed salt film fully covers the electrode surface and dissolution occurs through it.

REFERENCES

1. Dikusar, A.I., Engel'gardt, G.R., Petrenko, V.I. and Petrov, Yu.N., *Elekdrodnye protsessy i protsessy perenosa pri elektrokhimicheskoi razmernoi obrabotke metallov* (Electrode Processes and Processes of Transfer at Electrochemical Machining of Metals), Kishinev: Shtiitsa, 1983.
2. Davydov, A.D. and Kozak, E., *Vysokoskorostnoe elektrokhimicheskoe formoobrazovanie* (High Rate Electrochemical Forming), Moscow: Nauka, 1990.
3. Petrov, Yu.N. and Mochalova, G.L., Influence of Microstructure of Steel 40 and U10 on Surface Finish and Metal Removal Rate at the Electrochemical Machining, *Electron. Obrab. Mater.*, 1968, no. 1, pp. 15–17.
4. Zaidman, G.N. and Petrov, Yu.N., *Formoobrazovanie pri electrokhimicheskoi pazmernoi obrabotke metallov* (Forming at Electrochemical Machining of Metals), Kishinev: Shtiintsa, 1990.
5. Belkin, P.N. *Elektrokhimiko-termicheskaya obrabotka metallov i splavov* (Electrothermochemical Treatment of Metals and Alloys), Moscow: Mir, 2005.
6. Handbook of Electrochemistry, Sukhotin, A.M., Ed., Leningrad: Khimiya, 1981.
7. Dikusar, A.I., Ivanenkov, I.A., Saushkin, B.P., Silkin, S.A. and Yushchenko, S.P., High Rate Anode Dissolution of Heat-Resistant Chrome-Nickel Alloys Containing Tungsten and Rhenium. I Chloride Solutions, *Electron. Obrab. Mater.,* 2007, vol. 43, no. 1, pp. 1–10 [Surf. Eng. Appl. Electrochem. (Engl. Transl.) vol. 43, no. 1, pp. 1–10].
8. Kuo, N.S. and Landolt, D., On the Role Mass of Transport in High Rate Dissolution of Iron in Concentrated Chloride Media, Electrochim. Acta. 1975, vol. 20, no. 5, pp. 393.
9. Davydov, A.D., Kabanov, B.N., Kashcheeev, V.D., Mirzoev, R.A. and Nenashev, V.A., Anode Dissolution of Nickel in Solutions Being Mixed as Applied to the Electrochemical Machining, *Fiz. Khim. Obrab. Mater.*, 1972, no. 4, p. 139.
10. Kirgintsev, A.I., Trushnikova, L.N. and Lavrent'eva, V.G., *Rastvorimost' neorganicheskikh veshchestv v vode*, (Solubility of Inorganic Substances in Water), Reference Book, Leningrad: Khimiya, 1972.
11. Davydov, A.D., Karimov, A.Kh. and Voronenko, L.M., Influence of Structure of Steels on Their Anode Dissolution, *Electron. Obrab. Mater.*, 1974, no. 4, pp. 19–23.
12. Spitsyn, I.A., Davydov, A.D. and Batishchev, A.N., Anode Treatment of Cast Irons in Solutions of Chloride Iron at Electrochemical Running Iron Plating, *Electron. Obrab. Mater.*, 1984, no. 5, pp. 32–36.
13. Dikusar, A.I., Redkozubova, O.O., Yushchenko, S.P. and Yakhova, E.A., The Analysis of the Macroscopic Heterogeneity Effect on the Iron Anode Dissolution Rate in the Region of the Mixed Kinetics, *Elektrokhimiya*, 2002, vol. 38, no. 6, pp. 712–718.

ISSN 1068-3755, Surface Engineering and Applied Electrochemistry, 2008, Vol. 44, No. 5, pp. 353–358. © Allerton Press, Inc., 2008.
Original Russian Text © V.F. Gologan, Zh.I. Bobanova, S.Kh. Ivashku, 2008, published in Elektronnaya Obrabotka Materialov, 2008, No. 5, pp. 15–21.

ELECTRICAL SURFACE TREATMENT METHODS

Influence of an Induction-Capacitance Device on the Structure and Wear Resistance of Electrolytic Chromium Coatings

V. F. Gologan, Zh. I. Bobanova, and S. Kh. Ivashku

Institute of Applied Physics, Academy of Sciences of Moldova, ul. Academiei 5, Chisinau, MD-2028 Republic of Moldova
E-mail: bobanova@phys.asm.md

Received February 26, 2008

Abstract—The experimental data obtained at various parameters of the inductance–capacitance device (ICD) are presented. By varying the values of the inductance and capacity, it is possible to make a significant impact on the morphology, structure, and wear resistance of electrodeposited chromium.

DOI: 10.3103/S1068375508050025

It is shown in many works that the conditions of electrolysis, for the most part, determine the kinetic characteristics of the electrocrystallization and, therefore, the properties of the electrodeposited coatings [1, 2].

Earlier, it was found that a change in the parameters (induction and capacitance) of an inductance-capacitance device (ICD) connected in series to a power supply leads to a wide range of variations (200 mV) of the cathode potential in the process of chromium deposition. At the highest shift in the cathode potential to the positive range, the power yield increased, while the roughness and irregularity of the coating thickness decreased [3].

The aim of the present paper is to study the influence of the ICD parameters on the structure and wear resistance of chromium coatings and to determine the optimum conditions of electrolysis.

RESEARCH TECHNIQUE

The conditions of the coating deposition were selected taking into account the results obtained in [3]. The coatings were deposited on samples in a multipurpose electrolyte for chromium plating of the following composition: 250 g/l of chromic anhydride and 2.5 g/l of sulfuric acid at a solution temperature of $t_{el} = 55°C$ and at a cathode current density of 5.5–12.0 kA/m^2.

A three-phase rectifier (model VSZh-303) was applied as the power supply.

It was connected to the ICD, wherein the inductance L ranged within 0.027–0.456 mH and the capacitance C was 0.024 F. The circuital current was controlled by a ballast resistor (model RB-302U2).

For studying the morphology, structure, and friction surface of the coatings, optic microscopes (NEOPHOT-2, MM-6) and electron-scanning ones (Stereoscan-150, Tesla BS-340) were applied. The microhardness of the deposits was determined using a microhardness meter (model PMT-3) according to GOST 9450-76 at an indentation load of 100 gf.

The surface roughness was determined by means of a Taylor Hobson form Talysurf Intraseries 50 profilometer–profilograph.

The technique of the friction-and-wear tests was selected taking into account the results of previous studies [4]. The tests were carried out using an SMTs-2 friction-and-wear machine at a sliding velocity of $v = 0.785$ m/s and pressure of $P = 0.198$ GPa under conditions of dry friction. The coatings on round samples (the roller diameter was 50 mm) that possessed a thickness of 0.32–0.35 mm and roughness of $R_a = 0.32$–0.16 μm after polishing were subjected to the tests. Cast iron SCh 24-44 with a contact area of 1 cm^2 was applied as the counterbody. The temperature near the friction zone was measured by means of a thermocouple and a chart-recording millivoltmeter (model KSP-4), and the friction torque value was registered by means of a compensating self-recording instrument (model LKS-4-003).

RESULTS AND DISCUSSION

The studies have shown that the ICD parameters exert a significant influence on the morphology of the electrolytic chromium coatings.

On the surface of coatings obtained at standard conditions of electrolysis, without connection of the device, in the optimum mode ($i_k = 5.5$ kA/m^2), crystalline aggregates of various configurations and sizes were formed; they had a disordered arrangement and clearly defined boundaries. These aggregates consist of smaller elements that also differ in size and configuration. In some cases, aggregates of spheroidal form are observed (Fig. 1a).

Connection of the ICD with parameters shifting the cathode potential to a more negative range in comparison with its value at deposition without the ICD leads

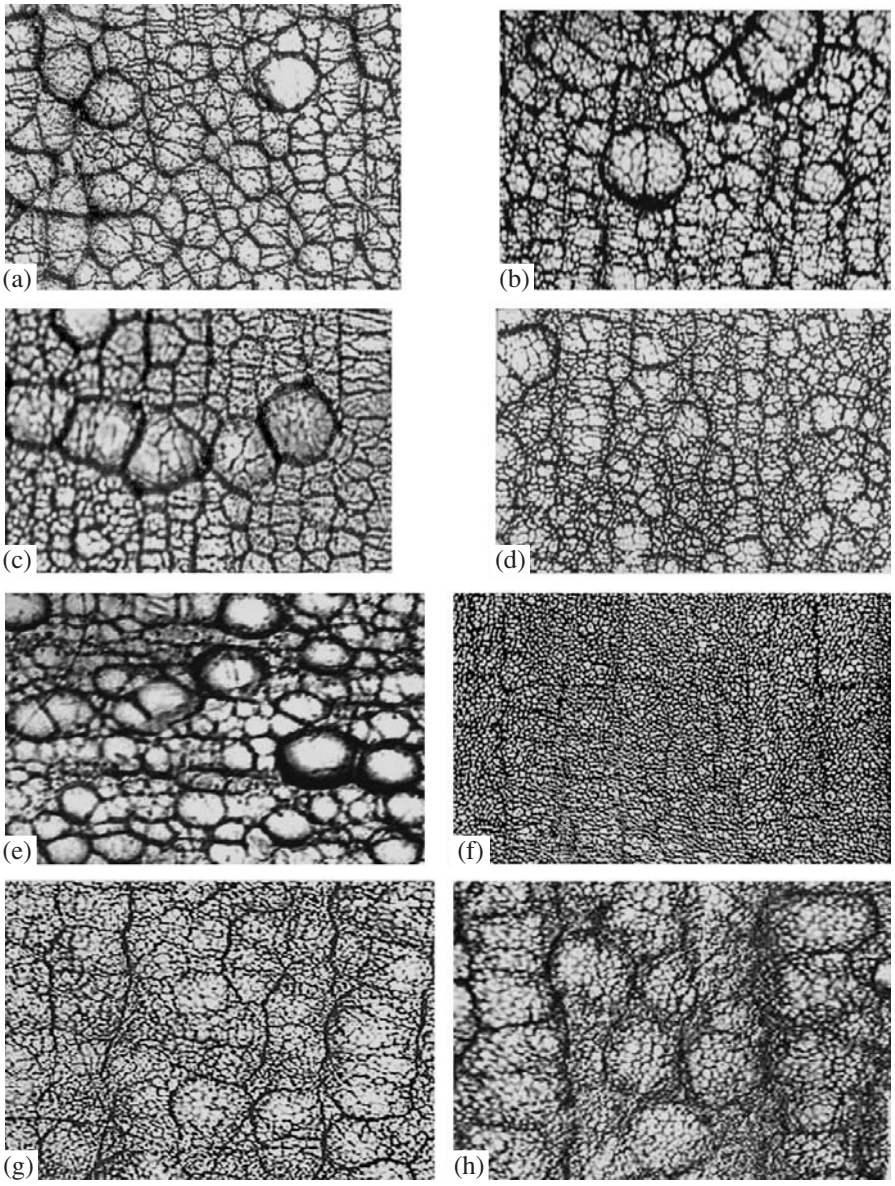

Fig. 1. Influence of the deposition conditions on the morphology of the coatings (×500), C = 0.024 F: (a) i_k = 5.5 kA/m^2, without the device; (b) i_k = 5.5 kA/m^2, with the device (L = 0.456 mH); (c) the same (L = 0.027 mH); (d) the same (L = 0.199 mH); (e) i_k = 8.5 kA/m^2, without the device; (f) i_k = 8.5 kA/m^2, with the device (L = 0.199 mH); (g) the same, i_k = 10.0 kA/m^2; (h) the same, i_k = 12.0 kA/m^2.

to the appearance of separate crystalline formations of larger sizes at simultaneous size reduction of other aggregates (Figs. 1b, 1c).

In the case of deposition at the optimum values of the induction and capacitance of the ICD (L_{opt} = 0.119 mH, C_{opt} = 0.024 F) [3], formation of a more homogeneous and smooth surface takes place due to the absence of large crystalline aggregates. In addition, the number of smaller components, which contribute to the intergrowth of boundaries of larger crystals, increases (Fig. 1d).

At chromium deposition in the customary mode at a current density of 8.5 kA/m^2, aggregates of different sizes are observed on the coating surface with many of them being of the spheroidal type (Fig. 1e). In comparison with the coatings obtained at 5.5 kA/m^2 without connection of the circuit, the considered surface is less homogeneous, the space between larger formations is filled by small aggregates, and this leads to an increase in the number of macrodefects.

Connection of the ICD with the optimum parameters (L_{opt} = 0.119 mH, C_{opt} = 0.024 F) allows obtaining a smooth and homogeneous surface of the coatings at the same current density (Fig. 1f). At close examination, it appears that active centers are formed on the surface; an outgrowth of the coating occurs around the

centers. However, they tower insignificantly and do not lead to the formation of boundaries at their linking.

An increase in the current density (i_k = 10.0–12.0 kA/m^2) at the same parameters of the ICD results in the formation of a cruder surface as compared with the previous one (Figs. 1g, 1h). Active centers are formed on the surface; in contrast to the previous case (Fig. 1f), they grow to large sizes; their linking is achieved by formation of smaller aggregates of different orientations (Fig. 1h); and, alternatively, clearly defined boundaries are formed in places of the linking (Fig. 1g).

Measurements of the roughness of the coating surface have shown that the deposits obtained with the ICD connected are smoother and they keep shining up to a current density of 12.0 kA/m^2 (Table 1). The surface roughness of the coatings obtained in the customary conditions at a current density of 5.5 kA/m^2 was higher than that of the coatings deposited with the ICD at the optimum parameters, that is, at current densities of 5.5–12.0 kA/m^2.

The coatings obtained at i_k = 5.5 kA/m^2 with the circuit parameters L_{opt} = 0.456 mH and C_{opt} = 0.024 F appeared to be rougher (R_a = 0.86 μm, R_z = 3.94 μm). However, the highest roughness was found for the coatings deposited at i_k = 8.5 kA/m^2 without connection of the device (R_a = 2.6 μm, R_z = 8.68 μm).

The lowest roughness was found for the surface of the coating obtained at i_k = 8.5 kA/m^2 with connection of the ICD and the optimum parameters (R_a = 0.12 μm, R_z = 0.8 μm).

Table 1. Influence of the induction-capacitance device parameters on the coating roughness

Deposition conditions	R_a, μm	R_z, μm
i_k = 5.5 kA/m^2	0.76	3.8
i_k = 8.5 kA/m^2	2.6	8.68
With ICD connection		
(L = 0.456 mH, C = 0.024 F)	0.86	3.94
i_k = 5.5 kA/m^2		
With ICD connection		
(L = 0.119 mH, C = 0.024 F):	0.51	2.5
i_k = 5.5 kA/m^2	0.12	1.1
i_k = 8.5 kA/m^2	0.628	3.16
i_k = 10.0 kA/m^2	0.66	3.8
i_k = 12.0 kA/m^2		

The above-described results of the estimation of the chromium coating surface roughness are in good agreement with their morphology (Fig. 1d).

The results of the study of the coating structure on the frontal section also count in favor of the significant influence of the ICD parameters on the process of electrolytic chromium deposition (Fig. 2).

The coatings deposited without the device at 5.5 and 8.5 kA/m^2 consisted of aggregates of different sizes (Figs. 2a, 2b). In many cases, at linking of large blocks

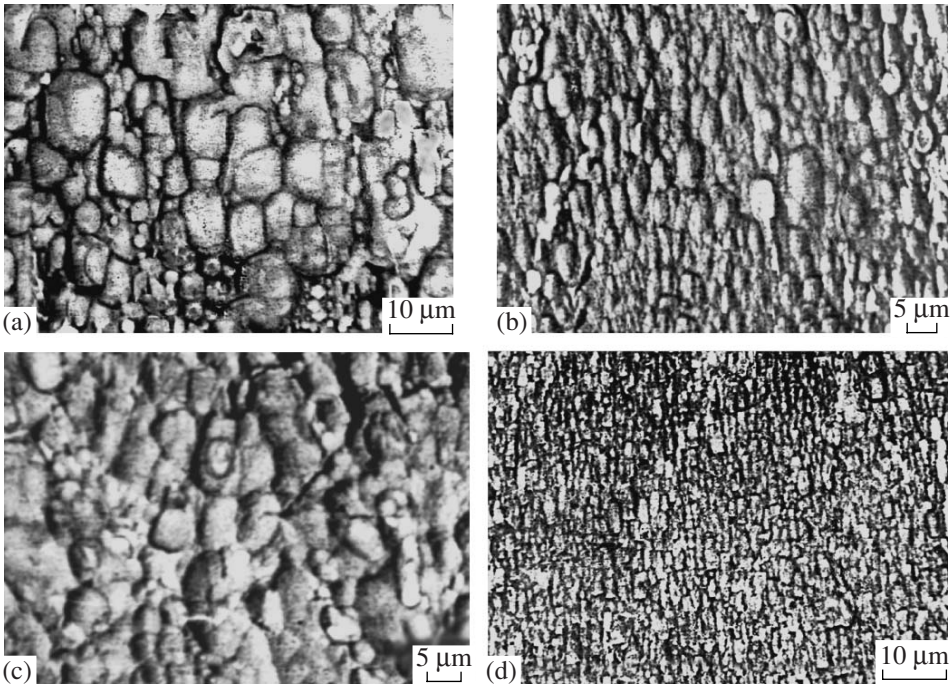

Fig. 2. Influence of the deposition conditions on the structure of the coatings, C = 0.024 F: (a) i_k = 5.5 kA/m^2, without the device; (b) i_k = 5.5 kA/m^2, with the device (L = 0.199 mH); (c) i_k = 8.5 kA/m^2, without the device; (d) i_k = 8.5 kA/m^2, with the device (L = 0.199 mH).

Table 2. Influence of the induction-capacitance device parameters on the coating microhardness

Deposition conditions	H_μ^{100}, GPa
i_k = 5.5 kA/m^2	9.3
With the ICD connection (L = 0.119 mH, C = 0.024 F):	
i_k = 5.5 kA/m^2	10.5
i_k = 8.5 kA/m^2	11.3
i_k = 10.0 kA/m^2	10.7
i_k = 12.0 kA/m^2	9.6

(~5–10 μm), microdefects in the form of microcracks and pores are formed. Their number decreased when smaller aggregates, ensuring the continuity of the coating, formed on the boundaries. Therefore, the roughness of the microsection surface is apparently due to the fact that, in the course of the sample polishing, the aggregates themselves were not ruined; they were divided along their boundaries. As one can see from the presented photographs, an increase in the current density (i_k = 8.5 kA/m^2) did not lead to appreciable changes in the chromium deposit structure.

The coatings obtained with application of the ICD at the optimum values (L_{opt}, C_{opt}) also significantly differ in their structure from the above mentioned ones. The crystalline aggregates have a prolate form (Figs. 2b, 2d), are situated perpendicular to the substrate, and insignificantly differ in their sizes (2–5 μm in the cross section). Due to the decrease in the sizes of the crystalline formations and their form, linking of the aggregates with each other is simplified. As well as in the previous case, the strength of the structural elements themselves is higher than the bond strengths along their boundaries.

The coatings deposited at i_k = 8.5 kA/m^2 (Fig. 2d), in comparison with the deposits obtained at i_k = 5.5 kA/m^2 (Fig. 2b), are finer with identical sizes of the aggregates; this affected the formation of their morphology and the roughness of the surface (Fig. 1f, Table 1). Apparently, this became possible due to the more uniform distribution of the current over the coated surface.

The change in the chromium coating structure at application of the ICD exerted an influence on the microhardness too (Table 2).

For the coatings deposited at i_k = 5.5 kA/m^2, the microhardness increased from 9.3 to 10.5 GPa at application of the circuit. The highest hardness was found for the coatings obtained at i_k = 8.5 kA/m^2 with the ICD (H_μ = 11.3 GPa). At further increase of the current density, H_μ decreased; it was 9.6 GPa at i_k = 12.0 kA/m^2.

The carried out friction-and-wear tests have shown that, at the selected test conditions, the friction couple was generally worn in within ~20 min; at an increase in the test time, the friction torque and the temperature in the friction zone decreased insignificantly (Fig. 3).

Periodic weighing of the rollers has shown that their wear inappreciably varied at the sample rearrangement, and the wear rate was kept practically constant at an increase in the test time.

As a result of the carried out studies, it was found that, after 144 h of the tests, the coatings deposited with application of the ICD were worn down less that the ones obtained without such a circuit at the optimum conditions of the electrolysis (i_k = 5.5 kA/m^2, t_{el} = 55°C) (Table 3). The deposits obtained at current den-

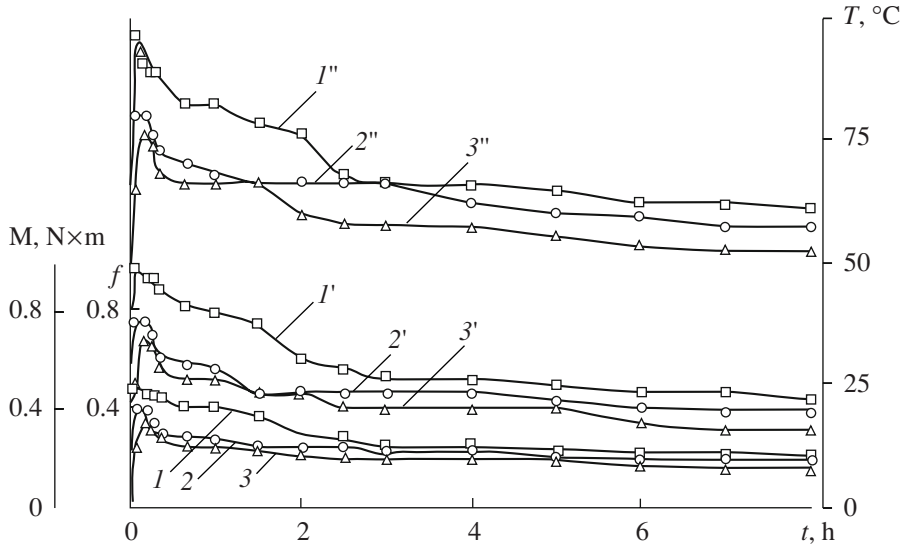

Fig. 3. Influence of the deposition conditions on the friction torque (*1–3*), the friction coefficient (*1'–3'*), and the temperature near the friction zone (*1"–3"*): (*1*) i_k = 5.5 kA/m^2, without the device; (*2*) i_k = 5.5 kA/m^2, with the device (C_{opt}, L_{opt}); (*3*) i_k = 8.5 kA/m^2, with the device (C_{opt}, L_{opt}).

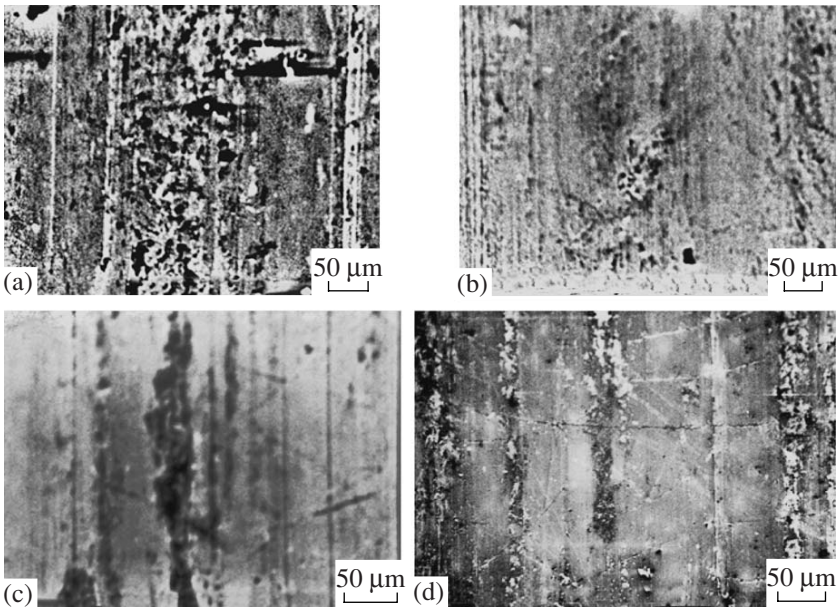

Fig. 4. Influence of the deposition conditions on the wear of the coatings, $C = 0.024$ F: (a) $i_k = 5.5$ kA/m^2, without the device; (b) $i_k = 5.5$ kA/m^2, with the device ($L = 0.199$ mH); (c) the same, $i_k = 8.5$ kA/m^2; (d) the same, $i_k = 10.0$ kA/m^2.

sities of 8.5–10.0 kA/m^2 appeared to be more wear resistant.

The determination of the counterbody wear value has also shown that it was worn down less at friction with more wear resistant coatings.

The friction coefficient f and the temperature near the friction surface varied in a similar way (Table 3).

The study of the friction surface has shown that its destruction is caused by defect accumulation in the near-surface layer; subsequently, it led to formation of wear debris. The surface damage depth is apparently attributed to the sizes of the structure elements of the coating: a cruder friction surface was observed for the coatings obtained at $i_k = 5.5$ kA/m^2 without ICD and at $i_k = 12.0$ kA/m^2 with ICD; less deep destruction is found on worn-out surfaces of the coatings deposited at $i_k = 8.5$–10.0 kA/m^2 with ICD (Fig. 4).

The presented data are also confirmed by the results of the measurement of the roughness of these surfaces (Table 4). The minimum roughness was found for the coatings obtained at 8.5 kA/m^2 with ICD ($R_a = 0.09$ μm, $R_z = 0.6$ μm).

For testing of the coatings in a production environment, chromium coatings were deposited on the wearing surfaces of the shaft of a TV-11-25A gear-type pump, which was installed for the preparation of emulsions of sunflower-oil production residue containing up to 3% cellulose. The pump was in operation until the completion of the performance loop. As a result of the carried out studies, it was found that the coatings obtained at 5.5 kA/m^2 in the customary mode worn down greater by a factor of 1.5 than the coatings deposited at the same current density with the ICD connected and by a factor of 2 in comparison with the coatings obtained at 8.5 kA/m^2 with ICD (Fig. 5).

Thus, the carried out studies have shown that the ICD parameters exert a significant influence on the structure and wear resistance of electrolytic chromium. Despite the fact that, at the optimum parameters of the device, the cathode potential shifted to a more positive range, the coating structure was formed of smaller crystalline aggregates; this is probably related to the character of the current distribution on the surface, which apparently leads to formation of a great number of nucleation centers that do not grow to large sizes. Similar results were obtained at deposition of copper and nickel coatings with application of the ICD [5, 6].

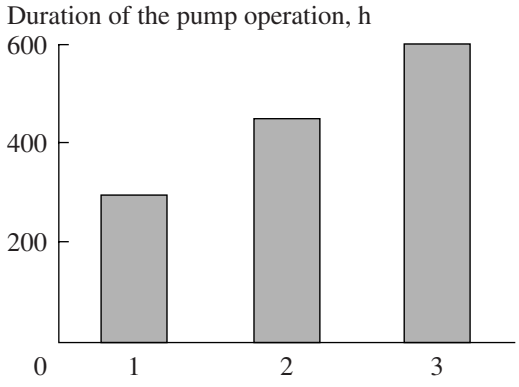

Fig. 5. Results of production tests of the coatings obtained under the electrolysis conditions: (*1*) in the customary mode, $i_k = 5.5$ kA/m^2; (*2*) with the ICD, $i_k = 5.5$ kA/m^2; (*3*) the same, $i_k = 8.5$ kA/m^2.

Table 3. Wear of the coatings

Deposition conditions	Coating wear, mg	Cast iron wear, mg	Friction coefficient f	Temperature in the contact zone T, °C
i_k = 5.5 kA/m^2	63.2	1391.9	0.42	62
With ICD connection (L = 0.119 mH, C = 0.024 F):				
i_k = 5.5 kA/m^2	49.96	1085.3	0.38	58
i_k = 8.5 kA/m^2	27.2	725.6	0.31	52
i_k = 10.0 kA/m^2	33.8	991.7	0.33	55
i_k = 12.0 kA/m^2	46.6	1032.5	0.37	57

Table 4. Influence of the induction-capacitance device parameters on the roughness of the worn-out surfaces of coatings

Deposition conditions	R_a, μm	R_z, μm
i_k = 5.5 kA/m^2	0.69	3.6
With the ICD connection (L = 0.119 mH, C = 0.024 F):		
i_k = 5.5 kA/m^2	0.47	2.2
i_k = 8.5 kA/m^2	0.09	0.6
i_k = 10.0 kA/m^2	0.57	3.2
i_k = 12.0 kA/m^2	0.67	3.8

The formation of a homogeneous structure of the coating obtained with application of the ICD leads to an increase in the wear resistance of electrolytic chromium.

REFERENCES

1. Vagramyan, A.T. and Zhemagortsyants, M., *Elektroosazhdenie metallov i ingibiruyushchaya adsorbtsiya* (Metal Electrodeposition and Inhibiting Adsorption), Moscow: Nauka, 1969.
2. Povetkin, V.V. and Kovenskii, I.M., *Struktura elektroliticheskikh pokrytii* (Structure of Electrolytic Coatings), Moscow: Metallurgiya, 1989.
3. Gologan V.F., Bobanova Zh.I., and Ivashku S.Kh., Features of Chromium Plating Process with Application of an Inductance-Capacitance Device, *Elektron. Obrab. Mater.*, 2008, no. 4, pp. 9–16.
4. Gologan, V.F., Azhder, V.V., and Zhavguryanu, V.N., *Povyshenie dolgovechnosti detalei mashin iznosostoikimi pokrytiyami* (Improvement of Lifetime of Machine Pieces by Wear–Resistant Coatings), Chisinau: Shtiintsa, 1979.
5. Gologan, V.F., Bobanova, Zh.I., Ivashku, S.Kh., Popov, V.A., and Mazur, V.A., Particularities of the Electroplating Process in the Case of Single–Phase Power Supply with an Embedded Induction-Capacitance Device, *Elektron. Obrab. Mater.*, 2007, no. 2, pp. 12–16 [*Surf. Eng. Appl. Electrochem.* (Engl. Transl.), vol. 43, no. 2, pp. 83–86].
5. Gologan, V.F., Bobanova, Zh.I., Ivashku, S.Kh., Mazur, V.A., and Pushkashu, B.M., Features of How the Parameters of an Induction-Capacitance Device Affect the Nickel Plating Process, *Elektron. Obrab. Mater.*, 2007, no. 5, pp. 4–8 [*Surf. Eng. Appl. Electrochem.* (Eng. Transl.), vol. 43, no. 5, pp. 307–311].

ISSN 1068-3755, Surface Engineering and Applied Electrochemistry, 2008, Vol. 44, No. 5, pp. 359–366. © Allerton Press, Inc., 2008.
Original Russian Text © S.I. Galanin, I.V. Kalinnikov, 2008, published in Elektronnaya Obrabotka Materialov, 2008, No. 5, pp. 22–29.

ELECTRICAL SURFACE TREATMENT METHODS

Polarization of Jewelry Gold Alloys by Bipolar Current Pulses in a Polishing Electrolyte

S. I. Galanin and I. V. Kalinnikov

Kostroma State Technology University, ul. Dzerzhinskii 17, Kostroma, Russia
E-mail: ikalinnikov@ya.ru

Received March 4, 2008; in final form, May 20, 2008

Abstract—The polarization is examined of 585th hallmark (14 karat) standard jewelry gold alloys of different colors (red, European yellow, and white) using bipolar current pulses with different amplitude–time parameters aimed at optimizing the electrochemical polishing modes.

DOI: 10.3103/S1068375508050037

INTRODUCTION

Modern jewelry production is characterized by the following:

—permanent complication of the article surface profile,

—a drastic increase in the assortment of manufactured articles combined with a tendency to make unique articles,

—the necessity for a fundamental reduction in the manufacturing duration of the articles, and

—the use of the alloys with different ligatures having different physical-mechanical properties.

To account for these factors, it is necessary to establish new adaptable manufacturing technology cycles of jewelry production, because the traditional technological methods have become inefficient in many respects. This is particularly related to the surface finishing treatment procedures. The electrochemical polishing (ECP) of the article surfaces may be used in both intermediate and final treatment stages [1–6]. Here, the set of experimental investigations and manufacturing testing shows that rectangular bipolar current pulses are preferable [7–10]. Yet, the selection of the optimum pulse amplitude–time parameters (ATP) for the ECP of alloys with different ligatures is connected with certain difficulties because the processes taking place at the treated electrode–electrolyte boundary under bipolar current pulse ECP is still not well understood.

Studies of anode polarization by unipolar and bipolar current pulses with control of the amplitude–time parameter were previously performed without the anode solution limitation [11, 12]. Yet, the ECP conditions differ drastically. During efficient polishing, the following two processes take place simultaneously: the anode solution and the formation of the phases opposing the solution at the anode surface and within the anode electrolyte areas. These complicated anode processes are reflected in the polarization–time and the current–time relations. The polishing efficiency is governed by the relation between the velocities of the processes of the passivating layer formation over the metal surface and its solution in the electrolyte with both process velocities being high enough [13].

In the present work, the polarization is studied of the different colored surfaces (red, European yellow, and white) of 585th hallmark gold jewelry alloys produced using bipolar current pulses in a polishing electrolyte in order to determine the ATP pulse selection criteria to optimize the ECP regimes.

EXPERIMENTAL

$10 \times 8 \times 2$ mm specimens were used for the experiment (the polished area was 80 mm^2); the specimens were molded into the customary models from the alloys whose composition is given in the table.

The specimens were fastened in a special holder with a current carrier and were thoroughly positioned against the cathode made of sheet titanium as well as against the hard gold comparator electrode (probe). The measurement errors were minimized using the technique described in [12, 14]. The specimen surface was thoroughly cleaned, washed with distilled water, and dried.

The specimens were polarized using solitary bipolar pulses and by a continuous bipolar pulse set from the pulse power source (PPS) on the basis of an ID6800 programmed logical controller [15]. The PPS makes it possible to set the time pulse parameters from 100 μs up to 10 ms with a 100 μs increment. The generation regime is also selectable (the solitary pulse, the given number of pulses, the manual stop). Figure 1 shows the PPS output voltage shape. The pulse current amplitude is also selectable from 0 to 10 A.

In the experiment, an electrolyte on the basis of thiocarbamide and sulphuric acid was used: 7% H_2SO_4 +

Compositions of the alloys investigated (State Standard GOST 6835-2002)

Alloy brand	Alloy color	Alloy composition, %						
		Au	Ag	Cu	Pd	Ni	Zn	In
ZlSrM (Au–Ag–Cu) 58.5–5.5	Red	59.50	5.77	33.80	–	–	0.93	–
ZlSrM (Au–Ag–Cu) 58.5–30	Yellow	58.31	31.14	10.56	–	–	–	–
ZlNMTs (Au–Ni–Cu–Zn) 5.5–25–5.5	White	60.20	1.16	26.66	–	5.70	5.81	0.47

9% $SC(NH_2)_2$. The heating system maintained the assigned constant temperature of the electrolyte. The polarization–time and the current–time dependencies were registered by a GRS-6052A digital two-channel oscilloscope having a data digitizing function and an RS-232 port to be connected to a computer.

The service hardware makes it possible to program the oscilloscope, to display the data obtained, and to save the data in **.csv* files containing information on the oscilloscope channel used, the scale (volts and seconds per point), and also a table containing 1000 digitized readings with values from 0 (min) to 255 (max). This format is unhandy for further mathematical processing and graphical data representation. Thus, a program was developed to transform the information from the **.csv* files into a database containing tables of the measured values. Also possible is the formation of cumulative tables and their graphical representation. The resulting polarization–time and current–time dependencies are averaged over 5 experiments performed under the same conditions. Mathematical smoothing of the obtained dependencies was performed.

RESULTS AND DISCUSSION

At the first stage, the electrodes were polarized by a solitary pulse pair: a direct polarity current pulse (DPCP) and a reversed polarity current pulse (RPCP) with varied time parameters at 20, 30, and 40°C. The temperature selection is governed by the advisability of the use of relatively cold electrolytes for ECP of the gold alloy [8, 10]. Figure 2 shows the dependencies obtained for the "red" gold. At the pulse start, the voltage drop within the electrolyte layer between the studied electrode surface and the probe electrode end (marked IR_e in Fig. 2) inserts instantly into the total potential value. At the pulse end, this voltage drop disappears instantly.

Note that increasing the RPCP duration (as well as its amplitude, that is, the quantity of electricity contained in it) causes the current to decrease in the pulse and a respective increase in the cathode polarization and a significant increase in its relaxation duration as compared to its stationary value after the RPCP. Then, the more the quantity of electricity increases, the more significant the cathode polarization peak is at the pulse end and the longer its subsequent relaxation is. Such a trend may be seen, for example, from the beginning of the abundant release of hydrogen, which shields the electrode surface after about a millisecond of the RPCP action. The subsequent t_{del} increase (Fig. 3) does not distort the pulse form and the polarization progress. The same effect is also observed at the increase of the RPCP duration and amplitude, as well as at the t_{del} increase if the RPCP electricity quantity is insufficient.

At the polarization by the continuous pulse set, the pattern becomes more complicated (Fig. 4). The cathode polarization changes: in the frequency regime, its relaxation progresses slower. The RPCP and the cathode polarization process also change. The RPCP drop forms quicker, it becomes more dynamic, and is more apparent; this may be caused by the gas release increase from pulse to pulse. A current peak also appears at the DPCP rise-up front under some amplitude–time parameters caused by the accumulation of the anode reaction products at the electrode surface [12].

The influence of the temperature under the conditions of an insufficient electricity quantity in the DPCP and the RPCP is expected: with its increase, the cathode and the anode polarization decreases (Fig. 5). Yet, with

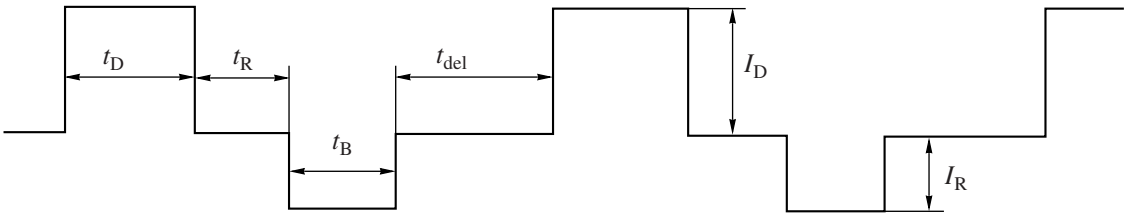

Fig. 1. The output voltage shape of the pulse power source. t_D is the direct polarity current pulse (DPCP) duration, that is, the duration of the first time interval; t_R is the reversed polarity current pulse (RPCP) duration, that is, the duration of the second time interval; t_{del} is the delay between the DPCP end and the RPCP start, that is, the duration of the third time interval; t_B is the break between the RPCP end and the next DPCP start, that is, the duration of the fourth time interval; I_D is the DPCP amplitude; and I_R is the RPCP amplitude.

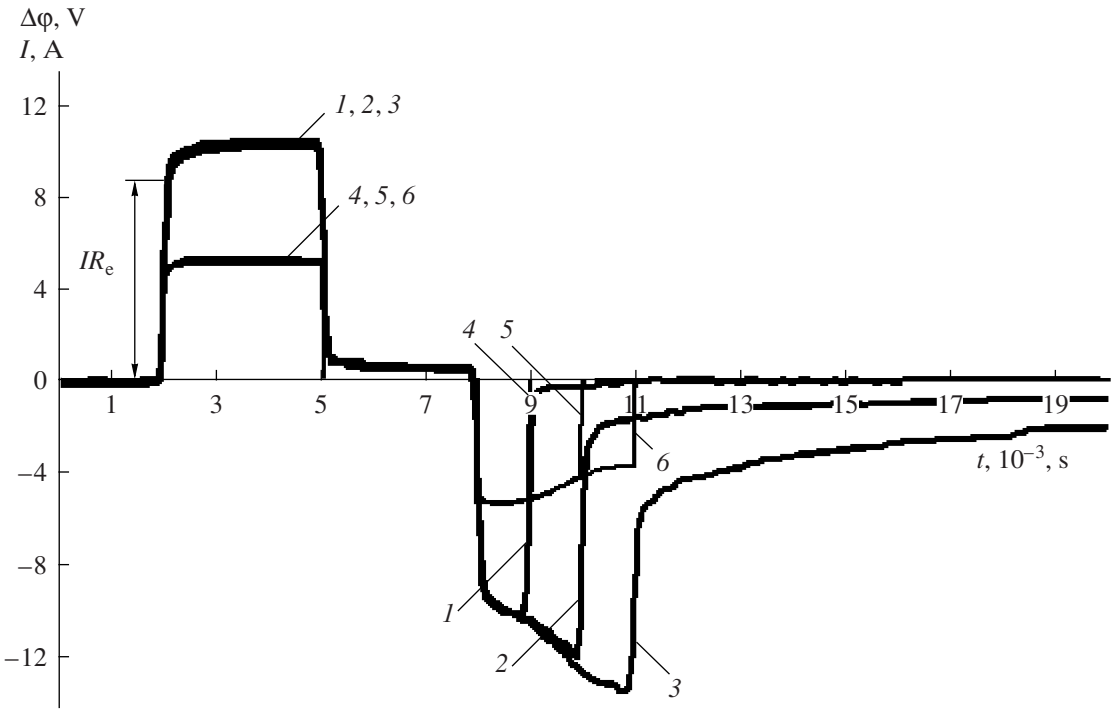

Fig. 2. The polarization–time (*1, 2, 3*) and the current–time (*4, 5, 6*) dependencies for the anode polarization of the "red" gold by the solitary pairs of the bipolar current pulses with the following parameters: $i_D = i_R = 7$ A/cm^2, $t_D = 3$ ms, and $t_{del} = 3$ ms; t_R, ms: (*1, 4*), 1, (*2, 5*), 2, and (*3, 6*), 3; and $T_e = 30$°C. "IR$_e$" is the voltage drop in the electrolyte between the anode surface and the probe electrode.

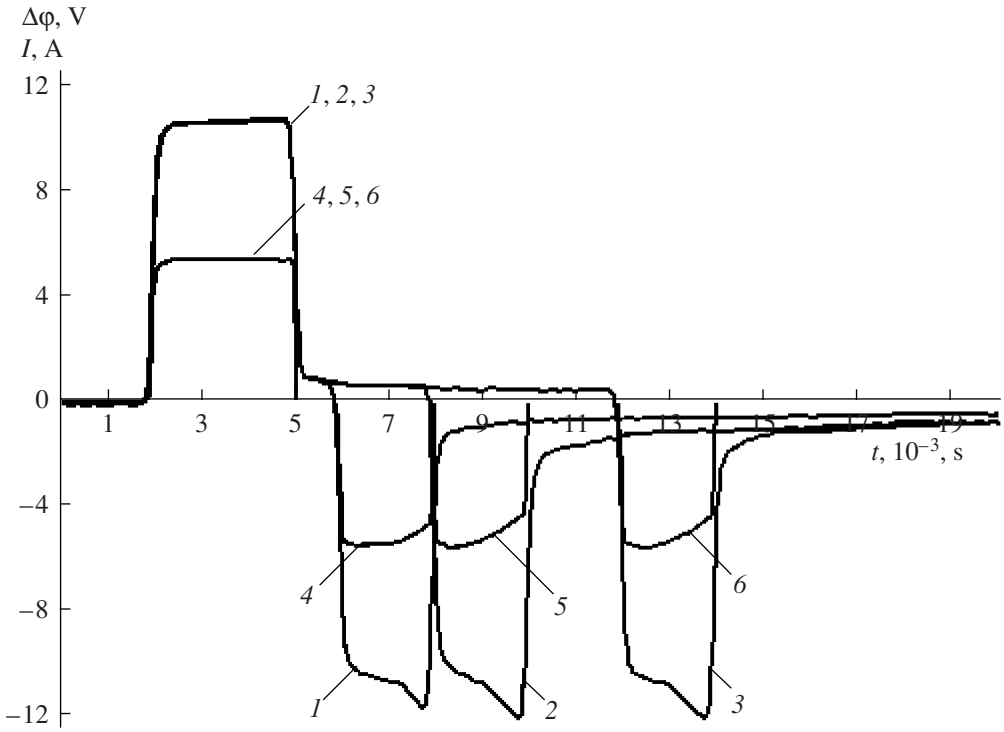

Fig. 3. The polarization–time (*1, 2, 3*) and the current–time (*4, 5, 6*) dependencies for the anode polarization of the "red" gold by the solitary pairs of the bipolar current pulses with the following parameters: $i_D = i_R = 7$ A/cm^2, $t_D = 3$ ms, and t_{del}, ms: (*1, 4*), 1, (*2, 5*), 3, and (*3, 6*), 7; $t_R = 2$; and $T_e = 30$°C.

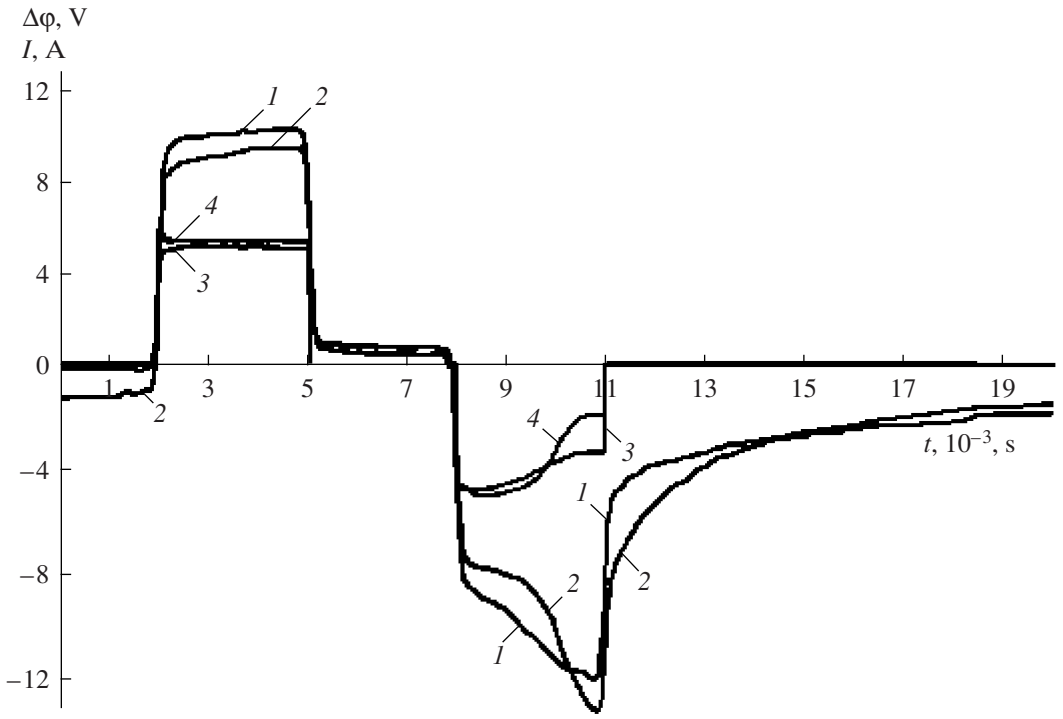

Fig. 4. The polarization–time (*1, 2*) and the current–time (*3, 4*) dependencies for the anode polarization of the "red" gold by the solitary pairs of the bipolar current pulses (*1, 3*) and by the continuous pulse set (*2, 4*) with the following parameters: $i_D = i_R =$ 7 A/cm^2, $t_D = 3$ ms, $t_{del} = 3$ ms, $t_R = 3$ ms, $t_B = 10$ ms, and $T_e = 30$°C.

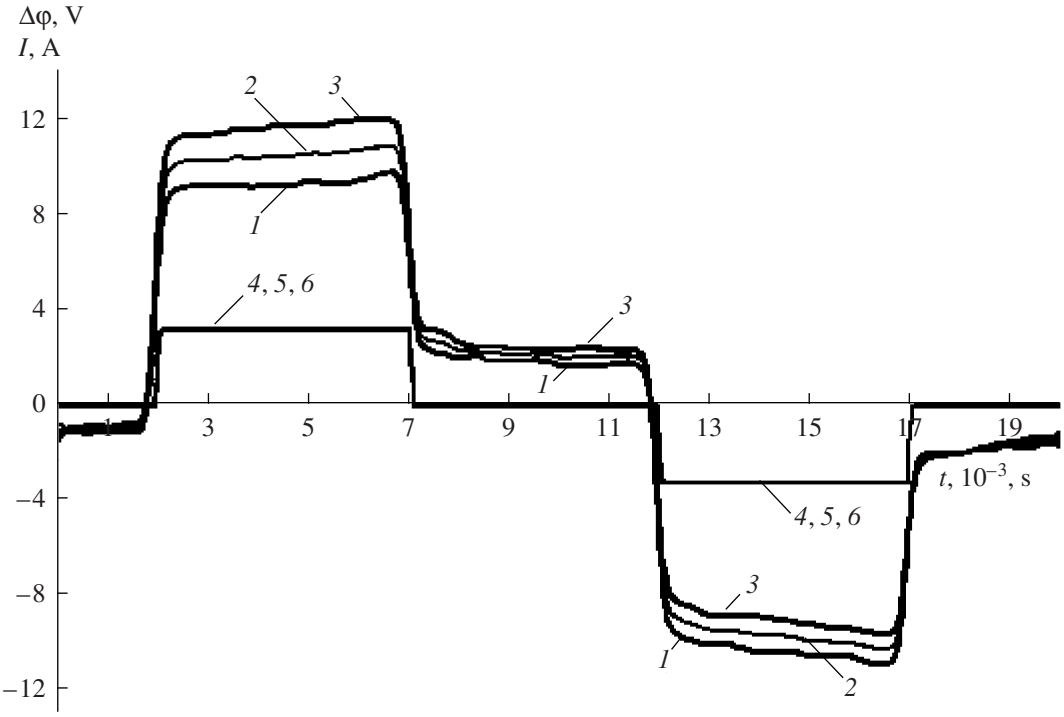

Fig. 5. The polarization–time and the current–time dependencies for the anode polarization of the "red" gold by the continuous pulse set with the following parameters: $i_D = i_R = 1$ A/cm^2, $t_D = 5$ ms, $t_{del} = 5$ ms, $t_R = 5$ ms, and $t_B = 10$ ms; T_e, °C: (*1*), 20, (*2*), 30, and (*3*), 40.

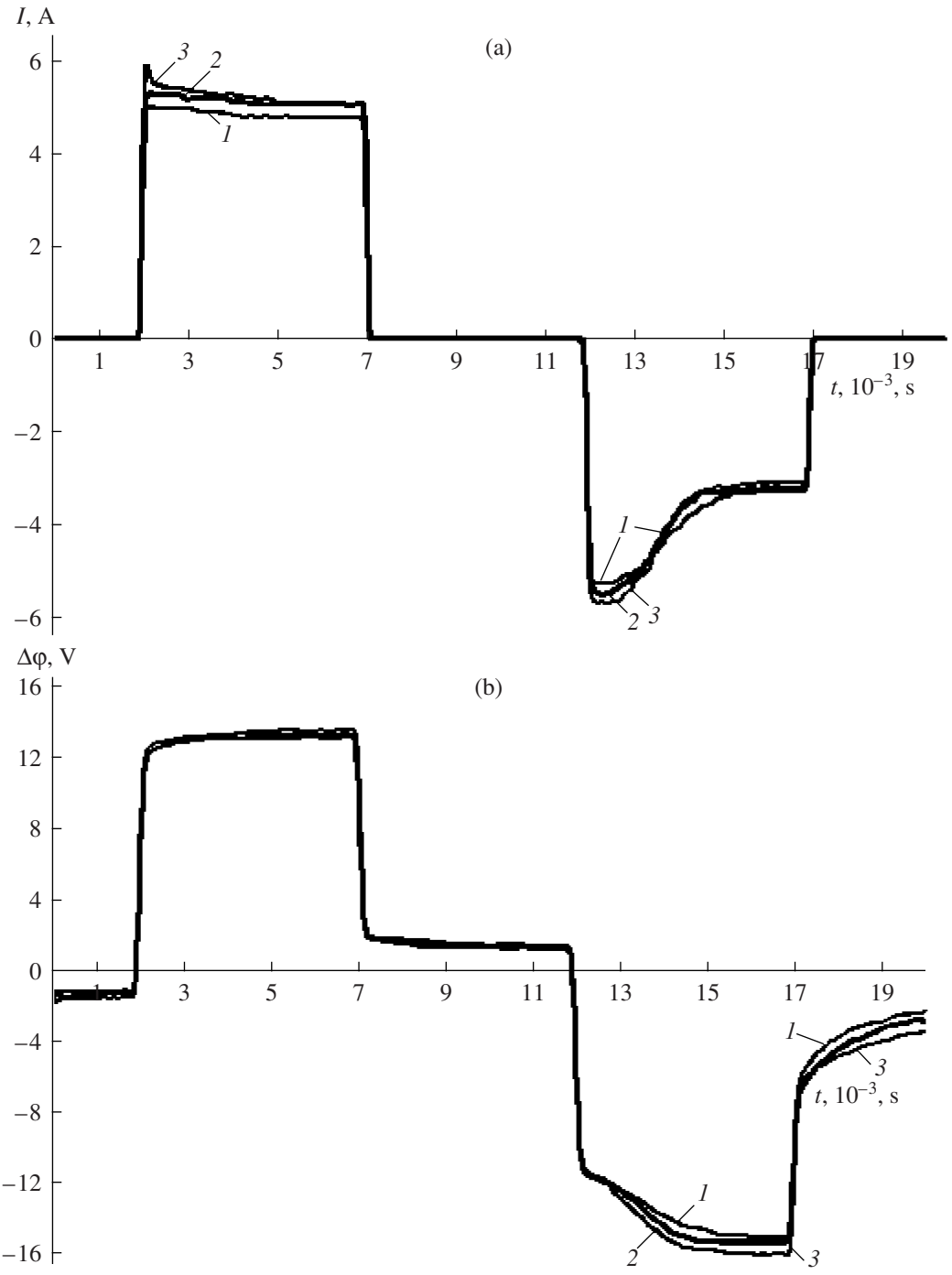

Fig. 6. The current–time (a) and the polarization–time (b) dependencies for the anode polarization of the "red" gold by the continuous pulse set with the following parameters: $i_D = i_R = 7$ A/cm^2, $t_D = 5$ ms, $t_{del} = 5$ ms, $t_R = 5$ ms, and $t_B = 10$ ms; T_e, °C: (*1*), 20, (*2*), 30, and (*3*), 40.

the pulse charge increase, the pattern distinctly changes (Fig. 6). With the temperature increase, a peak occurs at the rise-up DPCP front, the current drop processes grow in the DPCP, and the cathode polarization relaxation value and duration drastically increase. All this is evidence of the cathode and anode reaction products' accumulation from pulse to pulse with the electrolyte temperature increase.

The influence of the alloy composition on the polarization curve behavior is significant. For the polarization by the solitary DPCP and RPCP pair, a relative polarization increase is obtained within the "yellow–

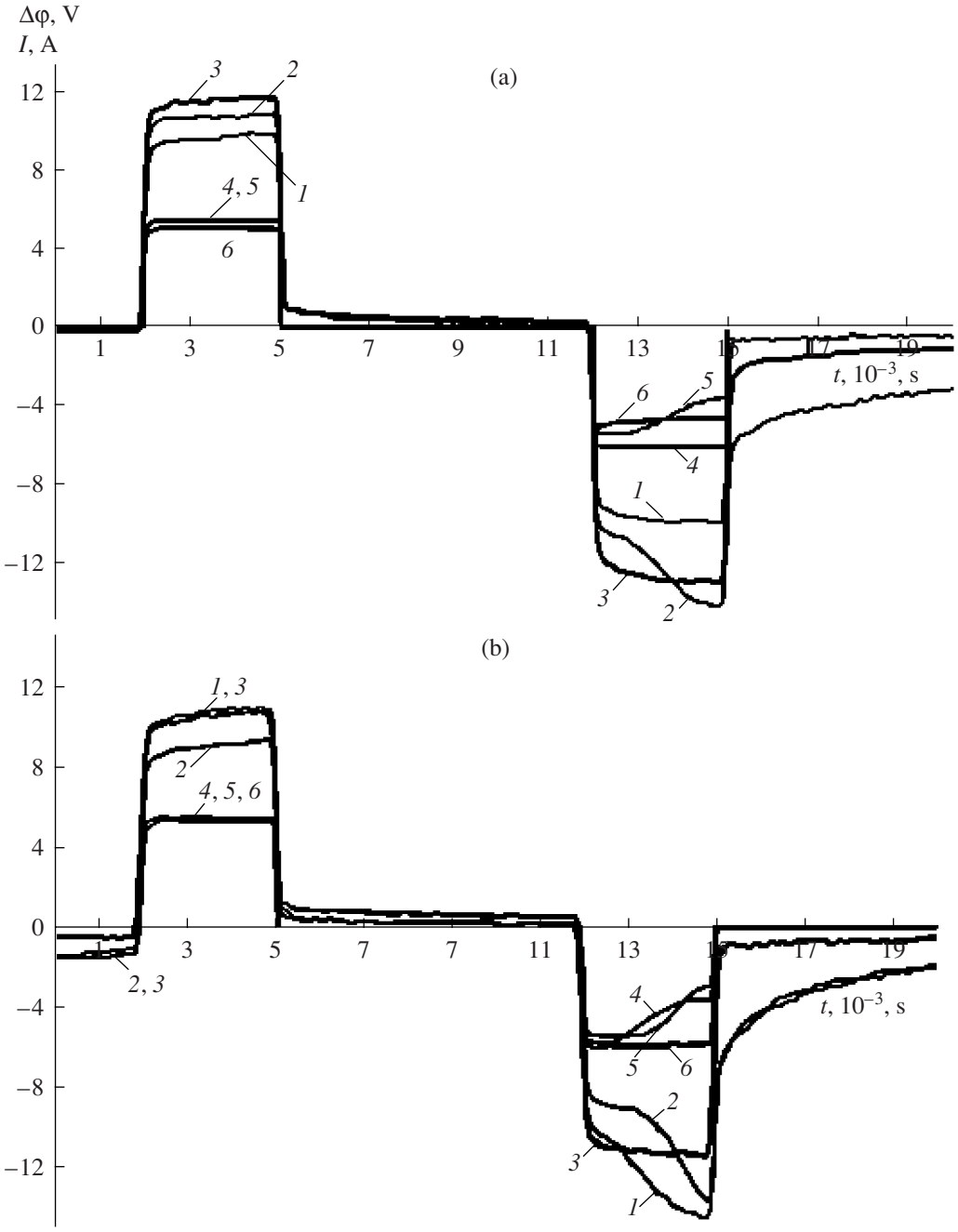

Fig. 7. The polarization–time (*1, 2, 3*) and the current–time (*4, 5, 6*) dependencies for the anode polarization of different gold alloys by the solitary pairs of the bipolar current pulses (a) and by the continuous pulse set (b) with the following parameters: $i_D = i_R = 7$ A/cm^2, $t_D = 3$ ms, $t_{del} = 7$ ms, $t_R = 3$ ms, $t_B = 10$ ms, and $T_e = 30$°C. (*1*, *4*), "yellow" gold; (*2*, *5*), "red" gold; (*3*, *6*), "white" gold.

red–white" gold succession (Fig. 7a). The insignificant DPCP current decrease after about 0.5 ms and the respective anode potential increase are evidence of the growth of the passivating effect. Similarly, under the RPCP electricity quantity excess over a certain value, sharp cathode potential steps take place that may be connected with the side reaction hydrogen release. It also increases the cathode potential relaxation duration. Note that the process dynamics vary with the alloys. For example, for the "yellow" gold, in the RPCP, the side reaction influence on the potential is insufficient; consequently, the cathode potential is also low and relaxes quickly. Just the opposite, for the "white" gold, the side processes begin early and the current pulse shape and potential variations are also significant (Fig. 7a).

Under the polarization by the continuous pulse set, the pattern changes (Fig. 7b). For the "white" gold, with the pulse polarity change, the cathode potential

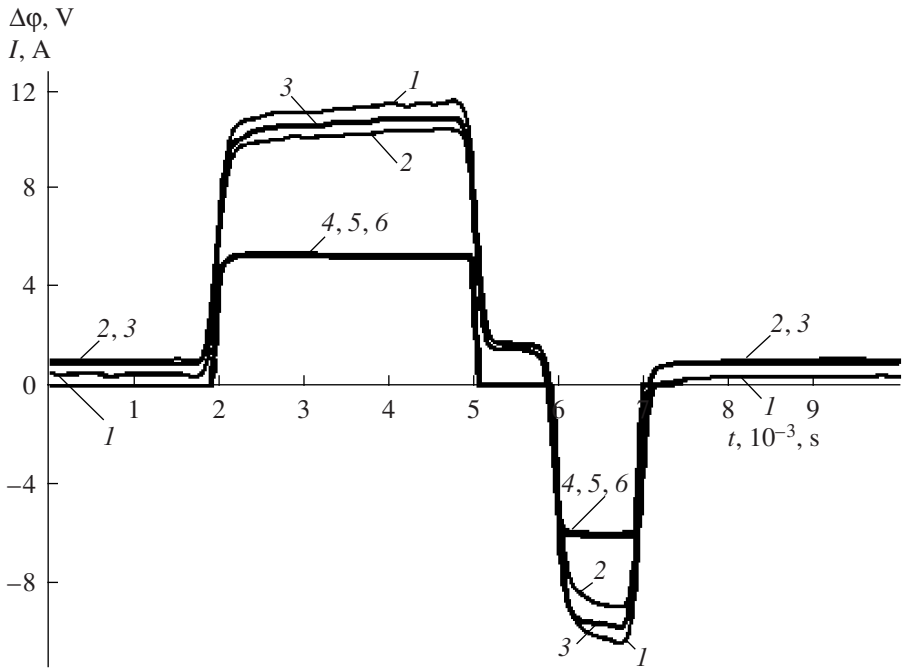

Fig. 8. The polarization–time (*1, 2, 3*) and the current–time (*4, 5, 6*) dependencies for the anode polarization of different gold alloys by the continuous pulse set with the following parameters: $i_D = i_R = 7$ A/cm^2, $t_D = 3$ ms, $t_{del} = 1$ ms, $t_R = 1$ ms, $t_B = 10$ ms, and $T_e = 30$°C. (*1*, *4*), "yellow" gold; (*2*, *5*), "red" gold; (*3*, *6*), "white" gold.

growth connected with the side processes becomes quickly obliterated. For the "yellow" gold, vise versa, the influence of the side processes accumulates successively from pulse to pulse. These two alloys seem to switch places. Under the RPCP duration shortening, for the "yellow" gold, the anode potential may be compensated for quicker (Fig. 8): under similar pulse parameters, even the "overcompensation" is obtained; for the "white" gold, the overcompensation is insignificant; and, for the "red" gold, total potential compensation is obtained. The pattern change under the polarization transition from a solitary pulse pair to a continuous pulse set may be caused by the high dynamism of the processes at the "yellow" gold surface.

The polarization studies show that the use of the RPCP makes it possible to flexibly govern the processes over the anode–electrolyte surface and, under the optimum selection of the amplitude–time parameters, to stabilize the balance between the passivating layer formation on the metal surface and its solution in the electrolyte during the processing.

CONCLUSIONS

1. The results obtained confirm the following well-known fact: the greater the electricity quantity in the pulse, the more probable the occurrence of the parallel process over the electrode surface; the processes increase for polarizing by a continuous pulse set.

2. The polarizations by solitary pulses and by a continuous set differ significantly from each other, thus evidencing the different dynamics of various processes at the anode–electrode boundary.

3. For the polarization by the continuous set of bipolar pulses, during the passivating processes taking place at the anode–electrode boundary, an increase in the RPCP duration and amplitude and an increase in the electrolyte temperature cause growth of the processes over the treated surface that significantly increase its relaxation to the stationary state. In those cases, the metal–electrolyte system becomes poorly dynamic and poorly governed. Governing the system in those cases is only possible by using RPCPs with determined amplitude–time parameters when the polarization–time dependency needed is formed over the metal–electrolyte boundary. The controllability is maximal when the boundary is in the in-between state, that is, when the rates of the passive film growth and its solution become equal and the passivating processes do not go too far. Thus, the electricity quantity in the RPCP should be significantly less than the same in the DPCP.

4. The electrochemical polarization dynamics essentially depend on the processed alloy composition. Hence, for each alloy, unique amplitude–time parameters exist that are optimum for its processing.

REFERENCES

1. Corti, C.W. Back to Basics: Electroplating and Electropolishing of Jewellery, *Gold Technol.*, 2002, no. 3, pp. 19–26.

2. Fink, G. and Moster, B. Electropolishing Gold Jeweler. *Aurum*, 1981, no. 6, pp. 34–41.
3. Gal-Or, L. Electropolishing of Gold Alloys. *Proceedings of the Santa Fe Symposium*, 1988. p. 173.
4. Galanin, S.I. and Uspenskii, S.V. Electrochemical Polishing of the Surface of the ZlSrM 585-80 Alloy by the Bipolar Current Pulses. *Metalloobrabotka*, 2005, no. 2 (26), pp. 10–13.
5. Galanin, S.I., Sorokina, M.V., and Tokmakov, A.Yu. Electrochemical Polishing of the Jewelry Surface Using Pulsed Currents. In: *Materialy IV mezhdunarodnogo simpoziuma yuvelirov "Traditsii, innovatsii i perspectivi sovremennogo yuvelirnogo iskusstva"* (Proc. IV Int. Symp. "Traditions, Innovations, and Prospects of Modern Jewelry Art), St.-Petersburg, July 2005, pp. 186–198.
6. Galanin, S.I., RF Patent 2184801, 2002.
7. Galanin, S.I., RF Patent 2288978, 2006.
8. Galanin, S.I., Subbotin, D.N., Sorokina, M.V., and Tokmakov, A.Yu. Efficiency of Different Surface Polishing Processes of the Jewelry Made of the 585th Hallmark Gold Alloy. *Metalloobrabotka*, 2006, no. 4, pp. 20–25.
9. Galanin, S.I., Sorokina, M.V., Tokmakov, A.Yu. and Galanina, A.S. Polishing and Glossing of the Complicated Profile Gold Jewelry by Current Pulses. *Yuvelirnoe Obozrenie* (Jewelry Review), March 2007, p. 77.
10. Galanin, S.I., Sorokina, M.V. and Galanina, A.S. Eletrochemical Polishing of the Jewelry Gold Alloys by the Bipolar Current Pulses. *Fiz. Khim. Obrab. Mater.*, 2007, no. 5, pp. 67–71.
11. Kalinnikov, V.A. Electrochemical Processing of the Nickel–Chromium Alloys by the Microsecond Rectangular Current Pulses. *Cand. Sci. (Tech.) Dissertation*, Kostroma, 2000.
12. Galanin, S.I. Theory and Practice of Anode Electrochemical Processing by Short Current Pulses. *Doct. Sci. (Tech.) Dissertation*, Kostroma, 2001.
13. Grylikhes, S.Ya. *Elektrokhimicheskoe i khimicheskoe polirovanie: teoriya i praktika. Vliyanie na svoistva metallov* (Electrochemical and Chemical Polishing: Theory and Practice. Influence on the Metal Properties), Leningrad: Mashinostroenie, 1987.
14. Rybalko, A.V. and Galanin, S.I. On the Accuracy Increase of Measurements of Electrical Characteristic of the Inter-Phase Metal–Electrolyte Boundary by Pulsed technique. *Elektron. Obrab. Mater.,* 1985, no. 3, pp. 85–88.
15. Galanin, S.I. and Sorokina, M.V. Electrochemical Polishing and Grinding of the ZlSrM 585-80 Alloy Surface by Current Pulses. *Sbornik trudov 9 VNTK "Sovremennaya elektrotehnologiya v promyshlennosti Rossii* (Proc. 9th VNTK "Modern Electrotechnology in the Industry of Russia"), Tula, Tula State Univ., June 2006, pp. 27–34.

ISSN 1068-3755, Surface Engineering and Applied Electrochemistry, 2008, Vol. 44, No. 5, pp. 367–369. © Allerton Press, Inc., 2008.
Original Russian Text © E.K. Sevidova, L.I. Pupan', V.N. Tsyuryupa, 2008, published in Elektronnaya Obrabotka Materialov, 2008, No. 5, pp. 30–33.

ELECTRICAL SURFACE TREATMENT METHODS

Influence of Coatings on the Surface Strength of Rapid Prototyping Products

E. K. Sevidova[a], L. I. Pupan'[a], and V. N. Tsyuryupa[b]

[a] *National Technical Institute Kharkov Polytechnical Institute, ul. Frunze 21, Kharkov, 61002 Ukraine*
E-mail: grinko@kpi.kharkov.ua

[b] *State Enterprise Malyshev Plant, ul. Plekhanovskaya 126, Kharkov, 61001 Ukraine*

Received February 14, 2008

Abstract—Using the example of a composite material applied in rapid prototyping (RP) technologies, the strengthening effect of various coatings is studied. It is shown that improvement of wear resistance by means of coatings is achieved not only due to formation of a harder layer but also due to the appearance of a homogeneous substance leading to variation in the character of the surface destruction.

DOI: 10.3103/S1068375508050049

INTRODUCTION

Products formed by the method of layer-by-layer synthesis, or rapid prototyping (RP), are most often applied in three aspects: as model-prototypes, models for production of metal casts, or as technological pieces for functional purposes [1]. In the latter case, the properties of the construction material of which the RP products are produced (the physicomechanical, chemical, and corrosion ones) are of significant importance; on the whole, they determine the functional-operational characteristics of the finished products. The selection of the material is governed not only by the purpose of the pieces but also by the type of RP technology applied in the process of the production. Each of them has its restrictions both in the chemical composition and in the physical state of the initial material.

In particular, for formation of RP products by selective laser sintering (SLS), powder materials are used, including metals ones; this implies formation of an initially porous structure. Further impregnation, for example, of the steel porous base with bronze levels the porosity but leads to physicochemical inhomogeneity; this, in turn, worsens the corrosion properties and negatively affects the wear resistance.

It is possible to improve the functional-operational characteristics of RP products obtained by the SLS method from metal powders by deposition of special coatings with improved properties (in comparison with the substrate) on their surface. The aim of the present paper is to study the influence of various coatings on the hardness and wear resistance of the surface layers of metal RP products.

RESEARCH TECHNIQUE

The initial material was samples of a composite formed by the method of indirect SLS technology from a powder of stainless steel (containing 85.3% Fe, 14.3% Cr, 0.3% Mn, and 0.1% Ni) and tin bronze (~86.6% Cu, 10.7% Sn, ~0.6% Pb, and 0.5% Zn). There were studied coatings deposited by different methods, including the chemical (NiP), electrodeposition (Cr_{mw}, Cr_{sol}, and Cu–Ni–Cr_{lus}), and ion–plasma (TiN) methods. The thickness of the chemical and electrodeposited coatings was ~20 μm and that of the ion–plasma ones was ~3 μm.

The hardness and wear resistance were taken as the basic criteria of the surface strength. The hardness of the coatings was measured using a PMT-3 microhardness meter at a load of 100 g.

The wear resistance of the coatings was estimated by virtue of a previously developed installation [2]. The blind end of a rotating cylinder with a stuck-on abrasive cloth with SiC with a grain size of 80 μm was applied as the abrading counterbody. The material wear was carried out under a specific load of 2 kg/cm^2. The time of the tests was 10 min. The abrasive wear was determined by the weight method according to the sample weight loss Δm in a unit of time. The reciprocal of the ratio of the studied material wear in the time $\Delta t/\Delta m$ was taken as the estimation criterion of the wear resistance.

RESULTS AND DISCUSSION

The analysis of the surface hardness of the samples by the method of microhardness measurement was selected taking into account the specific character of the research subject—the micrometer coatings.

Results of target measurement of the microhardness H_μ, kg/mm^2

No. of measurement \ Sample	Initial, after SLS		Ni coating, chem.	Ni coating, heat-treated	Cr coating, milk white	Cr coating, solid	Cu–Ni–Cr + TiN coating	Ni + TiN coating
	1	2	3	4	5	6	7	8
1	472	488	554	620	254	612	509	1288
2	572	488	480	612	284	612	1144	824
3	680	488	548	672	322	932	1144	792
4	446	472	492	762	348	824	841	1018
5	502	366	536	988	386	680	713	1018
6	376	420	478	740	322	572	946	824
7	762	488	598	658	306	894	1144	1168
8	350	536	480	960	322	858	1006	1018
9	446	464	530	836	348	572	1006	762
$\bar{H}_\mu$	501	467	522	761	322	709	939	968
δ_{max}, %	52	15	15	30	27	31	22	21
δ_{min}, %	30	22	8	20	23	19	24	21

With a view of the comparability of the obtained data, the same technique was applied for the estimation of the hardness of the initial metal composite materials, although, in the latter case, accurate measurements are rather problematic due to the structural inhomogeneity.

At the load P = 100 g, the visible indentation of the pyramid d ~ 20–30 μm is less than the diameter of the sintered grains of the stainless steel, the intergrain gaps of the bronze, or the spots of defects (porosity). Therefore, as a rule, when characterizing the hardness of such materials, their Brinell number is given. The average values are higher at larger diameters of the ball-indenter and at higher testing loads.

Taking into account the predicted composite inhomogeneity in the physicomechanical properties, including Hμ, for measurement of the latter an algorithm was developed. In particular, target measurements on the surface were carried out at nine points in two mutually perpendicular directions with increments of 0.5 mm.

The integral value H_μ was determined as the arithmetic mean value $\bar{H}_\mu$; in addition, the deviation of the maximum and minimum values of Hμ from the mean one was calculated

$$\delta_{max} = \left(\frac{H_{\mu^{max}} - \bar{H}_\mu}{\bar{H}_\mu} \right) \times 100\%;$$

$$\delta_{min} = \left(\frac{H_{\mu^{min}} - \bar{H}_\mu}{\bar{H}_\mu} \right) \times 100\%.$$

The results of the Hμ measurements presented in the table allow stating some generalizations.

It is obvious that the initial composite is characterized by a high degree of inhomogeneity; it may be different in different batches (samples nos. 1 and 2). The deposition of all the types of the studied coatings did not lead to equalizing (leveling) of the H_μ values, which could be a priori expected. This is explained, first of all, by the base material influence on the result of the measurement by the accepted technique. At a load of 100 g, a sharply defined reproducible indentation was obtained, but it was a fortiori deep (h = 3–4 μm) for the thicknesses of the studied coatings in order to eliminate the hereditation of the substrate. At the same time, in all the cases, an obvious tendency for equalizing (a decrease in δ_{max} and δ_{min}) of the H_μ values is observed, being the higher the greater the coating thickness or the higher the hardness of the coating substance itself.

In particular, the coating of the chemically deposited nickel with a thickness of 20 μm (sample no. 3) insignificantly increased H_μ as compared to the initial state of the composite (sample no. 1); however, the value of the deviations decreased by a factor of 3.5. It is obvious that the nickel layer (a propos, it can also be considered an Ni–P composite material) is strengthened with respect to tin bronze (the impregnation material) and milder as compared to Fe–Cr–Ni–Mn particles.

An identical increase in hardness ensures a coating of chemical nickel of the same thickness, which is subjected to heat treatment at T = 400°C for two hours. This treatment leads to variation in the layer structure and transition from the amorphous state into the crystalline one. According to [4], the hardness may increase from 500–700 to 850–950 kg/mm^2. The obtained results confirm the strengthening role of the heat-treated coatings with respect to all the components of the initial composite.

Electrodeposited chromium coatings deposited in different technological modes render different influences on the surface strength. As expected, milk white chromium (sample no. 5) decreases the averaged value $\overline{H}_\mu$ by a factor of 1.5; lusterless chromium (sample no. 6) increases it by a factor of 1.4. The result is logical, since the initial hardness of milk white chromium does not exceed 400–500 kg/mm^2, and, for lusterless (solid) chromium, it can achieve values on the order of 750–1100 kg/mm^2.

The most significant increase in the surface hardness of RP products is ensured by a TiN coating deposited on the surface after it is preliminarily chromium plated or chemically nickel plated (sample nos. 7 and 8). At identical thickness of the external layer (3 μm) and identical conditions of its deposition, somewhat better indices of $\overline{H}_\mu$ are obtained for SLS samples with an underlayer of chemical nickel. This underlayer, in the process of ion-plasma deposition of TiN, was subjected to bombarding by high-energy ions of titanium; as a result, it is heated up to a temperature of 400–420°C (and above in the ion-clearing process) and crystallizes. Herein, as was mentioned above, its microhardness significantly increases, in contrast to electrodeposited chromium, which is not affected by concurrent heat treatment.

The results of the wear tests (see the figure) correlate, to a certain extent, with the estimation indices of the surface microhardness. As expected, the highest and practically identical indices are characteristic of systems of coatings with the TiN external layer on the intermediate base of chemical Ni and three-layer electrodeposited Cu–Ni–Cr coating. Their wear resistance exceeds the initial composite index by more than a factor of 100. Almost identical wear resistance is found for coatings of heat-treated chemical Ni and solid Cr with some advantage found for the latter.

The wear resistance of relatively mild milk white chromium (H_μ ~ 330 kg/mm^2) is the lowest among the studied coatings. At the same time, despite a decrease in hardness with respect to the initial material by a factor of 1.4–1.5, it is worn down less intensively (by a factor of 5–7). This discrepancy can be explained by the different character of the wear of the two materials. At abrasive action on the surface, the initial substance, being a composite of solid particles in relatively mild bronze, fails, most probably, with the solid phase breaking off; this greatly increases its weight wear index. The homogeneous structure of the chromium coating fails more uniformly.

The initial (without heat treatment) coatings of chemical nickel exceed the deposits of milk white chromium in wear resistance, but they are inferior to the heat-treated ones, correlating with the corresponding values of H_μ and with known data [4].

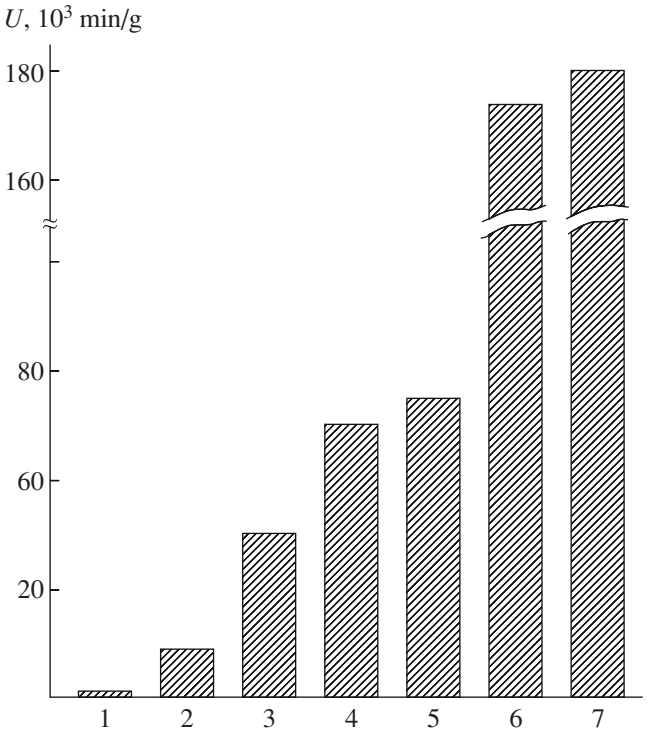

Wear resistance of coatings on SLS material: (*1*) without coating; (*2*) Cr_{mw}; (*3*) Ni_{chem}; (*4*) Ni_{chem}, heat-treated; (*5*) Cr_{sol}; (*6*) (Cu–Ni–Cr) + TiN; (*7*) Ni_{chem} + TiN.

CONCLUSIONS

In the general case, it may be stated that the effect of strengthening coatings on RP products obtained by the SLS method from powder materials is shown to a greater extent in wear tests. Improvement of this index is obtained not so much due to an increase in the surface layer hardness as, first of all, due to formation of a monolithic homogeneous substance, thus leading to variation of the character of the destruction.

REFERENCES

1. Shiganov, I.N., Modern Methods of Rapid Prototyping with Application of Laser Radiation, *Tekhnol. Mashinostroeniya*, 2005, no. 10, pp. 65–71.
2. Sevidova, E.K., Serova, N.N., Pupan', L.I., and Dyubner, L., Estimation of Physicomechanical Properties of Diamond-Like Coatings on Bioengineered Materials, in *Vysoki tekhnologii v mashinobuduvanni. Zb. nauk. pr.* (High Technologies in Mechanical Engineering. Coll. Sci. Papers), Khrakov: NTU "KhPI", 2001, issue 1(4).
3. *Galvanicheskie pokrytiya v mashinostroenii. Spravochnik v dvukh tomakh* (Electrodeposited Coatings in Mechanical Engineering. Handbook in Two Volumes), Shluger, M.A., Ed., Moscow: Mashinostroenie, 1985, vol. 1.
4. Sviridov, V.V., Vorob'eva, T.N., Gaevskaya, T.V., and Stepanova, L.I., *Khimicheskoe osazhdenie metallov iz vodnykh rastvorov* (Chemical Deposition of Metals from Water Solutions), Grinberg, A.A., Ed., Izd. Universitetskoe, 1987.

ISSN 1068-3755, Surface Engineering and Applied Electrochemistry, 2008, Vol. 44, No. 5, pp. 370–372. © Allerton Press, Inc., 2008.
Original Russian Text © A.V. Khlyustova, A.I. Maksimov, M.S. Khorev, 2008, published in Elektronnaya Obrabotka Materialov, 2008, No. 5, pp. 34–36.

ELECTRICAL PROCESSES IN ENGINEERING AND CHEMISTRY

Radiation of Metal Atoms in the Plasma of an Atmospheric Pressure Glow Discharge with an Electrolyte Cathode

A. V. Khlyustova, A. I. Maksimov, M. S. Khorev

Institute of Solution Chemistry, Russia Academy of Sciences,
ul. Academicheskaya 1, Ivanovo, 153045 Russia
E-mail: kav@isc-ras.ru

Received January 11, 2008

Abstract—The radiation of atoms of lithium (λ = 670 nm), sodium (λ = 588–589 nm), and calcium (λ = 657.2 nm, triplet) in an atmospheric pressure glow discharge plasma when the solution of the salt of the respective metal serves as a cathode is experimentally studied. It is shown that, in a system with solution circulation, the intensity of the mentioned lines during the discharge burning process rises tending to a constant limit value. The characteristic time of the establishing of the radiation intensity asymptotic value for the solutions of lithium, sodium, and calcium salts is 22, 5.5, and 9.5 minutes, respectively. These variations correlate with the previously observed growth of the rate of the nonequilibrium transfer of the solution components into the plasma zone. It is also found that the relationship between the line intensity and the discharge current is characterized by the presence of the threshold current (10–15 mA). The transfer from an alkaline solution to an acid one is attended with an increase of the intensity of the radiation of metal atoms.

DOI: 10.3103/S1068375508050050

INTRODUCTION

The burning of the glow discharge with the electrolyte cathode is attended with optic radiation significantly contributed to by the atom lines of the metals whose salts are in the solution [1]. The mechanisms of the transfer of the metal atoms into the plasma zone and their excitation are as yet little understood. Detailed information on the association of the atom radiation intensity with the solution properties and the discharge parameters is necessary in order to ascertain those mechanisms. The aim of this work is to obtain such data.

EXPERIMENTAL TECHNIQUE

A schematic diagram of the installation is presented in Fig. 1. The design of the plasma-solution cell displayed in the figure is similar to the one described in paper [2] and allows one to maintain the solution level constant during the discharge burning process, thus stabilizing the discharge zone length. The studied spectral lines were isolated using plasma monochromator UM 2 and recorded with the help of photocell F 23 with an amplifier. The experiments were carried out in the circulating system. The solution flow was 60 ml/min. The potential electrode (anode) was located at a distance of 2–3 mm from the solution surface. The anode was made of a pointed copper rod 3 mm in diameter. The ground electrode (cathode) was placed into the cell outer housing. Solutions of LiCl, NaCl, and $CaCl_2$ with concentrations of 0.01–0.1 mol/l were used as the electrolyte cathodes. The discharge current was varied in the range from 10 to 75 mA. The solution acidity was changed by addition of HCl (pH = 1) or NaOH (LiOH) (pH = 12). It should be noted that the solution of LiOH was added

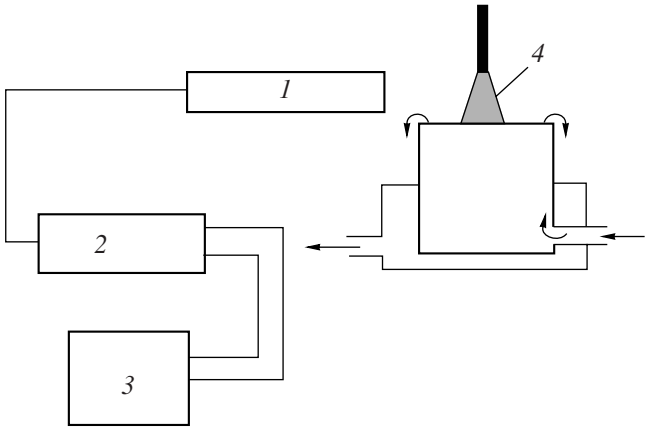

Fig. 1. Schematic diagram of the installation for spectral investigations. *1*, monochromator UM 2; *2*, radiation signal recording and amplifying assembly (photocell F 23); *3*, recording device; *4*, the discharge positive column zone. The solution movement in the cell is shown by arrows.

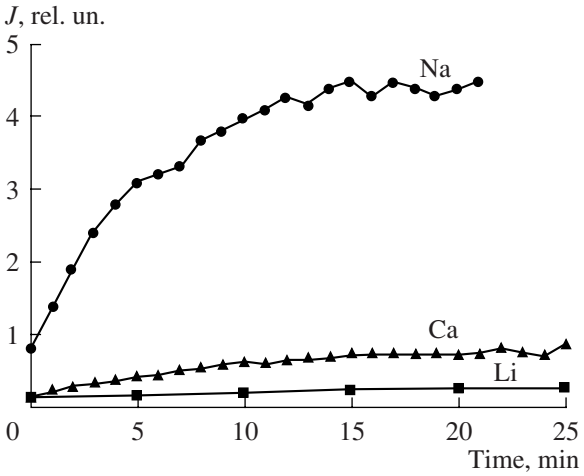

Fig. 2. Variation of the intensities of the spectral lines of metal atoms during the discharge burning process. The discharge current is 30 mA, and the soluted salt concentration is 0.06 mol/l.

to the solution of NaCl. This process was carried out to prevent the change of the sodium ion concentration in the solution.

RESULTS AND DISCUSSION

The experiment shows that the intensity of the metal atom lines after the ignition of the discharge increases converging asymptotically to a constant limit value (Fig. 2). The time dependency of the intensity of the lines may be described by the expression

$$I = I_0 + I_\infty(1 - e^{-t/\tau}), \quad (1)$$

where I_0 is the initial value of the intensity, $I_0 + I_\infty$ is its asymptotic limit value, and τ is the characteristic time of the steady state determination. The results of the experimental data treatment using the relation (1) are presented in the table.

It should be noted that the fact of the rise of the radiation intensity with the asymptotic approach to the steady value correlates itself with the previously observed change of the rate of the nonequilibrium transfer of the solution components into the plasma zone under the action of the glow discharge [3]. The characteristic time for the system to reach a steady state is close too. We think it means the commonness of the mechanism for these effects. As we suggest, the reason for them is the change of the electrolyte aqueous solution structure as a result of the ion bombardment appearing as partial damage of the hydrogen bond network relaxed relatively slowly after the shutdown of the discharge. The nonlinear relationship between the radiation intensity and the discharge current (Fig. 3) and the influence of the solution acidity (Fig. 4) could also be connected with this process. In conformity with the known data [1], the dependency of the radiation intensity on the discharge current is nonlinear and indicates the presence of the current threshold value radiation of atoms being absent at lower ones. The transfer from the alkaline solution to the acid one causes the growth of the atom radiation intensity. This conclusion correlates qualitatively with the results of work [2]. However, according to their data, the atom radiation is almost absent at pH = 4, but our data show that, even in the

Table

Solution	I_0, rel. un.	$I_0 + I_\infty$, rel. un.	τ, min
LiCl	0.12	0.33	22.38
NaCl	0.8	4.59	5.54
$CaCl_2$	0.13	0.83	9.53

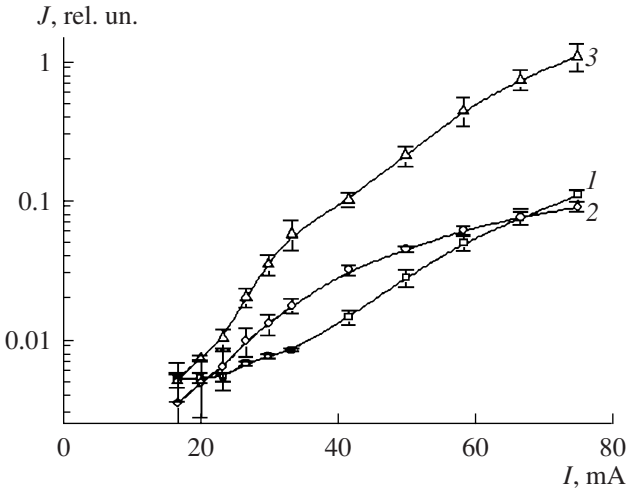

Fig. 3. The discharge current effect on the intensity of the spectral lines of the soluted metal atoms. *1*, Li (λ = 670 nm); *2*, Na (λ = 588–589 nm); *3*, Ca (λ = 657.2 nm, triplet). The soluted salt concentration is 0.09 mol/l.

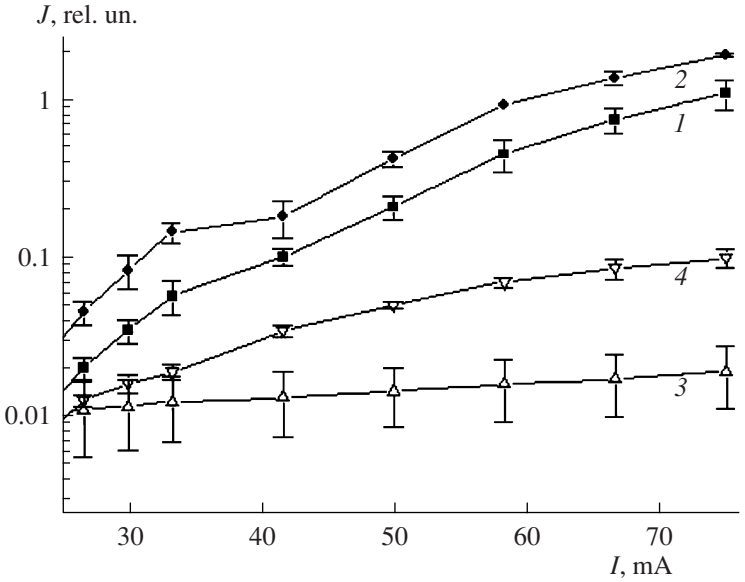

Fig. 4. The solution acidity effect on the intensity of the spectral lines of Na and Ca. *1*, Ca (pH = 7); *2*, Ca (pH = 0.98); *3*, Na (pH = 7); *4*, Na (pH = 0.94). The soluted salt concentration is 0.06 mol/l.

alkaline medium, its intensity is somewhat lower than in the acid one.

REFERENCES

1. Maksimov, A.I., Titov, V.A. and Khlyustova, A.V., Radiation of Glow Discharge with Electrolyte Cathode and Processes of Transfer of Neutral and Charged Particles from Solution into Plasma, *Chim. Vys. Energ.* 2004, vol. 38, no. 3, pp. 227-230.
2. Cserfalvi, T., Mezei, P. and Apai, P., Emission Studies on a Glow Discharge in Atmospheric Pressure Air Using Water as a Cathode, *J. Phys. D: Appl. Phys*., 1993, vol. 26, pp. 2184–2188.
3. Khlyustova, A.V., Maksimov, A.I., Dydykin, M.G. and Polyakov, M.S., Study of Chemical Reactions during Discharge in Water and Aqueous Solutions of Organic Substances, *Electr. Obrab. Mater.*, 2007, no. 5, pp. 48–51 [Surf. Eng. Appl. Electrochem., (Engl. Transl.) vol. 43, no. 5, pp.344–346].

ISSN 1068-3755, Surface Engineering and Applied Electrochemistry, 2008, Vol. 44, No. 5, pp. 373–376. © Allerton Press, Inc., 2008.
Original Russian Text © I.I. Beril, M.K. Bologa, S.I. Beril, 2008, published in Elektronnaya Obrabotka Materialov, 2008, No. 5, pp. 37–41.

ELECTRICAL PROCESSES IN ENGINEERING AND CHEMISTRY

On Theory of Electric Conductivity of Low-Conducting Liquid in the Field of Injecting Electrodes (Mobility Dependence)

I. I. Beril[a], M. K. Bologa[a], and S. I. Beril[b]

[a] *Institute of Applied Physics, Academy of Sciences of Moldova, ul. Academiei 5, Kishinev, MD-2028 Republic of Moldova*
E-mail: mbologa@phys.asm.md

[b] *T.G. Shevchenko Dniestr State University, ul. Oktyabrya 25, Tiraspol, Republic of Moldova*

Received February 6, 2008

Abstract—Calculation of the mobility of free electrons at the injection of electrons from high voltage needle electrodes on a liquid surface is conducted. Applicability of the methods of solid state physics is validated. The dependence of the mobility on the electric field intensity ~$E^{-1/3}$ is achieved on account of the dependence of the free electron wave function on the electric field intensity. It is substantiated that the distribution function with respect to the energies of electrons does not depend on the electric field intensity.

DOI: 10.3103/S1068375508050062

The relationship between the concentration of low-conducting liquid free electrons and the electric intensity and temperature was previously obtained [1].

The concentration of free electrons hardly depends on the field intensity up to the pre-break-down values.

The function of the conductivity distribution with respect to the electron energies doesn't depend on the field intensity as well and, at low concentrations of impurity centers, has the maxwell form.

The applicability of the methods of solid state physics for the calculation of the electrophysical characteristics of low-conducting liquids with periodically located atomic impurities is validated [1].

The liquid current-voltage characteristic nonlinearity can be explained by the dependence of the mobility of the current carriers on the intensity.

The estimation of the polaron effect gives a small value of the polaron bond constant determined by the energy of interaction of the band electron with phonons; it is computed according to the perturbation theory and, in the case of the weak polaron bond, has the form [2]

$$\alpha = \frac{1}{\sqrt{2}}\left(\frac{1}{\varepsilon_\infty} - \frac{1}{\varepsilon_1}\right)\frac{e^2\sqrt{m^*}}{\hbar^{\frac{3}{2}}\omega^{\frac{1}{2}}}, \quad (1)$$

where ε_∞ and ε_1 are the dielectric constants determined at high and low frequencies, respectively; e is the electron charge; m^* is the electron effective mass; $\hbar$ is the Plank constant; and ω is the frequency of the phonon oscillations.

For the refined sunflower-seed oil previously measured [3], $\varepsilon_\infty = 3.15\varepsilon_0$, $\varepsilon_1 = 3.5\varepsilon_0$,

$$\frac{m^*}{m_e} = 1 + \frac{\alpha}{6}. \quad (2)$$

From (1) and (2) for acoustic phonons, whose contribution to α is the biggest, we obtain $m^* \cong m_e$ and $\alpha \sim 5 \times 10^{-16}$, that is, $\alpha \ll 1$. The small value of α is caused by the fact that, for composite glycerides of fatty acids (sunflower-seed oil being one of them), the molecules have large molecular weights, little dipole moment, and the polarization of such molecules by the electrons is negligibly small; i.e., α is almost zero. The dimensionless constant α is equal to the ratio of the polaron energy difference in the polaron zone to the activation energy of the scattering impurity centers $\alpha = \Delta E_n/\Delta E$; hence, $\Delta E = \alpha E$ is a small quantity.

The mobility of the free electrons is

$$\mu = \frac{e}{m_e}\langle\tau\rangle, \quad (3)$$

where $\langle\tau\rangle$ is the averaged distribution with respect to the energies of the electron state relaxation time [4]

$$\frac{1}{\tau} = \sum_\theta (1 - \cos\theta) W(\theta), \quad (4)$$

where θ is the angle of scattering on impurity ions, and $W(\theta)$ is the probability of transitions between the electron states.

Let us calculate the coefficient function of the transition between the electron states in the conductivity band:

$$M_1 = \int \psi_1(\xi_1)\hat{V}\psi_2(\xi_2)r^2(dr\sin(\theta))d\theta d\varphi,$$

where $\hat{V} = -eEx$; $\psi_1(\xi_1) = A'\Phi(-\xi_1)$; $\Phi(\xi_1) = \frac{1}{\sqrt{\pi}}\int_0^\infty \cos\left(\frac{u^3}{3} + \xi_1\right)du$ is the Airy function; $\xi_1 = \left(x + \frac{\varepsilon_1}{eE}\right)\left(\frac{2m_e eE}{\hbar^2}\right)^{\frac{1}{3}}$; $A' = \frac{(2m_e)^{\frac{1}{3}}}{\pi^{\frac{1}{2}}(Ee)^{\frac{1}{6}}\hbar^{\frac{2}{3}}}$; and $\psi_2(\xi_2)$ is defined similarly.

$$\frac{2A'eE}{\sqrt{\pi}}\int_0^\infty\int_0^\pi\int_0^{2\pi} r^3\sin^2(\theta)d\theta d\varphi dr\int_0^\infty \cos\left(\frac{u^3}{3} - u\left(r\sin(\theta)\cos(\theta) + \frac{\varepsilon_1}{eE}\right)\left(\frac{2m_e eE}{\hbar^2}\right)\right)du$$

$$\times\int_0^\infty \cos\left(\frac{u^3}{3} - u\left(r\sin(\theta)\cos(\theta) + \frac{\varepsilon_2}{eE}\right)\left(\frac{2m_e eE}{\hbar^2}\right)^{\frac{1}{3}}\right)du.$$

Let's integrate over φ:

$$-2A'eE\int_0^\infty\int_0^\pi r^3\sin^2(\theta)d\theta dr\int_0^\infty J_1(2ubr\sin\theta)\left[-\cos^2\frac{u^3}{3}\sin(uba_1 + uba_2)\right.$$

$$\left. + 2\sin\frac{u^3}{3}\cos\frac{u^3}{3}\cos(uba_1 + uba_2) + \sin^2\frac{u^3}{3}\sin(uba_1 + uba_2)\right]du,$$

where $b = \left(\frac{2meE}{\hbar^2}\right)^{\frac{1}{3}}$, $a_1 = \frac{\varepsilon_1}{eE}$, $a_2 = \frac{\varepsilon_2}{eE}$, and J_1 is Bessel's function.

Let's integrate over θ and over u:

$$4A'eE\int_0^\infty\left\{\left[\frac{\pi}{2br} - \frac{3\pi}{br} - \frac{1}{6br}\sum_{k=0}^\infty \frac{[(-1)^k + 1]\beta^{k+1}}{(k+1)!}\left(\frac{1}{3}\right)^{\frac{k+1}{3}}\Gamma\left(\frac{k+1}{3}\right)\cos(-2k+1)\frac{\pi}{6}\right] - \frac{\pi}{2br} - \frac{\pi}{br} - \frac{1}{6(br)^2}\right.$$

$$\times\sum_{k=0}^\infty \frac{[(-1)^k + 1]\{br + b(a_1+a_2)^{k+1} - (b_2 - b(a_1+a_2)^{k+1})\}}{(k+1)!}\left(\frac{2}{3}\right)^{\frac{k+1}{3}}\Gamma\left(\frac{k+1}{3}\right)\cos(-2k+1)\frac{\pi}{6} + \frac{\pi}{2br} + \frac{1}{3br}$$

$$\times\sum_{k=0}^\infty \frac{[(-1)^k + 1]\beta^{k+1}}{(k+1)!}\left(\frac{2}{3}\right)^{\frac{k+1}{3}}\Gamma\left(\frac{k+1}{3}\right)\sin(-2k+1)\frac{\pi}{6}\left.\right] - \frac{1}{12(br)^2}$$

$$\left.\times\sum_{k=0}^\infty \frac{[(-1)^k + 1]\{br + b(a_1+a_2)^{k+2} - (b_2 - b(a_1+a_2)^{k+2})\}}{(k+2)!}\left(\frac{1}{3}\right)^{\frac{k+1}{3}}\Gamma\left(\frac{k+1}{3}\right)\cos(-2k+1)\frac{\pi}{6}\right\}r^3dr,$$

where $\beta = b(a_1 + a_2)$.

At $\varepsilon_1 \sim \varepsilon_2 \sim 3/2kT$, $a_1 \sim a_2 \sim 10^{-8} \ll 1$, $b \cong 10^8 \gg 1$, $m = 9.1 \times 10^{-31}$ kg, $\hbar = 10^{-34}$ J s, $E_1 = 3 \times 10^5$ V/m, and $a_1 b \sim a_2 b \cong 1$, as under all sums, there is present the multiplier $b^k(a_1 + a_2)^{k+1}$ or $b^{k+1}(a_1 + a_2)^{k+2}$; i.e., $(a_1 + a_2)$ is always to a power of 1 more. Therefore, $b^k(a_1 + a_2)^{k+1} \ll 1$ or $b^{k+1}(a_1 + a_2)^{k+2} \ll 1$, so, in sum, we can restrict ourselves to $k = 0$. In addition, in the integration element, there is absent the cutting factor with respect to r; thus, at integration over r, it

is necessary to confine ourselves to the volume with unit radius:

$$4A'eE\int_0^\infty\Bigg\{\frac{\pi}{2br}-\frac{1}{3br}\sum_{k=0}^{3}\frac{[(-1)^k+1]\beta^{k+1}}{(k+1)!}\left(\frac{1}{3}\right)^{\frac{k+1}{3}}\Gamma\left(\frac{k+1}{3}\right)\cos(-2k+1)\frac{\pi}{6}-\frac{3\pi}{2b}+-\frac{1}{b^3r}$$
$$\times\sum_{k=0}^{3}\frac{[(-1)^k+1]\{b^{k+1}[r+(a_1+a_2)]^{k+1}-b^{k+1}[r-(a_1+a_2)^{k+1}]\}}{(k+1)!}\left(\frac{2}{3}\right)^{\frac{k+1}{3}}\Gamma\left(\frac{k+1}{3}\right)\cos(-2k+1)\frac{\pi}{6}+\frac{\pi}{2b}+\frac{1}{3b}$$
$$\times\sum_{k=0}^{3}\frac{[(-1)^k+1]\beta^{k+1}}{(k+1)!}\left(\frac{2}{3}\right)^{\frac{k+1}{3}}\Gamma\left(\frac{k+1}{3}\right)\sin(-2k+1)\frac{\pi}{6}\Bigg]-\frac{1}{12b^2r}$$
$$\times\sum_{k=0}^{3}\frac{[(-1)^k+1]b^{k+2}\{[r+(a_1+a_2)]^{k+1}+[r-(a_1+a_2)]^{k+2}\}}{(k+2)!}\left(\frac{1}{3}\right)^{\frac{k+1}{3}}\Gamma\left(\frac{k+1}{3}\right)\cos(-2k+1)\frac{\pi}{6}\Bigg\}r^2dr \tag{5}$$
$$\longrightarrow\frac{4(2m)^{\frac{1}{3}}eE}{\sqrt{\pi}(eE)^{\frac{1}{6}}\hbar^{\frac{2}{3}}}\left[\frac{\pi\hbar^{\frac{2}{3}}}{6(2m)^{\frac{1}{3}}(eE)^{\frac{1}{3}}}-\frac{0.42(\varepsilon_1+\varepsilon_2)}{eE}-0.75\left(\frac{2mE}{\hbar^2}\right)^{\frac{2}{3}}\frac{\varepsilon_1+\varepsilon_2}{(eE)^3}\right]$$
$$=a_1(eE)^{\frac{1}{3}}-\frac{a_2(\varepsilon_1+\varepsilon_1)}{(eE)^{\frac{1}{6}}}-\frac{a_3(\varepsilon_1+\varepsilon_1)^3}{(eE)^{\frac{3}{2}}}=M_1.$$

The probability of the transition is

$$W=\frac{2\pi}{\hbar}|M_1|^2\delta(\varepsilon_k-\varepsilon_i-\Delta\varepsilon), \tag{6}$$

where ε_k and ε_i are the final and the initial energy of the electron, and $\Delta\varepsilon$ is the difference of the electron energies:

$$\varepsilon_k-\varepsilon_i=\frac{p_1^2}{2m}-\frac{p_2^2\cos^2\nu}{2m}=\frac{p_1^2}{2m}(1-\cos^2\nu),$$

where ν is the scattering angle.

$$\frac{1}{\tau}=\int_\nu\int_p(1-\cos\nu)W(p,\nu)$$
$$\times\delta\left[\frac{p_1^2}{2}(1-\cos^2\nu)-\Delta\varepsilon\right]d\nu dp.$$

After integrating over ν, we obtain

$$\frac{2\pi}{\hbar}\int_\nu(A_1\varepsilon+A_2\varepsilon^2+A_3\varepsilon^3+A_4\varepsilon^4+A_5\varepsilon^6)\sqrt{\frac{m}{2\varepsilon}}d\varepsilon,$$

where $A_1=-8.21a_1a_2(eE)^{1/3}$, $A_2=\frac{0.587a_2^2}{(2m)^2(eE)^{\frac{1}{3}}}$, $A_3=\frac{28.5a_1a_2}{eE}$, $A_4=-6.42a_2a_3$, $A_5=\frac{48.5a_3^2}{(eE)^3}$.

$$\frac{\pi(2m)^{\frac{1}{2}}}{\hbar}$$
$$\times\left(\frac{2}{3}A_1\varepsilon^{\frac{3}{2}}+\frac{2}{5}A_2\varepsilon^{\frac{5}{2}}+\frac{2}{7}A_3\varepsilon^{\frac{7}{2}}+\frac{2}{9}A_4\varepsilon^{\frac{9}{2}}+\frac{2}{13}A_5\varepsilon^{\frac{13}{2}}\right),$$

as $\varepsilon\sim0.04$ eV. Then, the estimation of $A_1, A_2, A_3, A_4, A_5, A_6$ gives

$$A_1\varepsilon^{\frac{3}{2}}\gg A_2\varepsilon^{\frac{5}{2}}\gg A_3\varepsilon^{\frac{7}{2}}\gg A_4\varepsilon^{\frac{9}{2}}\gg A_5\varepsilon^{\frac{13}{2}}.$$

and

$$\frac{2\pi m^{\frac{1}{2}}}{3\hbar}A_1\varepsilon^{\frac{3}{2}}=\frac{8\pi m^{\frac{5}{6}}(eE)^{\frac{1}{3}}\varepsilon^{\frac{2}{3}}}{\hbar^{\frac{5}{3}}}.$$
$$\tau=\frac{\hbar^{\frac{5}{3}}}{8\pi m^{\frac{5}{6}}(eE)^{\frac{1}{3}}\varepsilon^{\frac{3}{2}}}. \tag{7}$$

Let's average with respect to the Maxwell distribution:

$$\langle\tau\rangle=\frac{\hbar^{\frac{5}{3}}}{8\pi m^{\frac{5}{6}}(eE)^{\frac{1}{3}}}\frac{\int_\varepsilon\varepsilon^{-\frac{3}{2}}e^{-\frac{\varepsilon}{kT}}d\varepsilon}{\int_\varepsilon e^{-\frac{\varepsilon}{kT}}d\varepsilon},$$

$$\frac{\varepsilon}{kT} = x, \quad d\varepsilon = kTdx,$$

$$\int_{\varepsilon} \varepsilon^{\frac{3}{2}} e^{-\frac{\varepsilon}{kT}} d\varepsilon = \frac{1}{(kT)^{\frac{1}{2}}} \int_{\varepsilon} \frac{e^{-x}}{x^{\frac{3}{2}}} dx$$

$$= \left[-\frac{2}{\sqrt{x}} e^{-x} - 2\sqrt{\pi} erf\left(\sqrt{\frac{\varepsilon}{kT}} \right) \right] \frac{1}{(kT)^{\frac{1}{2}}}$$

$$= \frac{1}{(kT)^{\frac{1}{2}}} \left[-\frac{2(kT)^{\frac{1}{2}}}{\sqrt{\varepsilon}} e^{-\frac{\varepsilon}{kT}} - 2\sqrt{\pi} erf\left(\sqrt{\frac{\varepsilon}{kT}} \right) \right] \quad (8)$$

$$= -\frac{2}{\sqrt{\varepsilon}} e^{-\frac{\varepsilon}{kT}} - 2\sqrt{\frac{\pi}{kT}} erf\left(\sqrt{\frac{\varepsilon}{kT}} \right),$$

$$\int_{\varepsilon} e^{-\frac{\varepsilon}{kT}} d\varepsilon = -kTe^{-\frac{\varepsilon}{kT}},$$

$$\frac{\int_{\varepsilon} \varepsilon^{\frac{3}{2}} e^{-\frac{\varepsilon}{kT}} d\varepsilon}{\int_{\varepsilon} e^{-\frac{\varepsilon}{kT}} d\varepsilon} = \frac{2}{\sqrt{\varepsilon} kT} + \frac{2\sqrt{\pi}}{(kT)^{\frac{3}{2}}} e^{\frac{\varepsilon}{kT}} erf\left(\sqrt{\frac{\varepsilon}{kT}} \right).$$

The second member at room temperature is $\gg$ than the first one.

Restricting by the second member, we obtain

$$\langle \tau \rangle = \frac{\hbar^{\frac{5}{3}} \sqrt{\pi} e^{\frac{\varepsilon}{kT}} erf\left(\sqrt{\frac{\varepsilon}{kT}} \right)}{4\pi m^{\frac{5}{6}} (eE)^{\frac{1}{3}} (kT)^{\frac{3}{2}}}. \quad (9)$$

The electron mobility is

$$\mu = \frac{e\hbar^{\frac{5}{3}} \sqrt{\pi} e^{\frac{\varepsilon}{kT}} erf\left(\sqrt{\frac{\varepsilon}{kT}} \right)}{4\pi m^{\frac{11}{6}} (eE)^{\frac{1}{3}} (kT)^{\frac{3}{2}}}. \quad (10)$$

With regard to the first member,

$$\mu = \frac{e\hbar^{\frac{5}{3}}}{4\pi m^{\frac{11}{6}} (eE)^{\frac{1}{3}}} \left[\frac{1}{\sqrt{\varepsilon} (kT)^{\frac{1}{2}}} + \frac{\sqrt{\pi} e^{\frac{\varepsilon}{kT}}}{(kT)^{\frac{3}{2}}} erf\left(\sqrt{\frac{\varepsilon}{kT}} \right) \right]. \quad (11)$$

Using the formula for the concentration of electrons from (1) and mobility (11), for the current density, we obtain

$$j = \frac{N_{i.c.} N_c (e\hbar)^{\frac{5}{3}} \varepsilon^{\frac{2}{3}}}{4\pi (N_{i.c.} - N_{c.i.c.}) m^{\frac{11}{6}}} \left[e^{-\frac{\Delta E}{kT}} + \frac{8\hbar^{\frac{4}{3}} (e\varepsilon)^{\frac{7}{3}}}{3m^{\frac{7}{16}} \Delta E^{\frac{5}{2}}} \right] \times \left[\frac{1}{\sqrt{\varepsilon} (kT)^{\frac{1}{2}}} + \frac{\sqrt{\pi} e^{\frac{\varepsilon}{kT}}}{(kT)^{\frac{3}{2}}} erf\left(\sqrt{\frac{\varepsilon}{kT}} \right) \right]. \quad (12)$$

With allowance made for the smallness of the second member in the first square brackets and the first one in the second square brackets,

$$j = \frac{N_{i.c.} N_c (e\hbar)^{\frac{5}{3}} \xi^{\frac{2}{3}} e^{-\frac{\Delta E}{kT}} e^{\frac{\varepsilon}{kT}} erf\left(\sqrt{\frac{\varepsilon}{kT}} \right)}{4\sqrt{\pi} (N_{i.c.} - N_{c.i.c.}) m^{\frac{11}{6}} (kT)^{\frac{3}{2}}}. \quad (13)$$

For comparison with the experiment, it is necessary to analytically determine the ion electric conductivity with certain constants and allow it in the current density.

REFERENCES

1. Beril, I.I., Bologa, M.K. and Beril, S.I., On the Theory of Dielectric Liquid Electric Conductivity in a Field of Injecting Electrodes (Concentration Dependence) *Electr. Obrab. Mater.* [Surf. Eng. Appl. Electrochem. (Engl. Transl.), vol. 44, no. 4, pp. 297–300], 2008, no. 4, pp. 55–59.
2. Feintman, R., *Statisticheskaya mekhanika* (Statistical Mechanics), Moscow: Mir, 1978.
3. Bologa, M.K. and Beril, I.I., *Rafinatsiya podsolnechnogo masla v elektricheskom pole* (Fining Sunflower-Seed Oil in Electric Field), Kishinev: Shtiintsa, 1984.
4. Stilbans, L.S., *Fizica poluprovodnikov* (Physics of Semiconductors), Moscow: Sovetskoe radio, 1967.

ISSN 1068-3755, Surface Engineering and Applied Electrochemistry, 2008, Vol. 44, No. 5, pp. 377–382. © Allerton Press, Inc., 2008.
Original Russian Text © L.M. Vasilyak, F.I. Vysikailo, S.V. Mitin, A.S. Tivkov, 2008, published in Elektronnaya Obrabotka Materialov, 2008, No. 5, pp. 42–48.

ELECTRICAL PROCESSES IN ENGINEERING AND CHEMISTRY

Cumulative Processes on a Dust Particle in Plasma

L. M. Vasilyak[a], F. I. Vysikailo[b], S. V. Mitin[c], and A. S. Tivkov[b]

[a] *Joint Institute for High Temperatures, Russian Academy of Sciences, ul. Izhorskaya 13/19, Moscow, 127412 Russia*
[b] *FGU Technological Institute for Superhard and Novel Carbon Materials, ul. Tsentral'naya 7a, Troitsk, Moscow oblast, 142191 Russia*
[c] *FGUP Bochvar Institute of Inorganic Materials, ul. Rogova 5a, Moscow, 123060 Russia*
E-mail: vasilyak@yandex.ru

Received March 13, 2008

Abstract—Processes of asymmetric ionization and cumulation of electric field and electron and ion flows can develop near the surface of charged dust particles in plasma. In the region of cumulation asymmetry on heating, the particle surface and ion momentum transfer arises; as a result, the dust particle moves in the plasma with high velocity.

DOI: 10.3103/S1068375508050074

INTRODUCTION

Nonequilibrium plasma with a condensed dispersed phase is used in different plasma-chemical technologies for modification and hardening of surfaces at application of protective coatings. In a number of cases, the presence of dust particles in the plasma, on the contrary, is undesirable, and they are formed constantly at interaction of the plasma with electrodes, for example, at manufacture of electronic chips and other products of microelectronics using HF discharge when electron or ion beams act on the surface and at interaction of high temperature plasma in tokamaks with the wall. Therefore, the problem of removal of dust particles from the working volume is topical, as well as the control of their motion.

The particles in the plasma acquire a large negative charge; (10^4–10^5) electron charges; and, under certain conditions, the plasma with charged dust particles serves as an object with strong Coulomb interaction and the ordered dust structures resemble a crystal [1]. These dissipative crystals [2] are called Coulomb crystals [1]. The formation of structures from dust particles of a micron size was observed experimentally in the low pressure plasma in microwave and glowing discharges [1]. The processes of formation of structures of dust particles are influenced strongly by the properties of the ambient plasma. Dust particles with large charge and their ordered macrostructures after they are formed should change the local plasma properties [3], the electric fields in it, and the flows of charged particles, since the structure attracts ion and electron flows for maintaining its charge. In all the works devoted to dusty plasma, as a rule, spherical symmetry of energy–mass–momentum flows to the dust particle is assumed [1].

However, it is known from a number of experiments and theoretical works [2, 4, 5] that cumulative-dissipative structures, plasmoids, with complex asymmetric multidimensional profiles of the self-consistent cumulative electric field can be formed in a gas discharge. According to [6], cumulation is the concentration in a small volume of a force, energy, or other physical quantity. The presence of a large charge of dust particles may result in the formation of regions of focusing (cumulation) of the electric field strength and, therefore, in local cumulation of electron and ion flows. Plasmoids with the system of energy–mass–momentum flows of charged particles are the analogues of cumulative-dissipative structures of the type of Benard cells or fractures (with focused energy, mass, and momentum flows) in solids [2]. It is known that, in Benard cells [7], first, diffusion flows due to the temperature gradient are formed; then, focusing convective processes are self-enhanced. The self-organizing vortex structures of the type of Benard cells can be formed in plasma [5] as well. Similar to convective Benard cells, self-organization of convective and diffusion processes takes place on dust particles as their charge is increased. The plasma is polarized, and the dipole moment of the dust particle and the ambient plasma appears. As a result, the asymmetry of cumulating convective flows and, therefore, the asymmetry of cumulation of the self-consistent electric field are established. This phenomenon is due to the nonlinearity of convective transfer processes [2].

It is known that particles with large kinetic energy [8, 9] were observed in experiments along with ordered particles. They can move for a long time and travel considerable distances without noticeable loss of velocity. If this motion of a dust particle were realized as a result of random spherically symmetric processes, it should lose velocity due to viscous friction and collision with other dust particles at distances comparable with the characteristic distances between dust particles. In par-

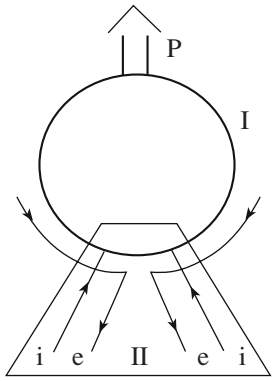

Fig. 1. Schematic diagram of possible cumulation of (e) electron and (i) ion energy and mass flows to the dust particle. P is the resulting force acting on the charged microparticle with the self-formed "reactive jet." In region I, the flows are close to spherically symmetric ones; in cone II, the cumulative jet of the plasma flows is formed and electric field cumulation takes place; and, in region II, bicumulation of the electron and ion flows takes place.

ticular, when such a particle passed with a velocity of 6–8 cm/s through the region of ordered dusty plasma, perturbation in the dust structure in the form of the Mach cone [8] was observed. The mechanisms of long-term rectilinear motion of fast particles through the whole plasma gap were not explained in [8]. In [9], the possibility of motion of a dust particle under a monolayer of other dust particles due to the action of the ion flow on it was substantiated; however, this mechanism cannot explain the motion of particles in other directions or between the layers.

In this work, nonsymmetric cumulative convective processes in dusty plasma are considered and the mechanism of long-term motion of dust particles due to the formation of nonsymmetric cumulative-dissipative plasma structures around them is proposed. In dissipative structures, a special flow geometry is formed and the corresponding cumulative processes accelerate the energy and mass transfer, i.e., accelerate due to cumulation of energy and the electric field strength convective processes of dissipation of the external source energy [2]. This is the objective of formation of cumulative-dissipative structures, such as near-electrode spots, plasma filaments, etc., in a medium activated by an external potential. Processes of inhomogeneous (nonsymmetric) cumulation (focusing) and self-focusing of flows may result not only in reactive ejection of the cathode material to the discharge gap and the anode, as in the case of focusing of ion flows in cathode spots near the cathode [4], but also in the formation of reactive drag of dust particles. The formation of these "rocket engines" with bicumulative asymmetric "fuel" (electron and ion flows) fed to dust particles from the external nonlinear plasma environment represents a new field of the physics of nonlinear cumulative-reactive systems not studied yet, which can certainly be used in practice.

The proposed schematic diagram of operation of the cumulative-reactive system created by the plasma near the surface of a dust particle is shown in Fig. 1. This diagram is similar to the model of operation of a cathode spot on a metal cathode [2, 4]. Equal flows of ions and electrons are incident on the dust particle. The flows of charged particles of the plasma are cumulated due to the difference of the drift velocities of electrons and ions. Electrons knocked out of the dust particle are accelerated in the field of the incident ions in the direction toward the anode and focus plasma ions to the electron beam. Ions focused by the electron flow knock more electrons out of the dust particle in the region of the cumulative jet. The process is self-developed, self-enhanced, and self-focused. This successive cumulation of ion flows on the focused electron flow is called bicumulation [2]. Electric field cumulation can be limited by the processes of diffusion and neutrality violation. The simulation of dynamic processes in the plasma with a condensed disperse phase is a complex non-steady-state dynamically self-consistent problem in which it is necessary to take into account additional processes that are seldom considered, such as thermophoresis, specific geometric features of cumulative-ion phoresis, and so on. This problem is beyond the framework of spherically symmetric models discussed in [1], in which the following topics were studied: the potentials of a charged dust particle, the average electron temperatures in a Seitz–Wigner cell, more precise determination of the Debye screening radius, the nonideality parameter, and the Coulomb parameter of interaction of charged dust particles. It should be noted that regions I and II (Fig. 1) are described by the system of common hydrodynamic equations with account for the quasi-neutrality violation. According to the model, the electron flow to the dust particle is determined by the diffusion processes, and electrons organized in a convective cumulative jet (Fig. 1) leave the dust particle. In this case, the flows are self-organized in the external electric field and form cumulative-dissipative structures with reactive jets, spherically nonsymmetric cumulation of the electric field, ion and electron flows, and local inhomogeneous heat release. The existing asymmetry of the ion and electron flows in the discharge amplified by cumulative processes provides the observed effect of long-term motion of fast dust particles.

The region of cumulation of convective ambipolar flow was simulated in the following formulation.

STATEMENT OF THE PROBLEM

The weakly ionized plasma around the dust particle consists of electrons, positive ions, and the neutral component. It will be assumed that the density of molecules (or atoms) of the neutral medium N is constant, and the coefficients of mobility of the electrons and ions are known functions of the parameter E/N. Let $\nabla \times \boldsymbol{E} = 0$. Let us use the common system of hydrodynamic trans-

port equations resulting after simple transformations with account for Poisson's equation in the following system of equations:

$$\partial n_i/\partial t + \nabla \boldsymbol{\Gamma}_i = I_i - R_i, \tag{1}$$

$$\begin{aligned} \boldsymbol{j} &= \varepsilon_0 \partial \boldsymbol{E}/\partial t + e\boldsymbol{E}(\mu_e n_e + \mu_i n_e) \\ &+ \mu_i \varepsilon_0 \boldsymbol{E}(\nabla \boldsymbol{E}) + e\nabla(D_\perp n_e) - \nabla D_i(e n_e + \varepsilon_0 \nabla \boldsymbol{E}), \end{aligned} \tag{2}$$

where j is the total current density; e, n_e, μ_e, and $D_\perp$ are the charge, density, mobility, and diffusion coefficient for the electrons, respectively; I_i and R_i correspond to generation and loss of ions and electrons, respectively; Γ_i, μ_i, and D_i are the flow, mobility, and diffusion coefficient for the ions, respectively; E is the electric field strength; and ε_0 is the dielectric constant.

System of equations (1), (2) in the volume of the gas discharge plasma far from the electrodes (which allows one to avoid problems related to boundary conditions) is usually solved using the perturbation theory where displacement currents are neglected [2, 10, 11]. The order of separate terms in (2) with respect to the term with the drift structure is determined as $\Omega\tau_M$, 1, $(\mu_k/\mu_J)l_E/L$, l_u/L. Here, Ω is the characteristic charge variation frequency; $\tau_M = \varepsilon_0/en_e\mu_e$ is the Maxwellian time of neutralization of the volume charge; L is the characteristic size of the problem; j_e and j_i are the electron and ion current densities, respectively; $\boldsymbol{l}_E = \varepsilon_0 \boldsymbol{E}/en_e$ is the vectorized size of the electric field strength $\boldsymbol{E}$ variation; and l_u is the energy width of the electron path. Dots denote the terms which take into account the ion diffusion in (2). Usually, the ion diffusion and dynamic pressure can be neglected if it is assumed that $l_i/L \ll 1$, which we do. Taking account of the ion diffusion does not considerably influence the solution of the formulated problems; however, without it, the structure of the equations is simpler. Note that the vectorized characteristic size of the electric field strength variation is determined by the electron rather than the ion density [10]. Under certain conditions (in regions where the neutrality violation is essential), this inaccuracy results in analytical errors in the size of the Coulomb structure or its transition profiles of several orders of magnitude. The connection of l_E and the Debye radius r_D is quite simple: $l_E = r_D^2/l_u \gg r_D$. The potential drop along the length l_E considerably exceeds the potential drop determined by the electron temperature T_e on the length l_u [10, 11]. The formation of this long-range, as compared to the Debye radius, energy potential can determine the shaping of the plasma structures and their characteristic size [11].

The small dimensionless parameters of the proposed perturbation theory are the following ratios: l_i/L, l_u/L, l_E/L, $\Omega\tau_M$, μ_i/μ_e, j_i/j_e, and $\alpha_i \ll 1$, where α_i is the gas ionization degree ($\alpha_i \ll 10^{-6}$). It was shown in [10, 11] that, if the parameters $\Omega\tau_M$, $(\mu_k/\mu_J)l_E/L$, and l_u/L are small, the complete system of hydrodynamic equations and Poisson's equation can be solved using the perturbation theory analytically and numerically without the assumption of the plasma neutrality. Note that the smallness of the parameter $(\mu_k/\mu_J)l_E/L \ll 1$ can also be satisfied for $l_E/L \gg 10$, since $\mu_k/\mu_J \ll 1$. Therefore, in the framework of the perturbation theory, a region with considerable neutrality violation can be reached even in the zero order [10, 11]. Thus, the zero approximation is separated into two cases:

(1) drift, or quasi-neutral, when $l_E/L \ll 1$; and

(2) Poisson's, when $l_E/L \sim 1$ (or even $l_E/L \gg 1$) but $(\mu_k/\mu_J)l_E/L \ll 1$ (the main current is carried by electrons).

DRIFT FIELD IN THE ZERO APPROXIMATION

In the zero, or the so called drift approximation ($\rho = 0$ or $n_e = n_i = n$, $D_{i,\perp} = 0$), system of equations (1), (2) is reduced to the drift equation in which the electric field strength is related to the total current density j as

$$\boldsymbol{E}_0 = \boldsymbol{j}/e(n_e\mu_{0e} + n_i\mu_{0i}), \tag{3}$$

where the index 0 denotes that the mobilities are calculated under the conditions of satisfaction of the homogeneity and steady-state character of the electron and ion distribution functions. The electric field strength $\boldsymbol{E}_0$ can be called the drift field or the zero approximation field, unlike the diffusion or the Schottky field. $\boldsymbol{E}_0$ is determined not only by the current density but also by the electron and ion mobilities and densities. The field can be inhomogeneous in space, but the electron and ion distribution functions in the zero approximation are assumed to be homogeneous, independent of the parameter gradients, and steady-state.

In the zero approximation, the equation for the ions is reduced to the equation

$$\partial n/\partial t + \boldsymbol{j}\nabla(\mu_{0i}/\mu_{0e})/e = I_{i0} - R_{i0}. \tag{4}$$

The electron mobility is a nonlinear function of parameters (in particular, the parameter $\gamma = E/N$) and is determined by the mismatch of the processes of the electron production and loss, the oscillatory gas temperature T_v, n_e/N, and other parameters. Equation (3) in the zero approximation yields the connection of the electric field strength divergence and the electron density gradient,

$$\begin{aligned} \nabla \boldsymbol{E}_0 &= -(\boldsymbol{j}\nabla)\ln[\mu_{0J}n_e]\big|/(e\mu_{0J}n_e) \\ &= -\boldsymbol{E}_0\nabla\ln[\mu_{0J}n_e], \end{aligned} \tag{5}$$

where $\mu_{0J} = \mu_{0e} + \mu_{0i}$.

In the one-dimensional approximation with plane, cylindrical, and spherical symmetries, Eq. (4) can be represented in the form [2]

$$\partial n/\partial t + \boldsymbol{V}_a \partial n/\partial r + k\boldsymbol{V}_a n/r = I_{i0} - R_{i0}, \tag{6}$$

where $k = 0$, 1, and 2 for the plane, cylindrical, and spherical cases, respectively. The quantity V_a has the dimension of velocity and determines the profiles of the parameters of cumulative-dissipative structures in the gas-discharge plasma in the zero approximation. Therefore, the second term in (6) is called the ambipolar drift of neutral plasma, unlike ambipolar diffusion, which appears only in the next approximation with respect to the parameter l_u/L of the perturbation theory developed. Ambipolar drift in plasma appears in the presence of different dependences of the electron and ion mobilities on the parameter γ and can reach 70 m/s in nitrogen [2, 10]. The mobility of ambipolar drift in this approximation is determined by the mobility of the main ion. Ambipolar drift in plasma at increased pressures determines the profiles of parameters in discharges in the Faraday dark space. Ambipolar drift can arise also as a result of action on ions of, for example, the gravitational force along with electric forces or pumping neutral gas with the velocity $\boldsymbol{U}_r$, etc. If ions are frozen to the gas flow, the velocity of the plasma wind is equal to [10] $\boldsymbol{V}_a = \boldsymbol{U}_r + \mu_a \boldsymbol{E}_0$, where $\mu_a = \mu_i(\mu_i^* - \mu_e^*)/(1 + \mu_e^*)$ is the ambipolar mobility [10] and $\mu^* = \partial \ln\mu/\partial \ln\gamma$. Ambipolar drift (and, therefore, convective focusing) can be due to the inhomogeneity or non-steady-state character of the electron distribution function in ion sources and sinks (I_{i0} and R_{i0}), plasma-chemical reactions with participation of ions, neutrality violation in inhomogeneous non-steady-state plasma [10], gas pumping, an external magnetic field [2], etc. The quantity $\vec{\nabla}\vec{\boldsymbol{E}}$ can be expressed in terms of $\vec{\nabla} n_e$ only in the one-dimensional approximation with respect to x [10, 11] or r [2].

ANALYTICAL AND NUMERICAL MODELS

The steady-state quasi-neutral profile in region II in the approximation of the reaction–drift ambipolar transfer is described by the differential equation following from (6):

$$d(Br^k n_e\gamma)/dr = -r^k n_e(\nu - \beta), \qquad (7)$$

where $k = 0$, 1, and 2 for the plane, cylindrical, and spherical cases, respectively. In this case, the reaction in (7) is taken into account in the following form:

(1) electron impact ionization with the frequency ν;

(2) loss of plasma is taken into account by the loss frequency β, and, at low ion pressures and densities, it is determined by ambipolar diffusion.

Equation (7) allows one to calculate the coefficient of quasi-neutral cumulation as a function of the radius r and the following parameters:

(1) the electron (and ion) density;

(2) the reduced electric field strength.

Note that, for $\gamma(r) > 40$, the effective plasma loss frequency in the region of developed cumulation is small as compared to the ionization frequency. If the electron and ion drift velocities are represented in the form $\mu_e E = C\gamma^\alpha$ and $\mu_i E = B\gamma$ (where C = const and B = const), the profile of the reduced electric field $\gamma(r)$ in the quasi-neutral approximation can be obtained analytically from (7):

$$\gamma(r) = -\ln[\exp(-A\gamma(0)) + A\nu_0(r - r_0)/B(1 - \alpha)]/A. \qquad (8)$$

It is seen from (8) that, for $r_1 = r_0 - B(1 - \alpha)/A\nu_0\exp(A\gamma(0))$, the value of $\gamma(r_1) = \infty$. The size of the transition region $r_\nu = B(1 - \alpha)/A\nu_0\exp(A\gamma(0))$ from $\gamma(0)$ to $\gamma(r_1) = \infty$ is determined by the ion mobility (the parameter B), the factor of the nonlinearity of the electron and ion drift flows with respect to each other $(1 - \alpha)$, the parameter of the dependence of the frequency of the direct ionization on the electric field strength (A), and the value of the ionization frequency $\nu_0\exp(A\gamma(0))$ at r_0.

Therefore, if the cumulation region is determined by the nonlinear process "ambipolar drift-ionization," the minimal dimensions of this region on the dust particle should vary according to these parameters. The coefficient of cumulation of the plasma density λ_n is determined according to Eq. (8):

$$\lambda_n = n_e/n_e(0) = 1/(\ln[\exp(-A\gamma(0)) + A\nu_0(r - r_0)/B(1 - \alpha)])^\alpha r^k. \qquad (9)$$

It follows from the condition of the electron current conservation (in the approximation $j_i/j_e \ll 1$).

For $\alpha = 1$, the ambipolar drift becomes equal to zero and the cumulation profiles of the order parameters vanish. In this case, other transfer processes should be taken into account for the description of the cumulative profiles.

According to (8), the cumulation of the reduced field ($\lambda_\gamma = \gamma/\gamma(0)$) is independent of the type of symmetry or geometry of the Coulomb plasma focusing the charged particle of the lens. Figure 2 shows the profile of the cumulation coefficient of the reduced electric field λ_γ qualitatively reflecting dependence (8). According to (9), the cumulation of the gas density or ionization degree is essentially determined by the type of symmetry and depends on the value of k (Fig. 3). For all three one-dimensional cases in this work, the same profile of the reduced electric field was analytically obtained; this profile is close to linear (in space) at the boundary of the cathode layer. Thus, relation (8) substantiates the assumption in the Engel–Steenbeck model concerning the linear character of the profile of the reduced electric field strength E/N in the region of its cumulation near the cathode (Fig. 2).

Model (7) is applicable for description of inhomogeneous profiles of parameters of the dynamic order of the discharge and current collapse within $10^{-2} < \gamma < 200$; it covers the wide spectrum of nonlinear dynamic

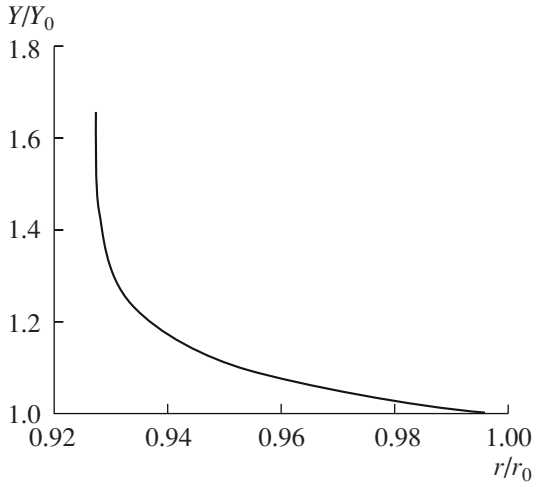

Fig. 2. The electric field strength $E/E_0 = \gamma/\gamma_0$ as a function of r/r_0 in the approximation of ambipolar drift ionization. For $k = 0$, 1, and 2, the profiles coincide.

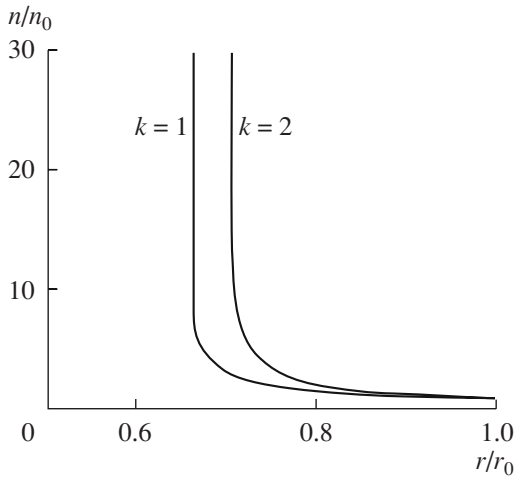

Fig. 3. Reduced electron density as a function of r/r_0 in the approximation of ambipolar drift ionization for different k.

phenomena, including electric field cumulation in gas-discharge nonequilibrium plasma. The presence of processes of ambipolar diffusion and diffusion due to neutrality violation does not eliminate the electric field cumulation [4], but the length of the cumulation region changes accordingly.

ESTIMATION OF CUMULATIVE-REACTIVE EFFECTS

Cumulative-reactive drag can be calculated from (8), (9). Taking into account the thermophoresis processes, the numerical solution of this system is a separate complex problem. Let us estimate this drag under the assumption that the main current is attracted to the cumulative-reactive jet according to the schematic diagram in Fig. 1. In the case of spherical symmetry ($k = 2$), the ratio of the interparticle distance R and the characteristic size of the dust particle r squared is the coefficient of simple cumulation of the ion current $\lambda = (R/r)^2$. The momentum transferred to the dust particle by the ion flow is proportional to the spot area, the ion velocity, and the ion current density j_i

$$P_1 \sim 4\pi R^2 j_i(R)/e. \quad (10)$$

If, in the cumulation region, the ion current is increased due to ionization and the relative role of the electron current is decreased due to the decrease in their density, as in the usual near-cathode layer, the drag P_1 can be increased by a factor of ξ, where ξ is the coefficient of ionization amplification. This amplification of the ion current in the structure with limited electric field cumulation near the dust particle can take place if the parameter E/N reaches breakdown values. Note that the parameter ξ is the analogue of the inverse quantity of the second Townsand coefficient, $\gamma_2 \sim 10^{-2}$. This gives grounds to assume that ξ can be on the order of $1/\gamma_2 \sim 10^{-2}$

$$P_2 \sim 4\pi\xi R^2 j_i(R)/e. \quad (11)$$

Simultaneous ion current and electric field cumulation near the dust particle results in the heating of its surface and the gas from the side of the electric field cumulation and the formation of great asymmetric thermophoresis forces. If there are no processes violating the cumulation, according to the explosion solutions to Eqs. (8), (9) bounded by the size of the dust particle only, the power of the heat release to one of the sides of the dust particle can be estimated. Let the heating take place as a result of direct collisions of ions with gas particles; then, the power of the heating of the gas volume element is

$$Q(R) = E(R) j_i(R). \quad (12)$$

The electric field $E(R)$ near the particle surface is increased weakly according to Eq. (8), and $Q(R)$ is increased toward the particle as $\sim 1/R^2$. As a result of cumulation, the power of the asymmetric heat release on the particle with the radius r can reach

$$Q(r) = Q(R)\lambda\xi = \chi Q(R). \quad (13)$$

If the ratio of the interparticle distance and the size of the particle $R/r = 200$ or 20, $\lambda = 40000$ or 400. If $\xi \sim 10^2$, the coefficient of heat release cumulation $\chi = \lambda\xi \approx 4 \times 10^6$ or 4×10^4.

It is seen from the estimates that the gas heating in the region of formation of cumulation and ionization enhancement on the surface of the dust particle can exceed many times the heating in the homogeneous background plasma. The thermophoresis forces arising as a result of the temperature gradient may result in the motion of the particle with high velocity.

The second important mechanism determining the motion of the dust particle is the momentum transfer to the particle by the ion flow in collisions. This phenom-

enon is known as ion drag [1] in literature devoted to investigation of dusty plasma. At development of cumulative processes according to our model, it is possible that the ion flow to the particle with asymmetric cumulation on its surface is multiply enhanced (by a factor of χ), which provides additional force in the region of cumulation. It is clear that, in the presence of ion enhancement, convective processes of cumulation of electric force and energy–mass flows are limited by the size of the particle and are destroyed by oscillations of dust particles. However, this is a separate problem.

CONCLUSIONS

Processes of asymmetric ionization and cumulation of an electric field and electron and ion flows can develop and be enhanced near the surface of charged dusty particles in plasma.

In the region of cumulation, when the parameter *E*/*N* reaches breakdown values, the ion current can be increased (multiply) due to ionization. The coefficients of ionization–cumulation enhancement can reach values on the order of 10^6. Due to self-developed processes of asymmetric cumulation of the flow of positive ions asymmetry in the heating of the surface of the dust particle, momentum transfer to it from positive ions arises; as a result, the negatively charged dust particle moves in the plasma with high velocity.

REFERENCES

1. Fortov, V.E., Khrapak, A.G., Khrapak, S.A., et al., "Dusty Plasma", *Usp. Fiz. Nauk*, 2004, vol. 174, no. 5, pp. 495–544.
2. Vysikailo, F.I., Electric Field Cumulation in Dissipative Structures of Gas–Discharge Plasmas, *JEPT*, 2004, vol. 98, no. 5, pp. 936–945.
3. Vasilyak, L.M., Vetchinin, S.P., Obvival'neva, A.A., et al., Parametric Excitation and Stabilization of Dusty Structures in Glowing Discharge with External Periodic Nanosecond Electric Field, *J. Tech. Phys. Lett.*, 2007, vol. 33, no. 2, pp. 135–140.
4. Kesaev, I.G., *Katodnye Protsessy Elektricheskoi Dugi* (Cathode Processes of Electric Arc) (Moscow, Nauka, 1968) [in Russian].
5. Aburdzhania, G.D., *Samoorganizatsiya Nelineinykh Vikhrevykh Struktur i Vikhrevoi Turbulentnosti v Dispergiruyushchikh Sredakh* (Self-Organization of Nonlinear Vortex Structures and Vortex Turbulence in Dispersive Media) (Moscow, KomKniga, 2006).
6. Zababakhin, E.I. and Zababakhin, I.E., *Yavleniya Neogranichennoi Kumulyatsii* (Unlimited Cumulation Phenomena) (Moscow, Nauka, 1988) [in Russian].
7. Rabinovich, M.I., Ezerskii, A.B., *Dinamicheskaya Teoriya Formoobrazovaniya* (Dynamic Shaping Theory) (Moscow, Yanus-K, 1998) [in Russian].
8. Samsonov, D., Goree, J., Ma, Z.W., et al., Mach Cones in a Coulomb Lattice and a Dusty Plasma, *Phys. Rev. Lett*., 1999, vol. 83, no. 18, pp. 3649–3652.
9. Schweigert, V.A., Schweigert, I.V., Nosenko, V., et al., Acceleration and Orbits of Charged Particles Beneath a Monolayer Plasma Crystal, *Phys. Plasmas*, 2002, vol. 9, no. 11, pp. 4465–4472.
10. Vysikailo, F.I., Jumps of Parameters of Inhomogeneous Collisional Plasma with a Current due to Quasineutrality Violation, *Plasma Phys. Rep.*, 1985, vol. 11, no. 10, pp. 1256–1261.
11. Vysikailo, F.I., On Drift Processes in Gas Discharge Plasma, *Plasma Phys. Rep.*, 1990, vol. 16, no. 10, pp. 1268–1270.

ISSN 1068-3755, Surface Engineering and Applied Electrochemistry, 2008, Vol. 44, No. 5, pp. 383–389. © Allerton Press, Inc., 2008.
Original Russian Text © A.I. Mikhailyuk, R.P. Zhitaru, 2008, published in Elektronnaya Obrabotka Materialov, 2008, No. 5, pp. 49–56.

ELECTRICAL PROCESSES IN ENGINEERING AND CHEMISTRY

Features of Plastic Deformation of Electrospark Coatings and Ways for Improvement of Their Strength Characteristics at Friction

A. I. Mikhailyuk and R. P. Zhitaru

Institute of Applied Physics, Academy of Sciences of Moldova, ul. Academiei 5, Chisinau, MD-2028 Republic of Moldova
E-mail: raisa@phys.asm.md

Received March 18, 2008

Abstract—Analysis of the structural state of surface metal layers after their electrospark doping (ESD) and subsequent surface plastic deformation (SPD) has been performed. The structure levels and their scale ranging within 20–10^3 nm have been determined. Applying the methods of X-ray structure analysis and electron microscopy, it has been found that the linear defect density after ESD and after ESD + SPD is practically identical; this allowed suggesting that the basis for the mechanism of plastic deformation of electrospark coatings is collective motion of dislocations, that is, rotational processes. Some ways of formation of stable and more homogeneous structures of electrospark coatings with required properties have been analyzed and proposed.

DOI: 10.3103/S1068375508050086

A promising way for the improvement of the bearing capacity of construction materials is to strengthen their surface layers or to deposit strengthening coatings. This allows improvement of the surface strength and wear resistance; as a consequence, the operational lifetime of the construction and tool materials increases. Electrospark doping well fits the requirements of this direction; it is a promising technique for modification of surface layers of construction materials.

One of the principal characteristics of the electrospark doping method (ESD) is the powerful thermoplastic deformation of the formed layer on the treated material surface, leading to its significant strengthening. This is caused by the transient pulse electric discharge between the electrode and the piece ($t \sim 10^{-4}$–10^{-5} s) [1]; as a result, a micromelt with a weight of ~0.05–0.1 mg is formed on the cathode–piece [2]; due to the high heat conductivity of the piece material and its relatively great weight, the micromelt is cooled from the temperature of the liquid (boiling) state to 0.05 T_m and below with a rate of ~10^4°C/s [3]. These conditions of treatment result in thermoplastic deformation with the formation of a high density of linear defects in the formed layer; in some cases, it achieves a value of 10^{11}–10^{12} cm^{-2} [4–5]. At this dislocation density and with the temperature–time specific character of the plastic deformation in the process of ESD, conditions for proceeding of the processes of dislocation polygonization and three-dimensional cellular substructure formation are established. However, in a number of cases, after ESD, another type of dislocation substructure is formed too. In this regard, the exact dependence of the substructure type on the ESD modes has not been found yet.

Therefore, the aim of the present paper is to specify the parameters of the surface layer substructure appearing in the process of ESD, its specific character, and the mechanism of plastic deformation of these layers, as well as to select ways for improvement of electrospark equipment allowing a stable mode of formation of the required properties. Estimation of the parameters of the electrospark coating substructure and its form were studied both by X-ray structure analysis and transmission electron microscopy while applying the thin foil preparation method [6]. X18H9T austenitic steel was selected for the studies; it is characterized by sufficiently high viscosity contributing to obtaining of electrospark thin steel layers with the thickness optimum for transmission electron microscopy observations. The absence of phase transformations in the process of hardening of the X18H9T steel liquid phase makes it possible to obtain a picture of the dislocation structure formation exclusively due to the thermoplastic deformation induced by ESD. The research techniques are described in detail in papers [5, 16, 18].

The studies carried out by us in paper [5] have shown that, as a result of thermoplastic deformation appearing in the process of ESD, a cellular substructure is formed; its walls consist of screw dislocations of different signs; that is, it is a multipole formation of dislocations characterized by low energy and significant resistance to deformation [7–9]. Formation of the substructure in the process of ESD is accompanied by certain surface strengthening. The observed deformation strengthening of the initial structure-inhomogeneous system of the metal is apparently caused by the following effects: at first, large local elastic deformations

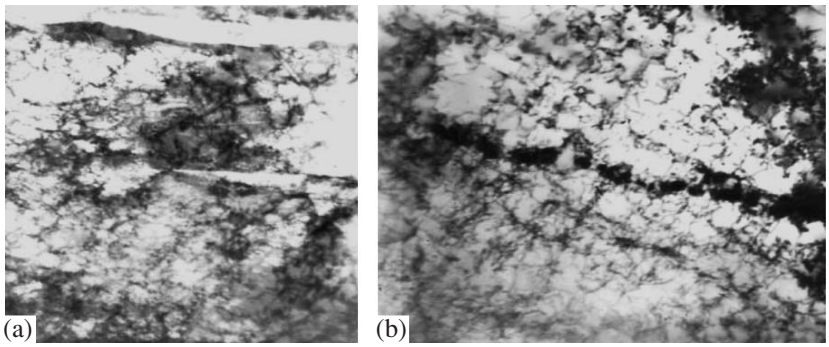

Fig. 1. Dislocation structure of the steel surface layer after treatment by ESD. Magnification: (a) 33500; (b) 15700.

appear; the dislocation density (ρ) increases; the conditions for dislocation alignment in the walls are established, which subsequently is transformed into boundaries of fragments and cells, and a cellular substructure is formed (Fig. 1).

According to the obtained data of the X-ray structure analysis and electron microscopy, the dimensional parameters that characterize the cellular substructure of the coating formed in the process of ESD range within 20–200 nm. Similar parameters of the microstructure were also obtained in paper [28] in the course of studying the microstructure of copper foil subjected to the action of electrospark discharges. These parameters of the microstructure correspond to the mesolevel in the structure level hierarchy [7].

Detailed metallographic analysis of layers of Armco iron and various steels subjected to electrospark treatment has shown that, at certain so-called mild treatment modes ($W_n \approx 0.4$–0.9 J), the size of the grain of the multiphase white layer ranges within 0.1–10 μm [10, 11]. The presented values are comparable with the cellular substructure parameters mentioned above. This allows concluding that, in some ESD modes, there is formed a substructure with the boundaries of its grains being areas limited by a dislocation network. Thus, in the process of electrospark treatment, in the surface metal layers, nanodimensional structures and substructures are formed; they are characterized by entirely new physicomechanical properties under various impacts [12, 13].

Thus, one of the efficient directions of ESD application in engineering is formation of friction surfaces. Appreciable improvement of wear resistance of the surfaces obtained by this method is shown in a number of papers [14]. Extensive research of the interrelation of the parameters of the substructure of friction surfaces of various metals strengthened by the ESD method and their wear resistance have revealed a certain correlation between the size of the mosaic blocks and the degree of wear of iron, copper, and titanium surfaces (representatives of BCC, FCC, and FCCP crystal lattices, respectively) [5]. In the tests under conditions of sliding friction, the highest wear resistance was found for the coatings characterized by the finest substructure, where the size of the mosaic blocks was 17 nm for iron, 130 nm for copper, and 20 nm for titanium [5]. The obtained results confirm the concept of strengthened surface formation not due to strong blocking of dislocations but due to the creation of obstacles to their long displacements with the possibility of their short displacements in the case of peak voltage appearance [15].

Table 1. Values of the theoretical strength and yield point strength

Sample type	τ_{theor}, MN/m^2	σ, MN/m^2	σ/τ_{theor}, %
Titanium	4.0×10^2	3.2×10^2	80
Iron	8.2×10^2	6×10^2	70
Copper	2.4×10^3	1.3×10^2	50

On the basis of the data of the X-ray structural analysis of the layers formed by electrospark treatment, the degree of strengthening of the crystal lattice was estimated; it was determined by comparison of the value of the strengthened structure yield point calculated by formula (1) and the value of the theoretical shear strength of the metals ($\tau_{theor} = G \times 10^{-2}$ for BCC and FCCP metals and $\tau_{theor} = G \times 0.66$ for FCC metals) [5] (Table 1):

$$\sigma = \alpha G b \sqrt{\rho}, \quad (1)$$

where α is the proportionality factor equal to 1, G is the shear modulus, b is the Burgers vector, and ρ is the dislocation density.

As one can see from Table 1, the values of the stresses of the yield point σ are lower than the stresses of the theoretical strength τ_{theor}, but, in magnitude, they constitute the major part of the strength limit. In addition, the higher the initial hardness of the studied metal, the closer the stresses of the yield point to the stresses of the strength: for copper, this relation is only 50%, while for titanium it is 80%. This testifies to the fact that the degree of strengthening of iron and titanium in the process of ESD approaches the critical value, while copper preserves a sufficiently great plasticity margin. Nevertheless, in both cases, the strengthening is significant; apparently, it cannot be achieved exclusively due

Table 2. Stresses of the I kind in surface layers of the samples treated by ESD and ESD + SPD

No.	Sample material	Electrode material	Running load at SPD, kgf	ESD	ESD + SPD
1	Steel 45	Steel 45	40	150	–770
2	″	″	80	150	–840
3	″	″	120	150	–910
4	Steel 40X	Steel 45	40	240	–630
5	″	″	80	240	–770
6	″	″	120	240	–980
7	VT-1	VT-1	–	980	–
8	VT-1	VT-1	40	980	780
9	VT-1	VT-1	80	980	590
10	VT-1	VT-1	120	980	200
11	VT-1	VT-1	150	980	–210

Table 3. Roughness at ESD + SPD at $P = 80$ kgf

Sample material	Electrode material	Initial hardness of sample HRC	R_α, μm		R_z, μm		R_{max}, μm		K
			ESD	ESD + SPD	ESD	ESD + SPD	ESD	ESD + SPD	
Steel 45	Steel 45	7–8	4.94	2.31	20.2	3.6	35.0	5	5.6
Steel 40X	Steel 45	38–40	4.63	2.41	8.94	4.56	14.0	6	1.96

Note: Here, $K = R_{ESD}/R_{ESD + SPD}$.

to retardation of long runs of dislocations. More complex behavior of dislocations (formation of piling up of dislocations, boundaries of cells, fragments, etc., and formation of barriers to the translational mode) is also critical [16].

However, in addition to the high degree of strengthening of the surfaces formed by the ESD method, they are also characterized by raised roughness ($R_z \approx 15$–30 μm) and a sufficiently high level of residual tensile stresses; in some cases, this impedes their application as friction surfaces. One of the methods for removal of these disadvantages is the method of surface plastic deformation (SPD) [17]. First of all, it was necessary to find how this treatment will affect the strength properties of a surface layer formed in the process of ESD, since it is known that these surfaces already possess a very fine structure with high dislocation density and are characterized by rather high hardness [14]. In order to elucidate this question, studies were carried out [16, 18] where the features of the structure formation in the formed layer at SPD of electrospark coatings and the character of the plastic yielding were found.

SPD was put into effect by means of a running facility; the deforming tool in it was a ball. Rollers of steels (st. 45, st. 40X, st. X18H9T) and titanium alloy (VT-1) were applied as samples. Electrodes were prepared of st. 45, st. X18H9T, and VT-1. The studies were carried out by virtue of optic and electron microscopy (scanning and transmission) and by the methods of X-ray structure analysis, strip chart recording, and microhardness measurement. As a result, SPD modes resulting in the formation of compression microstresses in the surface layer were determined (Table 2). Therein, the fatigue strength increases with the surface roughness being most favorable for friction conditions (Table 3).

One can see from Table 2 that, after ESD, significant tensile stresses appear in the surface layer. However, even at small efforts, the action of SPD led to sign inversion in the stresses—compression stresses appeared instead of tensile ones. In the case of the titanium alloy, such a sign inversion of stresses took place only at a load on the ball of 150 kgf. This effect is apparently related to the high initial value of the tensile macrostresses appearing in the titanium samples after ESD and to the low value of the stacking fault (10 mJ/m^2). For the iron, the stacking fault is 140 mJ/m^2; this explains its higher plastic properties as compared with the titanium.

The most interesting results were obtained when studying the evolution of the substructure of the deformed electrospark coatings. The substructure state was determined according to the degree of defect presence on the surface layer, which was estimated by the variation in the intrinsic broadening β along line (211)

Table 4. Intrinsic broadening of lines (211) α–Fe and (10.3) Ti after ESD and ESD + SPD

No.	Sample material	Load at SPD, kgf	By the Bragg–Brentano pattern, deg		By the slipping beam pattern, deg	
			ESD	ESD + SPD	ESD	ESD + SPD
1	St. 45	40	114 ± 0.04	1.09 ± 0.04	1.36 ± 0.06	1.58 ± 0.05
2	″	80	1.13 ± 0.05	1.11 ± 0.04	1.36 ± 0.06	1.43 ± 0.06
3	″	120	1.16 ± 0.06	1.16 ± 0.05	1.30 ± 0.05	1.42 ± 0.05
4	St. 45	40	1.42 ± 0.06	1.38 ± 0.06	1.39 ± 0.05	1.55 ± 0.05
5	″	80	1.43 ± 0.06	1.38 ± 0.06	1.38 ± 0.06	1.55 ± 0.06
6	″	120	1.38 ± 0.06	1.47 ± 0.05	140 ± 0.07	1.51 ± 0.05
7	VT-1	–	1.36 ± 0.06	–	1.38 ± 0.07	–
8	″	40	″	1.29 ± 0.05	″	1.33 ± 0.05
9	″	80	″	1.34 ± 0.06	″	1.28 ± 0.05
10	″	120	″	1.39 ± 0.06	″	1.41 ± 0.05
11	″	150	″	1.40 ± 0.06	″	1.42 ± 0.05

for α-iron and (10.3) for titanium. Herein, the intrinsic broadening was determined by the approximation method using the functions $f(x) = (1 + x^2)^{-2}$ and $g(x) = (1 + x^2)^{-1}$.

Two modes of X-ray photography were applied: the ordinary one with Bragg–Brentano focusing and photography by the method of a sliding beam for layers of low thickness [19]. The photography was carried out using Co-K_α-radiation along line (211) for α-iron and using Cu-K_α-radiation for titanium. The thickness of the analyzed layers using the ordinary photography was ≈12 μm for Fe and ≈7 μm for Ti; at photography by the sliding beam method, it was ~6 and ~5 μm, respectively. For determination of the intrinsic broadenings, vacuum-annealed samples of st. 45 and titanium alloy VT-1 were used as the reference standards. Photography of the reference standards allowed taking into account the sample geometry and surface roughness in the calculation of the intrinsic broadening (Table 4). Analysis of the data of Table 4 shows that, in the layer of ~12 μm, the values of β_{211} after ESD and the integrated action of ESP + SPD coincide within the experimental error. In the thinner near-surface layer (~6 μm), a certain increase in β_{211} after SPD is observed; this testifies to the insignificant strengthening of this layer. In the titanium alloy VT-1, differences in the intrinsic broadening $\beta_{10.3}$ were not observed either in the layer of 7 μm or in the layer of 5 μm; this confirms the previously obtained data on the critical degree of titanium layer strengthening after ESD.

Table 5. Microhardness of the metal surfaces after treatment by ESD and ESD + SPD

No.	Sample material	SPD load, kgf	H, GPa	
			ESD	ESD + SPD
1	St. 45	40	7.3 ± 1.0	6.9 ± 1.2
2	″	80	6.9 ± 1.0	6.9 ± 0.9
3	″	120	7.6 ± 1.0	8.0 ± 0.8
4	St. 40X	40	10.6 ± 2.2	10.6 ± 3.0
5	″	80	11.3 ± 1.8	10.6 ± 1.7
6	″	120	12.0 ± 1.8	11.3 ± 2.8

The character of the formation of the strength properties of the surface layers of the studied metals after ESD and ESD + SPD is also confirmed by the microhardness measurements, which were carried out by means of a PMT-3 device at an indentation load of 100 gf (Table 5). One can see from Table 5 that the additional action of SPD practically does not change the hardness of the layer formed after ESD; this correlates with the above given data of the X-ray structure analysis. Thus, it is shown that the degree of strengthening of the surface layer of the studied materials after application of ESD and subsequent action of SPD is approximately identical.

Electron microscope studies of the evolution of the structure of electrospark coatings after SPD have shown (Fig. 2) that, as a result of cold deformation, further transformation of the dislocation substructure took place. The action of SPD begins from the deformation level when the cellular substructure is formed. Already at this stage, the mechanical field in the deformed material contains two interdependent components—translational and rotational ones. The disorientation between the cells is still low (on the order of 1^0) (Fig. 1).

The subsequent action of SPD continues the evolution in the material structure. The cellular structure presented in Fig. 2b fills the whole surface of the treated sample. One can see that the boundaries of many cells are smeared-out, noncompact, and discontinuous in the majority of cases. This implies that grain-boundary slipping is developed and that rotation type processes are present; migration of boundaries and even material

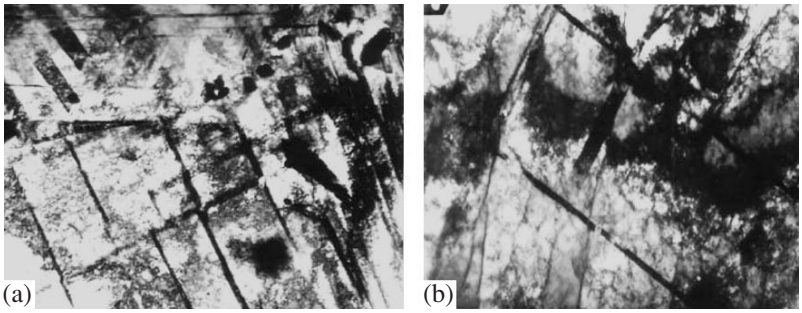

Fig. 2. Dislocation structure of the steel surface layer after treatment by ESD and subsequent SPD. Magnification: (a) 11000; (b) 23000.

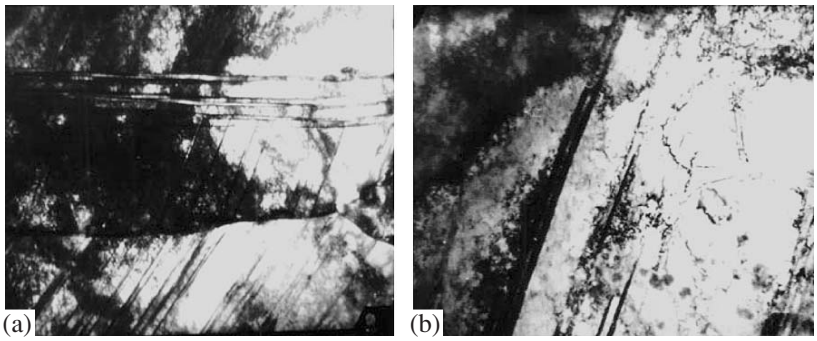

Fig. 3. Dislocation substructure of the steel surface layer after treatment by ESD and SPD. Magnification: (a) 11000; (b) 23000.

extrusion in some regions are observed. The size of the cells practically does not change with increasing deformation. At further action of SPD, the mentioned processes intensify and bend contours appear near boundaries of fragments. As a rule, their appearance is accompanied by the development of a disoriented band structure (Fig. 2b).

In addition, bands of deformation localized in the near-boundary zone are formed, in which the structure cell extrusion takes place; the material state becomes strongly stressed (Fig. 3). Processes of accommodation (relaxation) character originate [20, 21]. For relieving of the critically stressed material, its fragmentation occurs; the rate of the grain–boundary slipping, as well as the extrusion of the near-boundary bands on the whole, increases [22]. The cellular band dislocation substructure transits into the disoriented band cellular-reticular one (Fig. 3) according to the classification proposed in paper [7]. Analyzing the scale levels of the cellular and band substructures, one can note that they are in one diapason of the hierarchy of the structure levels with the scale of the substructure parameters within 10–10^3 nm.

This character of formation of the dislocation substructure testifies to its self-organization. The factor of the process of the dislocation substructure reconstruction at SPD, most probably, tends to the relative minimum of the total energy of the dislocation subsystem [23, 24]. The observed constancy of the density of the linear defects after SPD of electrospark coatings testifies that the principal mechanism of plastic deformation is grain-boundary slipping that leads to mutual rotation of micro-objects. The latter is one of the collective effects in systems of dislocations: the collective motion of dislocations consisting of dividing of ρ into $\Delta\rho_+$ and $\Delta\rho_-$, resulting in transition from the dislocational to rotational modes of deformation, that is, to the rotational mechanism of deformation [24, 25].

Consequently, the electron microscope studies have shown that the dislocation structure of electrospark coatings is transformed in the process of SPD. However, the scalar dislocation density and microhardness value before and after the SPD practically did not change. It is found that the deformation levels of the dislocation structure after ESD and SPD correspond to the deformation stages when rotational processes prevailing in them contribute to the intensification of the processes of dislocation polarization and to a decrease in the coefficient of deformation strengthening of the substructure [7]; this improves the plastic character of the deformation of the material and its lifetime. Apparently, these processes are responsible for the identity of the microhardness and the scalar dislocation density before and after SPD.

Thus, it is found that, in the process of ESD of metals, a coating with a high degree of deformation strengthening is formed; the dislocation structure is a

cellular substructure with minimum cell sizes. Subsequent tribological deformation of the coatings occurs not due to translational motion of dislocations with variation in their density and dispersion of the cellular substructure but mainly by virtue of rotational mechanisms. Turning of fragments and nanograins, as well as the appearance of mesoscopic shears developing along boundaries of the fragments, is, apparently, a real mechanism of deformation of electrospark coatings. However, formation of a concrete substructure is only possible in certain modes of ESD. Finding the conditions of ESD for formation of a fine cellular substructure is a problem of further studies.

It is known that the properties of the surface layer obtained at ESD depend on the value of the discharge gap, *ceteris paribus*. Since, in the electrospark process, the distance between the vibrating electrode and the piece surface continuously varies within certain limits and the electrode moves above the piece surface with possible pulse actions of already treated sections, it should be expected that, in one treatment cycle, there will be formed coatings with different physicochemical characteristics and substructure differing from the ordered one (of the cellular type and similar) (Fig. 3).

The studies carried out in paper [26] have shown that, after ESD, the treated surface is characterized mainly by three types of microtopography corresponding to the plasma, drop, and contact mechanisms of electrode material transfer on the piece. Herein, it was found that a cellular substructure is only formed in the plasma transfer zone (sometimes in the zone of drop transfer) and it is never revealed in the contact transfer zone.

The analysis of the factors influencing the formation of a certain transfer mechanism has shown that the relation of zones of plasma, drop, and contact microtopography depends on the open-circuit voltage, the short-circuit current, the reserve capacity (pulse duration), the material of the piece and the cathode, and on other factors. Thus, an increase in the open-circuit voltage, *ceteris paribus*, increases the plasma transfer zone area. The degree of coating strengthening is appreciably affected by the pulse duration at ESD, which must be sufficient for the complete proceeding of phase transformations, such as steel austenization at heating, formation of a fine cellular substructure, etc.

Since the phenomenon of austenization is related to the transformation temperature, the probability of the complete proceeding of the phase transformations at various depths was estimated on the basis of the solution of the heat conductivity equation:

$$\partial T(x,\tau)/d\tau = \alpha\partial^2 T(x,\tau)/dx^2 \quad (\tau > 0;\ 0 < X < \infty), \tag{1}$$

where x is the distance from the surface, and α is the heat conductivity coefficient. The solution of this equation has the form

$$T(x,\tau) = 2q_c/\lambda\sqrt{\alpha\tau}\,\mathrm{ierfc}(x/\sqrt{\alpha\tau}), \tag{2}$$

where q_c is the energy flux on the surface of the half-space, and λ is the heat conductivity coefficient. The time of the isothermal transformation and austenite formation is determined from the following expression [27]:

$$\tau(T_i) = \tau_o \exp(Q/RT_i), \tag{3}$$

where $\tau(T_i)$ is the time of complete transformation, T_i is the transformation temperature, τ_o is the preexponential factor (1.89×10^{-9} C), Q is the activation energy (218 kJ/mol), and R is the universal gas constant. The solutions of equations (2)–(3) determine the criterion of complete austenization:

$$K = \int_{\tau i} d\tau/\tau_o \exp(Q/RV_{av}\tau), \tag{4}$$

where $\tau_i = T_o/V_{av}$ is the time of achievement of the transformation beginning temperature, and V_{av} is the average rate of heating. At $K > 1$, this expression is a criterion of the complete austenization in the surface layer with the thickness h under the action of the external energy flux q with the duration τ_u. The results of the calculations have shown that, according to the criterion, the austenitic-martensitic strengthening action of the pulse discharge of ESD may be achieved in a pulse duration range of 100–600 μs. However, the pulse duration influence on the formation of the optimum substructure for various types of lattices and materials has not been studied yet. Therefore, it appears to be efficient to continue studies in this field with the view to reveal ESD modes allowing the formation of a substructure of materials with high wear resistance properties.

CONCLUSIONS

As a result of the carried out studies, it was found that, within the limits of certain modes of treatment, the scale substructure parameters formed by the method of ESD of the surface layer range within nanometer values (17–130 nm). SPD of electrospark coatings leads to sign inversion in their microstresses, transforming tensile stresses into compression ones. The scalar dislocation density and the microhardness practically do not change. The plastic deformation in the studied modes of SPD of electrospark coatings is determined mainly by the rotational mode, that is, the rotational motion of fragments, thus preserving the plastic character of the deformation and extending the lifetime of the material.

ACKNOWLEDGMENTS

We thank A.E. Gitlevich for participation in discussions of the subject of the paper.

REFERENCES

1. Lazarenko, N.I., Variation in Initial Properties of the Cathode Surface under Action of Spark Pulses Proceeding in a Gaseous Medium, in *Elektroiskrovaya obrabo-*

tka metallov (Electrospark Treatment of Metals), Moscow: Akad. Nauk SSSR, 1957, issue 1, pp. 70–94.

2. Zolotykh, B.N. and Kruglov, A.I., Heat Processes on Electrode Surface at Electrospark Treatment of Metals, *Problemy elektricheskoi obrabotki materialov* (Problems of Electric Treatment of Materials), Moscow: Akad. Nauk SSSR, 1960, issue 1, pp. 65–76.
3. Zolotykh, B.N., Kruglov, A.I., Gioev, K.Kh. et al., *Issledovanie fizicheskikh zakonomernostei elektricheskoi erozii metallov v zhidkoi dieleketricheskoi srede. Tekhn. otchet TsNIL* (Study of Physical Laws of Electric Erosion of Metals in Liquid Dielectric Medium. Tekhn. Report TsNIL), Elektrom. Akad. Nauk SSSR, 1957.
4. Lukichev, B.N. et al., Improvement of Efficiency of Surface Strengthening at Electrospark Doping of Machine Pieces, *Electron. Obrab. Mater.*, 1987, no. 4, pp. 22–25.
5. Mikhailyuk, A.I., Influence of Electrospark Doping of Metal Surfaces on their Wear Resistance, *Extended Abstract of Cand. Sci. (Eng.) Dissertation*, Institute of Instrument Engineering, Moscow, 1990.
6. Gorelik, S.S., Rastorguev, L.N., and Skakov, E.A., *Rentgenograficheskii i elektronno–opticheskii analiz* (X-ray and Electron–Optic Analysis), Moscow: Metallurgiya, 1970.
7. Panin, V.E., Grinyaev, Yu.V., Danilov, V.I. et al., *Strukturnye urovni plasticheskoi deformatsii i razrusheniya* (Structure Levels of Plastic Deformation and Failure), Novosibirsk: Nauka, 1990.
8. Ignatenko, L.N., Kasatkina, N.F., Sharkeev, Yu.P. et al., *Formirovanie i razvitie s deformatsiei tonkoi struktury srednelegirovannoi konstruktsionnoi stali* (Formation and Development with Deformation of Thin Medium-Alloy Construction Steel), Tomsk: Izd. Tomskogo Univ., 1986, pp. 164–172.
9. Ivanov, Yu.F., Gladyshev, S.A., and Kozlov, E.V., Structure Estimations of Yield Point of High-Resistance Construction Steel, in *Plasticheskaya deformatsiya splavov* (Plastic Deformation of Alloys), Tomsk: Izd. Tomskogo Univ., 1986, pp. 152–163.
10. Palatnik, L.S., Transformation in the Surface layer of Metals under Action of Electric Discharges, *Izv. Akad. Nauk SSSR, Ser. Fiz.*, 1951, vol. 15, no. 4, p. 467.
11. Mogilevskii, I.Z. and Chepovaya, S.A., Metallographic Study of Steel Surface Layer after Electrospark Treatment of Metals, in *Elektroiskrovaya obrabotka metallov* (Electrospark Treatment of Metals), Moscow: Akad. Nauk SSSR, issue 1, pp. 95–116.
12. Volkov, G.M., On Critical Parameters of Nanotechnology, *Nanotekhnika*, 2006, no. 1, pp. 3–9.
13. Polyakov, S.A. and Khazov, S.P., Nanotechnique in Tribology, *Nanotekhnika*, 2006, no. 1, pp. 42–51.
14. Gitlevich, A.E., Mikhailov, V.V., Parkanskii, N.Ya, and Revutskii, V.N., *Elektroiskrovoe legirovanie metallicheskikh poverkhnostei* (Electrospark Doping of Metal Surfaces), Chisinau: Shtiintsa, 1985.
15. Tushinskii, L.I. and Tikhomirova, L.B., Structure Aspects of Improvement of Construction Strength of Alloys, *Fiz.–Khim. Mekh. Mater.*, 1975, no. 5, pp. 10–22.
16. Mikhailyuk, A.I., Ivanov, A.N., Kaputkina, L.M., and Gitlevich, A.E., Features of Formation of Substructure of Surface Layer of Some Metals after Electrospark Doping and Surface Plastic Deformation, *Elektroiskrovaya Obrab. Mater.*, 1995, no. 1.
17. Papshev, D.D., *Otdelochno-ukreplyayushchaya obrabotka poverkhnostnym plasticheskim deformirovaniem* (Finishing–Strengthening Treatment by Surface Plastic Deformation), Moscow, 1978.
18. Mikhailyuk, A.I., Rapoport, L.S., Gitlevich, A.E. et al., Influence of Surface Plastic Deformation on Characteristics of Electrospark Coatings Based on Iron, *Elektron. Obrab. Mater.*, 1991, nos. 1 and 2.
19. Ivanov, A.N., Fomicheva, E.I., and Shelekhov, E.V., Application of Slipping Beam for Study of Surface Layers by X-ray Diffractometer of General Purpose, *Zavod. Lab.*, 1989, no. 12, pp. 41–47.
20. Zhitaru, R. and Rahvalov, W., The Influence of Rest on the Micromechanical Properties of Preliminarily Deformed MgO Single Crystals, *Phys. Solid State*, 2007, vol. 49, no. 5, pp. 839–841.
21. Zhitaru, R. and Rahvalov, W., Influence of the Stresses of Predeformed InP Crystals on Acoustic Emission under Indentation, *Proc. SPIE*, 1999, vol. 4068, pp. 65–73.
22. Utyashev, F.Z. and Raab, G.I., Effect of the Deformation Zone on the Structure Refinement in Metals, *Fiz. Met. Metalloved.*, 2007, vol. 104, no. 6, pp. 605–617 [*Phys. Met. Metallography* (Engl. Transl.), vol. 104, no. 6, p. 582].
23. Koneva, N.A. et al., Accumulation of Defects, Stored Elastic Energy, and Self-Organization of Structure, *Fizicheskie aspekty prognozirovaniya razrusheniya i formirovaniya geterogennykh materialov* (Physical Aspects of Prediction of Destruction and Formation of Heterogeneous Materials), Leningrad: Ioffe FTI, 1987, pp. 137–148.
24. Vladimirov, V.I., *Fizicheskaya priroda razrusheniya metallov* (Physical Nature of Destruction of Metals), Moscow: Metallurgiya, 1984.
25. Noskova, N.I., Vil'danova, N.F., Churbaev, R.V. et al., Nanotechnology of Obtaining, Structure and Properties of Nanocrystalline Alloys Based on Aluminum with Small Additives of Rare–Earth and Transition Metals, *Nanotekhnika*, 2006, no. 1, pp. 57–63.
26. Korobeinik, V.F., Rudyuk, S.I., and Korobeinik, S.V., Feature of Formation of Microtopography, Structure, and Substructure of Surface Layer at Electrospark Doping, *Elektron. Obrab. Mater.*, 1989, no. 1, pp. 15–17.
27. Usov, S.V., Drozdov, Yu.N., Belobragin, Yu.A. et al., Combined Processes of Electroerosion Strengthening for Improvement of Limited Lifetime of Machine Pieces, *Vestn. Mashinostroeniya*, 1986, no. 7, pp. 59–62.
28. Pyachin, S.A., Zavodinskii, V.G., and Pugachevskii, M.A., Structure–Phase Transformations of Copper Foil under the Effects of Spark Discharge, *Fiz. Met. Metalloved.*, 2006, vol. 102, no. 2, pp. 171–177 [*Phys. Met. Metallography* (Engl. Transl.), vol. 102, no. 2, p. 157].

ISSN 1068-3755, Surface Engineering and Applied Electrochemistry, 2008, Vol. 44, No. 5, pp. 390–395. © Allerton Press, Inc., 2008.
Original Russian Text © E.P. Grishina, A.V. Zhirov, P.N. Belkin, A.I. Dikusar, 2008, published in Elektronnaya Obrabotka Materialov, 2008, No. 5, pp. 57–62.

ELECTRICAL PROCESSES IN ENGINEERING AND CHEMISTRY

Influence of Anodic Electrothermochemical Oxidation on the Corrosion Stability of Steel 45

E. P. Grishina[a], A. V. Zhirov[b], P. N. Belkin[b], and A. I. Dikusar[c]

[a] *Institute of Chemistry of Solutions, Russian Academy of Sciences, ul. Akademicheskaya 1, Ivanovo, 153045 Russia*
E-mail: epg@isc-ras.ru

[b] *Nekrasov State University, Kostroma, ul. Pervogo maya 14, Kostroma, 156961 Russia*
E-mail: belkin@kmtn.ru

[c] *Institute of Applied Physics, Academy of Sciences of Moldova, ul. Academiei 5, Chisinau, MD-2028 Republic of Moldova*
E-mail: dikusar@phys.asm.md

Received April 1, 2008; in final form, April 29, 2008

Abstract—The possibility to increase the corrosion stability of steel 45 by its anodic electrothermochemical oxidation in aqueous solutions of ammonium acetate (10–15%) is shown. Tests of oxidized samples in a sulfuric acid solution (0.5 M) allowed finding a shift of their potential to the positive range (up to 0.3 V) with respect to the platinized electrode, which was accompanied by a decrease in the conductivity of the oxide layer. The minimum corrosion rate [0.7 g/(m^2 day)] in the 5% NaCl solution was obtained for the specimen oxidized at a voltage of 200 V.

DOI: 10.3103/S1068375508050098

INTRODUCTION

Oxidation of steel pieces in the practice of mechanical engineering is applied for deposition of protective-decorative coatings, which are stable under conditions of atmospheric corrosion. At present, anodic, chemical, and thermal methods of oxidation are widely used; the obtained thickness of the coatings depends on the conditions of the oxide layer formation and ranges within fractions of microns to several tens of microns [1]. Each of the given methods is characterized by certain advantages [2], but all of them have a common disadvantage: the great time of the piece treatment—from 30 min to several hours.

In recent years, a new promising method of short-term electrothermochemical oxidation of metals has been developed—high-temperature oxidation under conditions of anodic electrolytic heating [3]. In the given method, the treated piece serves an anode, and the cathode is the electrolytic cell walls; their area must exceed the anode area by approximately an order of magnitude. In voltastatic conditions, this ratio of the areas of the electrodes allows the appearance of a current density of up to several A/cm^2 on the anode. The treated piece is heated up to several hundreds of degrees, the electrolyte boils in the near-anode space, and a gas–vapor envelope (GVE) is formed. In the GVE, localization of further release of heat energy occurs; it is consumed for heating of both the electrolyte and the piece. By varying the voltage of the electrolyzer, it is possible to control the treated piece's temperature (from 500 to 1000°C), and, by varying the composition of the aqueous electrolyte solution, it is possible to control the type of action (thermal/thermochemical). The interaction of the metal or alloy with water vapors in the GVE leads to the formation of an oxide film on the anodically polarized piece.

Earlier, studies were carried out [4, 5] concerned with high-velocity electrothermochemical treatment of metals and alloys in view of surface modification with nitrogen at 750°C; this resulted in an increase in not only the hardness, fatigue resistance, and other physicomechanical characteristics of the treated samples but also in their corrosion stability. The possibilities of efficient oxidation under other thermochemical conditions have not been studied yet.

The aim of the present paper is to study the influence of the temperature and the concentration of the electrolyte on the corrosion stability of oxide coatings obtained on steel St 45 at high temperature oxidation under conditions of anodic electrolytic heating.

EXPERIMENTAL

High temperature oxidation of samples under conditions of anodic electrolytic heating was carried out in aqueous solutions of CH_3COONH_4 (ammonium acetate) with concentrations of 100 and 150 g/l. The components of the given salt do not penetrate the surface oxide film in the process of the treatment, and the specific electroconductivity of the solutions (not below 50 mS cm^{-1}) is sufficient for anodic heating in a wide temperature range (500–1000°C) [3].

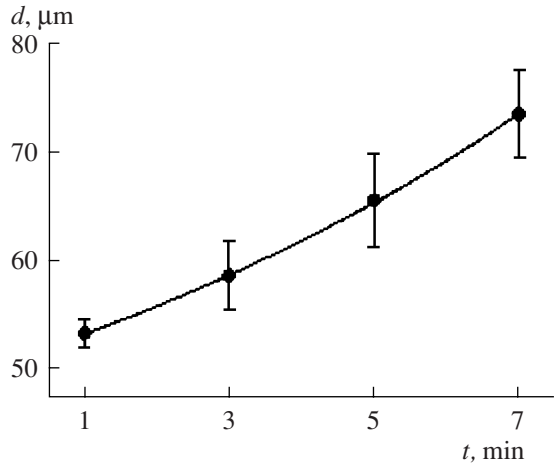

Fig. 1. Dependence of the thickness of the oxide layer on the sample of St 45 on the treatment time at $U = 200$ V. The ammonium acetate concentration is 100 g/l.

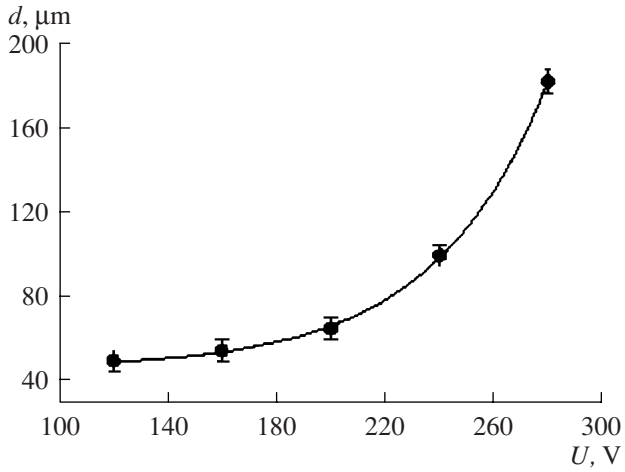

Fig. 2. Dependence of the thickness of the oxide layer on the sample of St 45 on the heating voltage. The treatment time is 5 min, and the ammonium acetate concentration is 100 g/l.

For the work, cylindrical samples of St 45 (12 × 12 mm) were used; one of their end faces has an opening with a diameter of 5 mm and a depth of 7 mm for a thermocouple. Anodic heating was carried out in a cylindrical operation chamber with electrolyte spillover (the consumption of the treatment solution was 5 l/min, and the mean temperature was 30°C).

Oxidation was carried out at a voltage across the cell U_c of 160–280 V for 1–5 min. The samples were cooled in air in order to avoid cracks and stripping of the coatings. What is more, additional oxidation in air favorably affects the protective properties of the oxide layer [4, 5].

The X-ray phase analysis of the oxide layer was carried out by means of a DRON-UM1 installation (Cu-K_α-radiation), and the layer thickness was measured by virtue of a PTM-3M microscope (lens $F = 6.3$ cm, $A = 0.6$).

The corrosion behavior of the coatings was studied by the potentiometric and impedance methods in a 0.5 M solution of sulfuric acid at a temperature of 20°C [6, 7]. The studied electrode potential in time was measured with respect to a saturated silver–chloride electrode by means of a digital voltmeter (Shch 300). The resistance and capacitance of the electrodes in the corrosion process was measured by virtue of an alternating current bridge (P 5021) and a platinized platinum electrode at an alternating current frequency of 1 kHz and a voltage across the cell of 5 mV. The studied sample surface was 5.65 cm^2.

RESULTS AND DISCUSSION

Treatment of the samples prepared of St 45 in aqueous solutions of ammonium acetate by the method of high temperature oxidation under conditions of anodic electrolytic heating leads to formation of a dark gloss film on the sample surface. According to data of the X-ray phase analysis, the film consists of Fe_2O_3 and Fe_3O_4. The dependence of the layer thickness on the treatment duration is close to a linear one (Fig. 1), and that on voltage is close to the exponential one (Fig. 2). An increase in the concentration of ammonium acetate does not qualitatively change the given dependences but causes a weak increase in the temperature of the treated sample at identical voltage across the cell (Fig. 3).

The maximum thickness of the surface oxide layer was obtained at $U_c = 280$ V, but, in this case, blisters of the oxide layer and an increase in the surface roughness along the sample edges were observed.

Potentiometric studies have shown that the corrosion potential E_c of the treated samples depends on the conditions of the electrothermochemical treatment. If

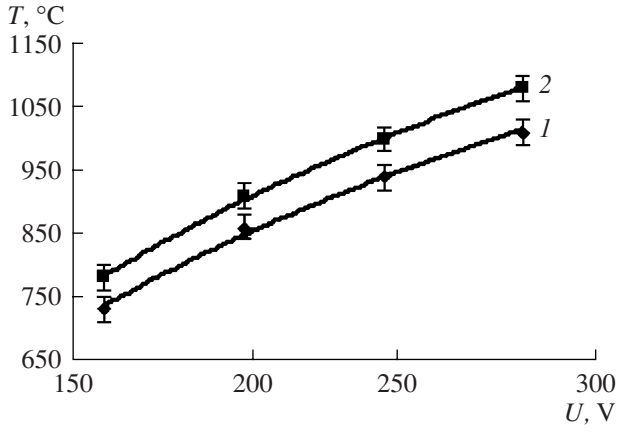

Fig. 3. Voltage–temperature characteristics of heating of the samples of St 45 in an aqueous solution of ammonium acetate with concentrations 100 g/l (*1*) and 150 g/l (*2*).

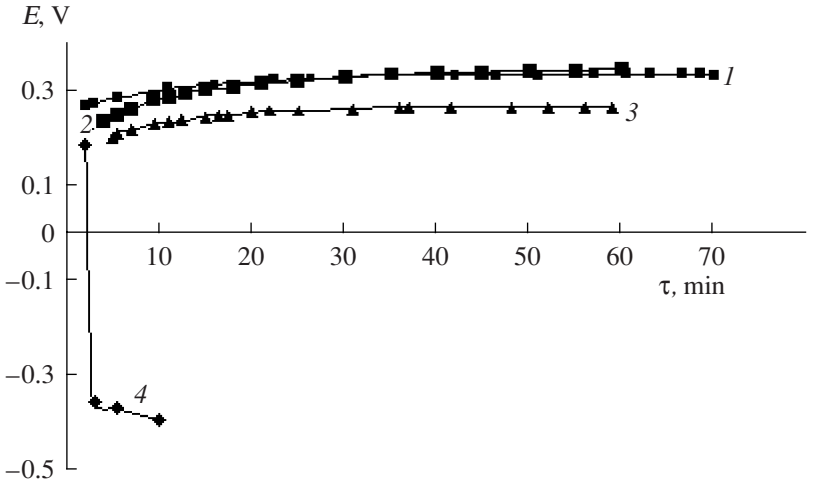

Fig. 4. Dependence of the sample potential on the time of the tests in a sulfuric acid solution (0.5 M) after oxidation for 1 min. The ammonium acetate concentration is 100 g/l. The oxidation voltage is the following in V: 200 (*1*), 280 (*2*), 240 (*3*), and 160 (*4*).

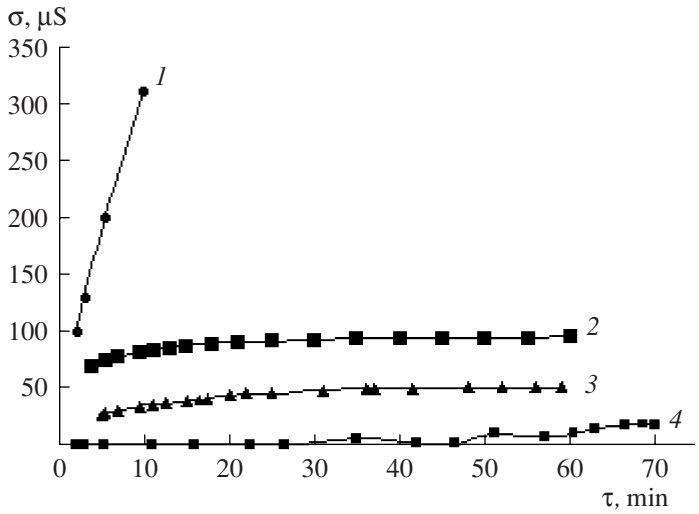

Fig. 5. Dependence of the sample conductivity on the time of the tests in the sulfuric acid solution (0.5 M) after oxidation for 1 min. The ammonium acetate concentration is 100 g/l. The oxidation voltage is the following in V: 160 (*1*), 280 (*2*), 240 (*3*), and 200 (*4*).

the potential of the electrode that was not subjected to oxidation is –0.43 V, then, as a result of formation of the oxide layer, its ennoblement to values of 0.20–0.40 V takes place.

The E_c behavior in time is affected most appreciably by the oxidation voltage (Figs. 4–7). In all the considered cases, the potential of the samples obtained at U_c = 160 V after several minutes of exposure in the H_2SO_4 solution sharply decreased to the values characteristic of nonoxidized steel 45. Herein, an increase in the capacitance with a rate of 10 and 2 μF/min took place for the samples treated in CH_3COONH_4 solutions with concentrations of 100 and 150 g/l, respectively, as well as an increase in the conductivity of the studied sample (Fig. 5). The presented experimental data testify to the high rate of interaction of the relatively thin oxide layer with the acid solution in this case and, therefore, to the low protective properties of the film.

A behavior opposite to the one considered above is found for the samples treated at U_c = 280 V. In this case, in contrast to the previous one (though the samples also had raised roughness), an oxide film was formed having, apparently, a great number of through pores, since, at immersion into the acid solution, the electrode potential immediately took on negative values. However, then E_c began to increase rapidly, and, after 10–30 min, its value approached the potential of the samples treated at U_c = 200 and 240 V (Figs. 6–8). Probably, this

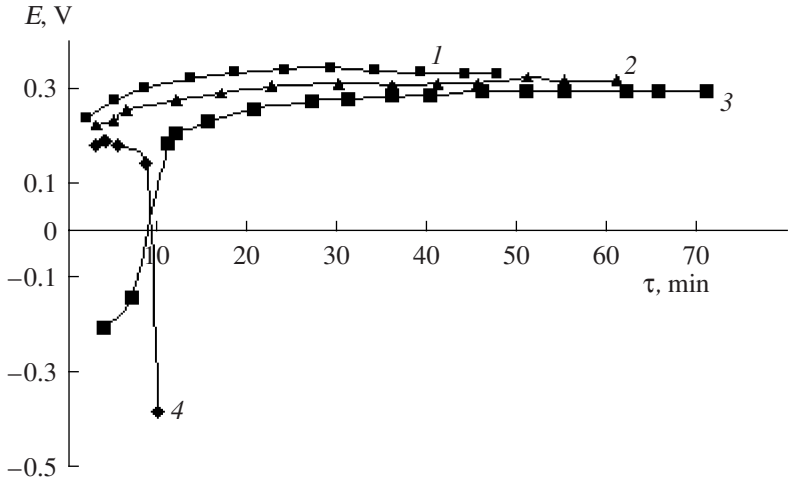

Fig. 6. Dependence of the sample potential on the time of the tests in the sulfuric acid solution (0.5 M) after oxidation for 1 min. The ammonium acetate concentration is 150 g/l. The oxidation voltage is the following in V: 200 (*1*), 240 (*2*), 280 (*3*), and 160 (*4*).

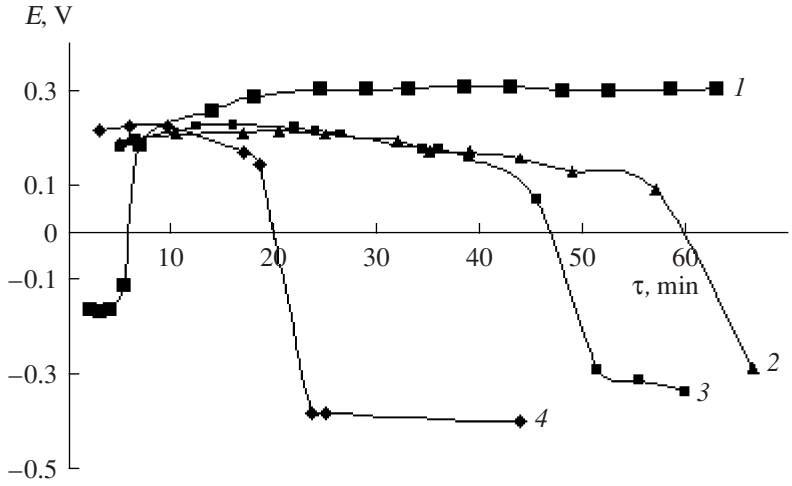

Fig. 7. Dependence of the sample potential on the time of the tests in the sulfuric acid solution (0.5 M) after oxidation for 5 min. The ammonium acetate concentration is 100 g/l. The oxidation voltage is the following in V: 280 (*1*), 240 (*2*), 200 (*3*), and 160 (*4*).

is due to the fact that, in the film pores, "bare" steel corrodes by the electrochemical mechanism and the anodic process and, being narrowly localized by the sizes of the pore base, proceeds at a high current density leading to passivation of these surface sections.

The developed surface of the sample oxidized at 280 V is also confirmed by its high, as a rule, capacitance in comparison with the one observed after oxidation at 200 and 240 V. At the beginning of the measurement, the capacitance of the samples oxidized at 280 V was 20 μF; for the samples oxidized at 200–240 V, values of 2–4 μF were obtained (a 10% ammonium acetate solution, treatment time of 1 min).

An increase in the time of oxidation does not lead to improvement of the corrosion characteristics of the treated samples. First, a decrease in the initial potential values (in some cases, up to negative values) is observed in the corrosion tests. Second, the samples treated in the 10% ammonium acetate solution are characterized by a tendency for the potential decrease in time, up to negative values (except for the case of treatment at U_z = 280 V) (Fig. 7). This potential variation in time at an increase in the sample treatment time is probably due to the growth of the oxide layer thickness (the resistance increases) and the appearance of internal stresses in it, leading to discontinuity of the film. It is also possible that, at an increase in the process time, microdischarge processes leading to the appearance of a great number of pores in the layer are intensified in the VGE.

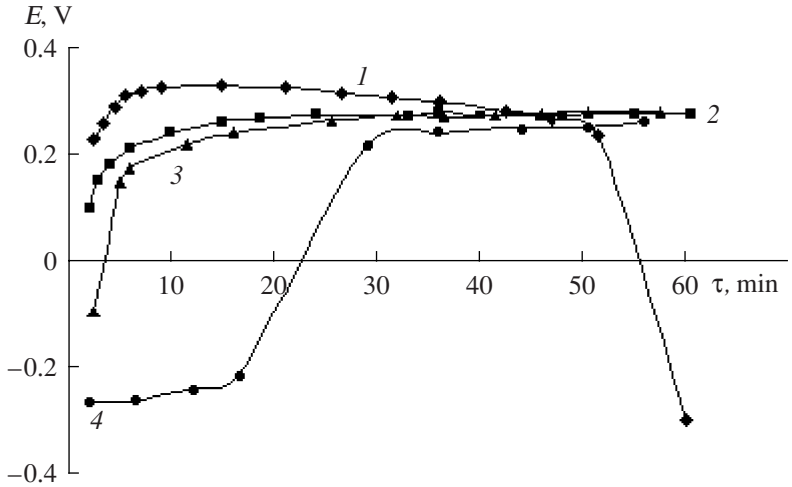

Fig. 8. Dependence of the sample potential on the time of the tests in the sulfuric acid solution (0.5 M) after oxidation for 5 min. The ammonium acetate concentration is 150 g/l. The oxidation voltage is the following in V: 160 (*1*), 200 (*2*), 240 (*3*), and 280 (*4*).

It also follows from the obtained data that an increase in the concentration of ammonium acetate does not lead to a significant improvement of the protective properties of the formed oxide layer, although insignificantly higher initial values of the sample potential (U_z = 160 V) and its later shift to the negative range are observed in corrosion tests.

It follows from the obtained data that the optimum modes of oxidation of steel St 45 are in the voltage range of 200–240 V (corresponding to the anode temperature of 850–950°C) and a treatment time of 1–3 min. The potential of the samples treated at the given voltages is ≈0.3 V; the conductivity of the oxide layer is 10–50 and 30–100 μS for the 10 and 15% ammonium acetate solutions, respectively; and the capacitance is 10–40 μF.

For confirmation of the characteristics of the corrosion stability of the steel 45 after the treatment, gravimetric tests of the oxidized samples were carried out by the method of immersion into a 5% sodium chloride solution. After 96 h of the tests, the rate of corrosion of the steel 45 oxidized at a voltage of 200 V in the 10% ammonium acetate solution was 0.7 g/(m^2 day), which was lower by an order of magnitude than the corrosion rate of the untreated samples of 8.4 g/(m^2 day). For the samples treated at voltages of 160 and 280 V, the corrosion rate was 4.8 and 3.1 g/(m^2 day), respectively [8].

CONCLUSIONS

1. Electrothermochemical treatment (anodic electrolytic heating) of steel 45 in an aqueous solution of ammonium acetate leads to formation of surface oxide layers characterized by well pronounced protective properties. Formation of the oxide layer is accompanied by ennoblement of the potential by more than 0.6 V, an increase in the resistance, and a decrease in the capacitate of the electrode.

2. The study of the voltage influence on the protective properties of the oxide layers has shown that the densest and most chemically stable coatings may be obtained at oxidation of samples at voltages of 200–240 V, which corresponds to treatment temperatures of 850–950°C.

3. It is found that, in the ammonium acetate concentration range of 100–150 g/l, the corrosion characteristics of the treated samples are close in their values. An increase in the treatment time (by more than 3 min) leads to the development of an irregular surface on the pieces, which unfavorably affects the corrosion characteristics.

ACKNOWLEGMENTS

This work was carried out according to a plan of research with financial support from the Ministry of Education and Science of the Russian Federation.

REFERENCES

1. *Anodnye oksidnye pokrytiya na metallakh i anodnaya zashchita* (Anodic Oxide Coatings on Metals and Anodic Protection), Frantsevich, I.N., Pilyankevich, A.N., Lavrenko, V.A., and Vol'fson, A.I., Eds., Kiev: Naukova Dumka, 1985.
2. Lavorko, P.K., *Oksidnye pokrytiya metallov* (Oxide Coatings of Metals), Moscow: Mashgiz, 1963.
3. Belkin, P.N., *Elektrokhimiko-termicheskaya obrabotka metallov i splavov* (Electrothermochemical Treatment of Metals and Alloys), Moscow: Mir, 2005.
4. Chernova, G.P., Bogdashkina, N.L., Parshutin, V.V., Revenko, V.G., Tomashov, N.D., Belkin, P.N., Pasink-

ovskii, E.A., and Faktorovich, A.A., Electrochemical and Corrosion Behavior of Steel 40Kh Nitrided in "Electrolytic Plasma", *Zashch. Met.*, 1984, no. 3, pp. 408–411.

5. Revenko, V.G., Chernova, G.P., Parshutin, V.V., Bogdashkina, N.L., Tomashov, N.D., Belkin, P.N., and Pasinkovskii, E.A., Influence of Parameters of Electrolyte Nitrogenization Process on Protective Properties of Conversion Coatings, *Zashch. Met.*, 1988, no. 2, pp. 204–210.
6. Godovskaya, K.I. and Tolstaya, L.T., *Laboratornyi praktikum po tekhnicheskomu analizu i kontrolyu kachestva elektrokhimicheskikh pokrytii* (Laboratory Course on Technical Analysis and Control of Quality of Electrochemical Coatings), Moscow: Mashinostroenie, 1984.
7. *Laboratornye raboty po korrozii i zashchite metallov* (Laboratory Works on Corrosion and Protection of Metals), Tomashov, N.D., Zhuk, N.P., Titov, V.A., and Vedeneev, M.A., Eds., Moscow: Metallurgiya, 1971.
8. Zhirov, A.V., Anodic Oxidation of Steel 45 in Aqueous Electrolytes, *Materialy V mezhdunarodnogo nauchno-prakticheskogo seminara "Sovremennye elektrokhimicheskie tekhnologii v mashinostroenii"* (Proc. V Int. Sci.-Pract. Seminar "Modern Electrochemical Technologies in Mechanical Engineering), Ivanovo: IGKhTU, 2005, pp. 83–85.

ISSN 1068-3755, Surface Engineering and Applied Electrochemistry, 2008, Vol. 44, No. 5, pp. 396–400. © Allerton Press, Inc., 2008.
Original Russian Text © M. Cojocaru, I. Ciuca, L. Druga, G. Cosmeleata, 2008, published in Elektronnaya Obrabotka Materialov, 2008, No. 5, pp. 63–68.

ELECTRICAL PROCESSES IN ENGINEERING AND CHEMISTRY

Empirical Exposition of the Adsorption's Ionic Mechanism on Gaseous Nitriding[1]

M. Cojocaru, I. Ciuca, L. Druga, and G. Cosmeleata

Polytechnic University of Bucharest, Splaiul Independentei 313, Bucuresti, 060042 Romania

E-mail: office@uttis.ro

Received July 1, 2008

Abstract—The countless contradictions of practical or theoretical nature associated with the gaseous nitriding process, for a long time, have forced researchers to study in depth the theoretical aspects of the process. The analysis of the main phases of the mass transfer process occurring within the nitriding process led to the conclusion that the phases responsible for the series of noted contradictions are the ones corresponding to the reactions in the environment and at the environment–product interface. Through theoretical studies and experimental verification, it was discovered that, in the reaction space, under the specific conditions for the gaseous nitriding to occur, the ammonia most probably undergoes, in the areas close to the metallic surfaces, at the same time as the thermal catalytic dissociation, an ionization process that is followed as a consequence by the appearance of a greater number of anions and anionic complexes. In this paper are presented the results of the studies and experimental research related to the adsorption's ionic mechanism on nitriding in a gaseous medium.

DOI: 10.3103/S1068375508050104

INTRODUCTION

The classic theory of the adsorption of the Nitrogen resulting through thermal catalytic dissociation of ammonia cannot explain the series of situations appearing repeatedly during nitriding:

—the nonmonotonous variation of the adsorbed nitrogen quantity on the increase of the ammonia dissociation degree;

—the intensifying of the nitriding process kinetics through the existence of transition metals in contact with the nitriding media of completely different nature than that of both the nitrogen and the material subject to nitriding.

The comparative analysis (based on the energy grounds) of the ammonia thermal catalytic dissociation reactions and the ionization of the molecules with the creation of anions or cations has led to the conclusion that the most likely decomposition mechanism is the one of ionization with the creation of anions.

(a) The ammonia thermal catalytic dissociation global reaction

$$NH_3 \longrightarrow N + H, \quad (1)$$

represents a strongly endothermic reaction with the quantity of energy necessary for it to develop being 11.2 eV. The sum of the necessary energies for the three phases of decomposition

$$NH_3 \longrightarrow NH_2 + H, \quad (2)$$

$$NH_2 \longrightarrow NH + H, \text{ and} \quad (3)$$

$$NH \longrightarrow N + H, \quad (4)$$

is 4.2 eV (reaction 2), 3.64 eV (reaction 3), and 3.36 eV (reaction 4) giving a total consumption of 11.2 eV.

(b) The ionization of the ammonia molecule with the creation of its anions

$$NH_3 + \bar{e} \longrightarrow NH_3^-, \quad (5)$$

is exothermal with the quantity of energy released being +2.8 eV.

(c) The ionization of the ammonia molecule with the creation of its cations

$$NH_3 \longrightarrow NH_3^+ + \bar{e}, \quad (6)$$

is strongly endothermic with the quantity of energy necessary for it to develop being on the order of 10.34 eV.

All these observations lead to the conclusion that, under the conditions in which the nitriding process in a gaseous atmosphere develops, the appearance of NH_3^- type anions is very probable (along with type NH_x neutral radicals or other types of ions). This conclusion, if proved valid, would allow understanding the possible contradictions noted and, at the same time, modify the current perception of the adjustment and control mode of the classic nitriding parameters.

MATERIALS AND METHODS

The experimental research has pursued the empiric exposition of the presence of type NH_3^- anions on the gaseous nitriding occurring in an ammonia atmosphere

[1] The text was submitted by the authors in English.

and, by this, the adsorption's ionic mechanism in the case of this variant of thermal processing as compared to the free atoms adsorption mechanism. The starting point was the idea that the creation of the ammonia anions is possible under the conditions specific to the development of the classic nitriding process and the hypothesis that, in this situation, the presence of an electric field of a certain intensity should result in an orientation and an acceleration of the ions in the electric field with the consequence being the forming of the kinetics of the different polarity samples' layers existing in the field. Considering the desired outcome, in the first stage of the research, it was sought to determine through calculations the thermal and electric conditions in which it is possible for the formation of type NH_3^- anions and, following that, through experiments, it was sought to confirm the theoretical reasoning.

The material on which the research was performed was technical pure iron, as it allows more precise exposing of different structural components of the nitrided layer and their dimensions under real processing conditions.

The assembly used for the research is presented in Fig. 1; it allowed strict control of the processing's electric and geometric parameters.

Cylindrical samples were used (d20 × 30 mm (anodes)) with a dimensional relation to the coaxial central electrode and the cathode (D28 × 150 mm, D/d = 1.4). The anodes and the cathodes were made from technical pure iron (Fe-ARMCO). The nitriding results were analyzed using specific metallographic methods and optical microscopy using a Reichert microscope. There were also performed measurements of the samples' mass variation as the nitriding process continued under various conditions.

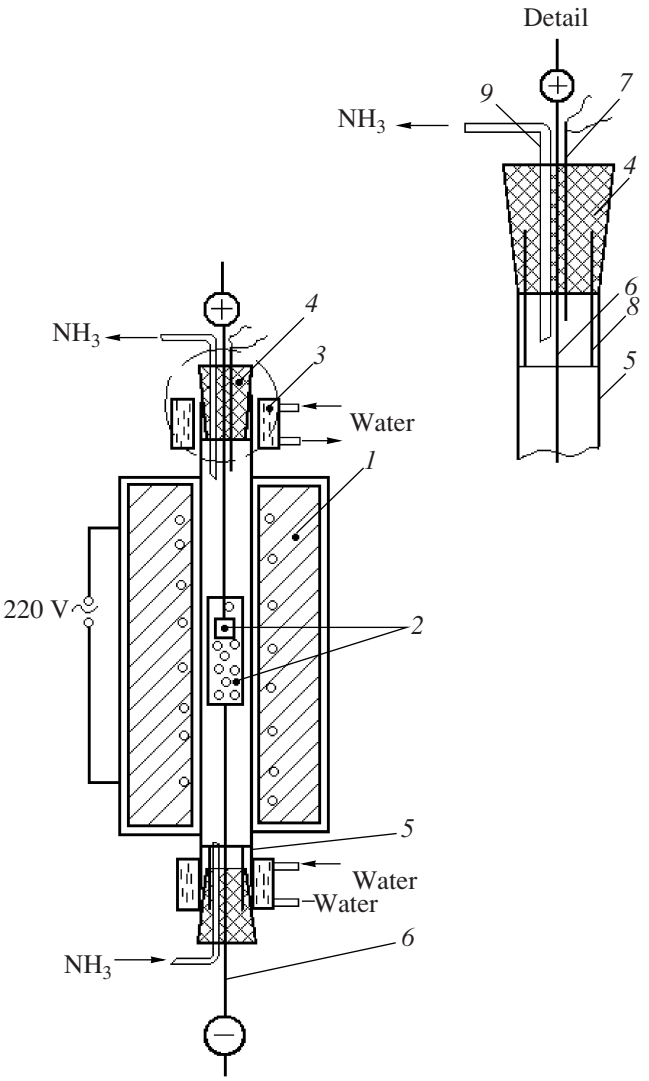

Fig. 1. Installation for exposing the presence of anions on gaseous nitriding. *1*, electric furnace; *2*, coaxial electrodes; *3*, water coolers; *4*, insulators; *5*, refractory steel pipe; *6*, electrode; *7*, thermocouple; *8*, centering elements; *9*, exhaust pipe for ammonia dissociation products

RESULTS AND DISCUSSION

The analysis on energy grounds of the ammonia molecule ionization emphasizes the fact that the forming of the ammonia's negative ion, in the case when there are created the conditions for the phenomenon to occur, can develop with an energy probability higher than that of thermocatalytic dissociation. One such mechanism of electron exchange between the gas' molecules used for the saturation of the metallic surface is made possible by the existence of the double electric layer in the zone near the metallic surface. Besides this, on the surface of the metal, the crystalline matrix is not electrically balanced, which is equivalent to exceeding the number of electrons in these areas. When the ammonia molecules make contact with the metallic surface, it is possible for there to occur a transfer of electrons towards the gas molecules. The possibility for the electrons to adhere is ensured by the presence of stable external orbits for the atoms that compose the molecules of gas. The ammonia neutral molecules' affinity for the electrons can be explained using the energy released or, on the contrary, that consumed during the process of merging between the electron and the molecule (the value corresponding to the affinity towards the electron is +2.85 eV for the ammonia molecule). The energy release when forming the metallic anions by the contact of the gas molecules with the metallic surface represents a necessary but not sufficient condition for the electron to adhere. The value of the energy necessary for the interaction of the gas molecules with the metallic surface must be equivalent to the value of the energy needed to tear apart the electron, which, in the case of the iron matrixes, is 4.31 eV. In the presence of submicron oxide films (a real occurrence in the thermochemical processing), this value is 3.0 eV.

The energy necessary to tear apart the electron and to pass over the barrier of the potential comes from the

Table 1. The energies of the electrons in the electric double layer after contact with the nitriding gas (ammonia)

T, °C	T, K	W_1, eV	W_2, eV	$W = W_1 + W_2 + S_{NH_3}$ **AMMONIA**
100	373	3.21×10^{-2}	4.81×10^{-2}	2.9302
200	473	4.07×10^{-2}	6.10×10^{-2}	2.9517
300	573	4.94×10^{-2}	7.41×10^{-2}	2.9735
400	673	5.80×10^{-2}	8.7×10^{-2}	2.995
500	773	6.66×10^{-2}	9.99×10^{-2}	***3.0165***
600	873	7.53×10^{-2}	11.29×10^{-2}	***3.0382***
700	973	8.39×10^{-2}	12.58×10^{-2}	***3.0597***

following: the electrons, the kinetic (thermal) energy, the molecule's kinetic energy transferred to the electron at the moment the molecule impacts the metallic surface, and the energy corresponding to the molecule's affinity towards the electron.

The kinetic energy of the ammonia molecule at different temperatures can be calculated from the following relation:

$$W_1 = \frac{m\varpi^2}{2} = kT, \quad (7)$$

where ϖ represents the average speed of the molecule; m is the mass of one molecule; and k is the Boltzmann constant, which is equal to 1.38×10^{-23} J/K = $1.38 \times 10^{-23}/1.6 \times 10^{-19}$ eV.

The average kinetic energy (thermal energy) of the electrons at different temperatures can be determined with the following relation:

$$W_2 = \bar{\varepsilon}_i = 3/2kT. \quad (8)$$

The calculated values for the electron's energy in the area of contact between the metallic surface and the molecule of nitriding gas (ammonia) in the range of temperatures between 100–700°C are summarized in Table 1.

The analysis of the results stated in Table 1 confirms the information verified in common practice: nitriding in ammonia can develop at temperatures over 450°C (at which temperature the appearance of NH_3^- is certain). On the contrary, in nitrogen, it is impossible for the process to develop. The calculations confirm the great stability of the molecule in the range of temperatures at which gaseous nitriding develops.

The analysis of the electronic interaction mechanism, which is specific for the initial stages of the adsorption process, creates the possibility to anticipate the temperature range in which the thermal processing can occur. The conditions can also be estimated in which it develops with maximum intensity. This is possible because the forming process of the negative ions depending on the electron energy has an extreme character. The adherence of the electron to the neutral molecule takes place after the first one has sufficient energy to pass over the barrier of the potential. It is also noteworthy that both the electron and the molecule must have relatively reduced kinetic energies of ~0.1 eV. At higher values (speeds), the electron will slide alongside the molecule unable to interact with the later. For values of the energy equivalent to the energy necessary to pass over the barrier of the potential, the electron at the end of the mid free way will have a kinetic energy close to zero with this fact supporting the maximal development of the process of "adherence" to the neutral molecule (in other words, of the anions forming process). When the electrons have energy values higher than the energy value necessary to pass over the barrier of the potential, an increasingly higher proportion of the electrons will slide along the molecules unable to interact with the later ones (a phenomenon that implies a decrease of the proportion of anions).

Following this first phase, it became necessary to determine in theory the energy conditions that must be created in order to make possible an acceleration of the anions in the electric field created. The causes that determine this problem that are to be clarified are as follows:

—At reduced values of the electric field intensity generated in the space between the electrodes (the part to be nitrided; the cathode and the muffle in which the process develops), the orientation and the effective acceleration of the anion in the field cannot occur due to the energy ceded to the electrons from the electric double layer of the product's surface being insufficient to stimulate the emission of the electrons on the surface.

—At values of the applied electric field intensity that are too high, it is possible to initiate a spark type electrical discharge. The explanation for this is as follows: the increase in the energy of the electrons emitted by the anode surface, following the energy intake caused by the anions strongly accelerated in the electric field, causes an increase in the number of electrons that can't interact with neutral molecules of ammonia (a phenomenon that will cause a reduction of the anion proportion in the space between the electrodes and, as

Table 2. The modification of the NH_3^- anions' energy under the influence of the electric field*

U, V	E, V/m	W, eV-S (2.8 eV), for T, K							
		573		673		773		873	
		K.T	E.λ	K.T	E.λ	K.T	E.λ	K.T	E.λ
500	148800	0.049	0.037	0.058	0.043	0.066	0.050	0.075	0.056
1000	297600		0.074		0.086		0.099		***0.112***
1500	446400		0.115		0.135		***0.156***		0.176
2000	515200		0.148		***0.174***		0.200		0.226
2500	744000		***0.185***		0.218		0.250		0.282
3000	892800		0.221		0.260		0.299		0.337
3500	1041600		0.260		0.305		0.350		0.396
4000	1190400		0.297		0.349		0.401		0.453

* The data in the table does not include the corresponding value for the ammonia molecule's affinity for the electron.

a consequence, decrease the kinetics for layer forming). With the increase in the energy of the electric field applied, the proportion is also amplified of the rapid electrons capable, through collision with the neutral molecules, of leading to the ionization of the later with the formation of type NH_x^+ cations.

As a result, there must be an optimal value of the electric field intensity in order for the effect of the anions' presence to become noticeable due to the intensification of the nitriding process of the anode at the same time as a reduction of the cathode nitriding kinetics.

The general level of the ion's energy in the presence of the electrical field can be calculated using the following relation:

$$W = E\lambda + kT + S, \tag{9}$$

where E is the electrical field intensity, V/m; and λ is the length of the average free way, m.

$$\lambda_i = \lambda_0 \frac{T_i}{T_0}, \tag{10}$$

where $\lambda_0 = 12.8 \times 10^{-8}$ m at $T_0 = 293$ K and $p = 101.3$ kPa,

k is Boltzmann's constant

$$k = \frac{1.38 \times 10^{-23}}{1.6 \times 10^{-19}} = 0.862 \times 10^{-4}\ \text{eV},$$

T is the temperature (K), and S is the ammonia molecule's affinity for the electron.

$$E = \frac{U}{r \ln \frac{R}{r}}, \tag{11}$$

where U is the applied voltage (V); r is the anode's radius, m (the part to be nitrided); and R is the coaxial electrode's radius, m, acting as the cathode (see Fig. 1).

Note. During the cycle of experiments performed, the anode's radius was set to $r = 10$ mm and the cathode's to $R = 14$ mm; thus, $R/r = 1.4$.

The results of the calculations regarding the modification of the anion's energy in the presence of the electric field are summarized in Table 2.

For the range of temperatures set for the analysis (300–600°C) and the range of voltages (500–4000 V, DC), the calculated values for the anions' energies, which are superior to those marked in the table, represent the necessary minimal values for the electrons to pass over the barrier of the potential (3.0 eV in the case of iron matrixes with submicron oxide films) and extract themselves from the double electric layer and perform the ionization of the molecule.

The calculations led to the conclusion that the actual experiments intended to expose the presence of the anions and therefore the adsorption's ionic mechanism must be performed in the range of corresponding values for the intensity of the electric field of 1.48×10^5–7.44×10^5 V/m (an applied voltage of 500–2500 V for a value of the geometric factor of $R/r = 1.4$), when the temperature of the nitriding process would in theory vary between 300 and 600°C.

The experiments were effectively performed using the installation presented in Fig. 1 at a temperature below the corresponding eutectoid transformation tem-

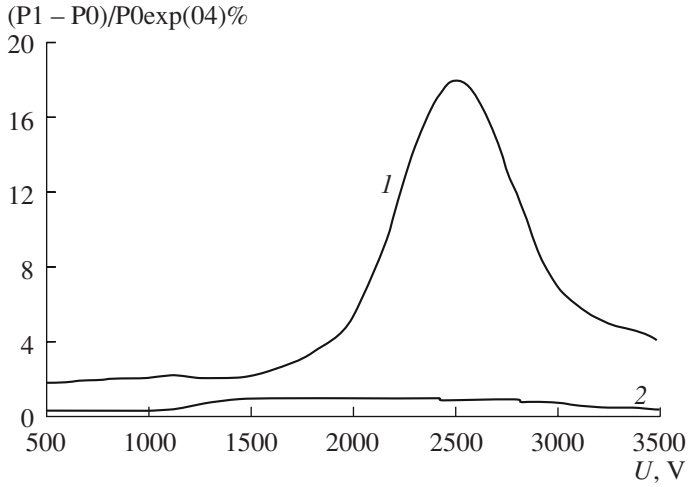

Fig. 2. Mass variations of the pure iron samples (anode and cathode) nitrided at 560°C for 2 h in the presence of an electric field.

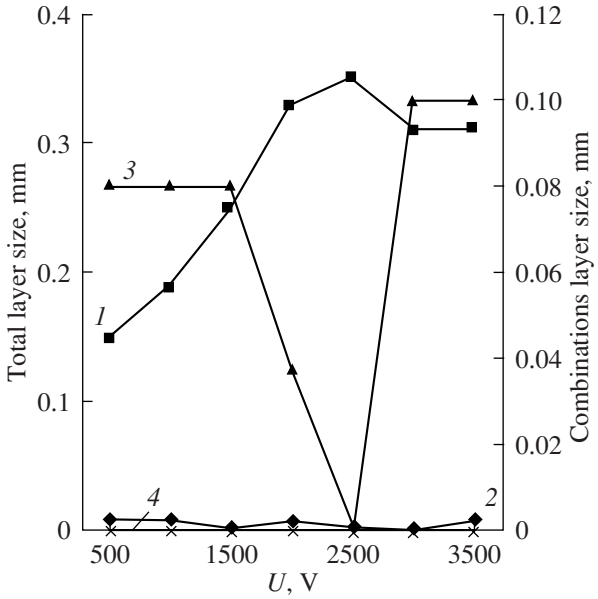

Fig. 3. The variation of the dimensions of different structural components of the nitrided layers in the electric field obtained for pure technical iron samples ($T = ct$ = 560°C, $t = ct = 2ore$).

perature in the Fe–N system (591°C), namely, 560°C, in partially dissociated ammonia atmospheres with 2 h of maintaining the temperature and with varying the applied voltage in the range of 500–4000 V. The results obtained were evaluated by calculating the mass variations and measuring the total layer and the combination zone. The results obtained are summarized in Figs. 2 and 3.

The results obtained confirm the theoretical reasoning previously given: around the value of 2500 V, there are both the maximum corresponding to the increase in the size of the nitrided layer (in general dimension and in the size of the components' area) and the maximum corresponding to the mass increases. Passing over this value implies an increase in the anions' energy. This has an effect on the proportion of anions in the space between the electrodes and on the energy associated with the electrons that leave the electric double layer. On passing this value, the effects of the presence of the electric field begin to diminish. Over a certain value (3500 V), spark type electric discharge begins to occur, which is a phenomenon that favors the amplifying of the cathode saturation kinetics.

CONCLUSIONS

The following was demonstrated using experiments: that the existence of anions on gaseous nitriding in ammonia and, therefore, in the working enclosure can coexist depending on the created conditions, as well as nondissociated ammonia molecules and their dissociation products represented by type NH_x radicals, anions, cations, etc. The possibility to accelerate the process by applying an electric field whose intensity is dependent on the process temperature and the geometric factor of the charges was underlined.

REFERENCES

1. Vedeneev, V.I., *Energia Razryva Himicheskih Svyazei*, Moskva: Izd. AN SSSR, 1962.
2. Kai, D.J. and Lebi, T., *Tablitsy Fizicheskikh i Himicheskih Postoyannyh*, Moskva: Izd. Fiz.-mat. Literatury, 1962.
3. Cojocaru, M. and Florian, E., Cementarea cu Azot, Rezultat al Schimbului de Electroni Intre Metal şi Amoniac, *Metalurgia*, 1978, no. 7.
4. Cojocaru, M. and Florian, E., Comportarea Amoniacului in Timpul Incălzirii, Explicată Prin Mecanismul Ionic de Adsorbţie, *Metalurgia*, 1978, no. 9.
5. Kostiucenco, V.M. and Urţeva, B.I., *Azotrovanie v Electrostaticheskom Pole*, Magnitogorsk, 1971.
6. Lahtin, I.M., Kogan, I.D., and Cojocaru, M., Azotirovanie v Electrostaticheskom Pole, *Electron. Obrab. Mater.*, 1974.

ISSN 1068-3755, Surface Engineering and Applied Electrochemistry, 2008, Vol. 44, No. 5, pp. 401–409. © Allerton Press, Inc., 2008.
Original Russian Text © N. Frini-Srasra, E. Srasra, 2008, published in Elektronnaya Obrabotka Materialov, 2008, No. 5, pp. 69–78.

ELECTRICAL PROCESSES IN ENGINEERING AND CHEMISTRY

Determination of Acid–Base Properties of HCl Acid Activated Palygorskite by Potentiometric Titration[1]

N. Frini-Srasra[a,b] and E. Srasra[a]

[a] *Unité de recherche sur les matériaux, CRTE, Technopole Borj Cedria, B.P. 95-2050 Hammam-Lif Tunisia*
[b] *Département de Chimie, Faculté de Sciences de Tunis, 1060 Tunis, Tunisia*
E-mail: nfrini@gmail.com

Received January 15, 2008

Abstract—The surface acidity of raw and acid activated palygorskite clay was studied by acid–base potentiometric titration. The Gran plot method was applied for the hydroxide titration, and the total surface sites (Hs) and the average number of protons reacted per surface site (*Z*) of the palygorskite samples at a given ionic strength were calculated. Acid treatment increases the clay acidity and modifies its surface charge. The point of zero charge value, which was determined by the common crossing point of *Z* vs. the pH curves performed at different ionic strengths, decreased from 8.8 to 3.5 with the acid treatment period. For illustrating the acidic characteristics of the treated and untreated palygorskite surface, three surface protonation models were tested: (a) the one site one pK_a model, $\equiv SOH \rightleftharpoons \equiv SO^- + H^+$; (b) the two sites two pK_as model, $\equiv S_IOH \rightleftharpoons \equiv S_IO^- + H^+$ and $\equiv S_{II}OH \rightleftharpoons \equiv S_{II}O^- + H^+$; and (c) the one site two pK_a model, $\equiv SOH \rightleftharpoons \equiv SO^- + H^+$ and $\equiv SOH + H^+ \rightleftharpoons \equiv SOH_2^+$. The three surface protonation models sufficiently describe the surface properties and their evolution with the acid treatment.

DOI: 10.3103/S1068375508050116

INTRODUCTION

Clay minerals have many applications related to adsorption and catalysis, which use the acidic–basic properties of the clay mineral surface. Their textural and structural properties may lead to a wide range of applications, especially if activation is able to increase the number and strength of the surface acidic sites. There are some studies on the acid activation of palygorskite: [1] investigated the effect of magnesium on structural alteration and on the specific surface area and porosity, and [2] proposed a mechanism of acid activation of magnesic palygorskite. [3] studied the structural and textural modification of palygorskite under acid treatment in comparison with a Spanish sepiolite treated under the same experimental conditions. [4] studied the influence of octahedral sheet composition on the kinetics of acid leaching of palygorskite [5, 6] and showed that Tb^{3+} and La^{3+} increase the acid sites number and improve the catalytic properties of acid activated palygorskite. Activated palygorskite provides excellent catalytic activity in the rearrangement of the chalcone epoxide reaction [7]. The rearrangement of α-epoxyketone (chalcone epoxide) was found to yield the E(–) enolic form of 1,3-diphenyl-1,3-propanedione, indicating that the proton migration takes place from the less favoured direction of the epoxy ring. It was observed that acid activated palygorskite gives a higher yield (90%) of the compound, while, raw palygorskite, kaolinite, and zeolite 4A have no effect on the rearrangement of chalcone epoxyde.

Although the properties of acid activated palygorskite have been studied from different points of view, no attempt has been made to study the charge characteristics and especially the point of zero charge (PZC) and the acidic surface constant (pK_a). The determination of the PZC based on potentiometric titrations or by mass titration has been the subject of many studies on oxide minerals as well as on layer clay minerals [8–13]. However, similar studies for fibrous clay are missing. The PZC of palygorskite and sepiolite was evaluated, until now, only by electrophoretic mobility measurements in dilute suspensions in order to determine the isoelectric point [14, 15].

In this study, we determined the acid–base properties on a series of acid activated palygorskite samples. The total surface sites and the surface site density were calculated from Gran plots [16]. The acidic surface constants were estimated with three surface protonation models at a specific ionic strength. The point of zero charge was evaluated using the common crossing point of *Z* vs. pH curves performed at different ionic strengths. The effect of the activation period on the acid–basic properties of palygorskite was investigated.

MATERIAL AND METHODS

Red palygorskite from south Tunisia was used as the starting material. The crude sample contained impurities: mainly dolomite (8% as measured by calcimetry)

[1] The text was submitted by the authors in English.

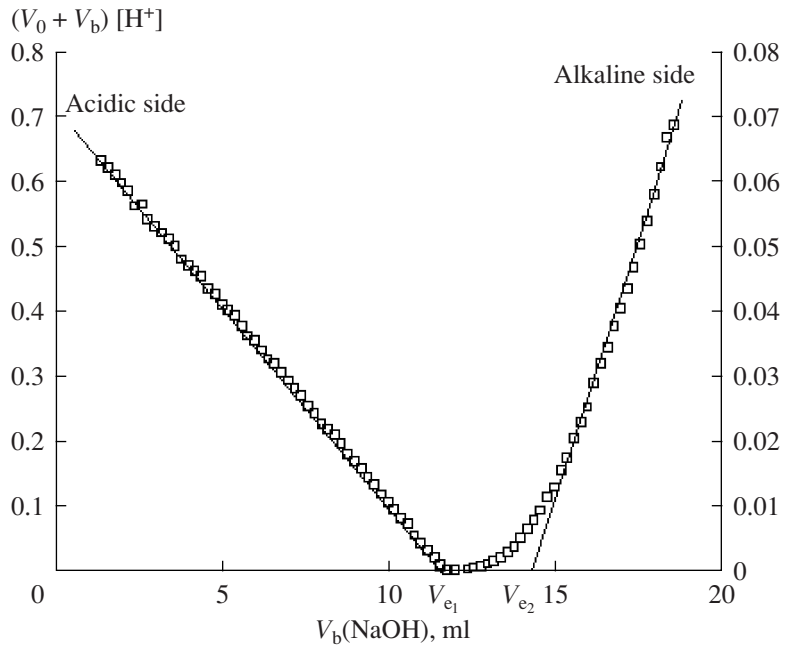

Fig. 1. Gran plot of a Paly2M25h suspension in 0.1 M NaCl.

and less than 5% quartz. The crude palygorskite was first treated with a diluted HCl solution in order to remove the carbonate. Then, it was washed with distilled water by centrifugation and dialysis to remove the excess chloride. After sedimentation, the purified fraction was dried and ground. The average size of the grains is <60 μm. Referring to the ASTM file (reference code 21-0957), Tunisian palygorskite has a monoclinic structure (Fig. 2). The chemical composition of the purified sample is as follows: SiO_2 53.5%, Al_2O_3 11.98%, MgO 12.05%, Fe_2O_3 5.9%, K_2O 0.72%, Na_2O 0.03%, CaO 0.09%, LOI 16% of the lost weight. Its structural formula calculated according to [17] is as follows: $(Si_{7.324}Al_{0.676})(Mg_{2.459}Al_{1.257}Fe_{0.608})(K_{0.125}Na_{0.008}Ca_{0.013})O_{20}(OH)_2(H_2O)_4 \cdot 4H_2O$. The cation exchange capacity (CEC) carried out by the Kjeldahl method is 23 meq/100 g, and its specific surface area is 59.7 m^2/g.

The purified palygorskite sample was subjected to acid treatment with 2 M hydrochloric acid using a solid/liquid ratio of 10/100 (w/w) at boiling temperature under reflux for different periods. The resulting solids were washed with distilled water until chloride free and the pH was constant.

The activated and raw palygorskite were characterised by X-ray diffraction (Pan analytical X'Pert High Score Plus diffractometer equipped with a Cu anticathode), chemical analysis [18], and by their specific surface area (Micrometric Autosorb 2050 Analyser) from the nitrogen adsorption isotherms at 77 K by the BET method and after degassing the samples at 150°C with a residual pressure of 10^{-5} mm Hg.

The acid–base properties of the palygorskite suspensions were determined using potentiometric titration. Measurements were performed with a microburette containing the titrant (NaOH 5.13×10^{-2} M) and an HI 9321 microprocessor pH meter (HANNA Instruments) with a combination electrode calibrated with two commercial pH buffers at ambient temperature and in an aerated medium.

For all the acid–base titrations, 0.1 g palygorskite was added to a 15 ml water flask and stirred for 24 h in order to attain equilibrium. The palygorskite suspensions were firstly acidified using HCl 10^{-2} M at pH 2 and then titrated with hydroxide solution to an alkaline pH (pH = 11). An NaCl solution was used to stabilize the system at a fixed ionic strength. Distilled water was added to bring the total initial volume of the suspension to 50 ml. The temperature was held constant at 25 ± 0.5°C. Afterwards, 5.13×10^{-2} M NaOH in 0.2 ml increments was used to titrate the suspension up to a pH of approximately 11. The equilibrium criterion for each addition of the titrant was the stability of the pH value measured. The NaCl electrolyte concentration was adjusted to 0.1, 0.01, and 0.001 mol/l. Before each potentiometric titration, the aqueous suspensions were equilibrated for about 10 min to each equilibrium pH value.

THEORETICAL BACKGROUND

For each studied system, Gran plots for the hydroxide titration were made from the experimental data and the two equivalence points V_{e_1} and V_{e_2} were determined by linear regression as shown in Fig. 1. The V_{e_1} values obtained in the acidic region are used to calcu-

late the amount of total protons added to the system. In fact, before the V_{e_1} point, the added NaOH reacted with the excess of HCl initially put in the system, so we can consider the V_{e_1} point as the zero titration point of the palygorskite surface. Therefore, for each titration point, the concentration of the total protons added is determined by

$$H_{TOT} = \frac{-(V_b - V_{e_1})C_b}{(V_0 + V_b)} \text{ mol/l}, \quad (1)$$

where V_b is the volume of NaOH added, V_0 is the initial volume of the system, and C_b is the concentration of NaOH.

The total surface sites per solid weight (Hs) calculated from the two equivalence points in the Gran plot V_{e_1} and V_{e_2} and the average number of protons reacted per surface site (Z) were defined by the following formula:

$$H_s = \frac{(V_{e_2} - V_{e_1})C_b}{m_s} \text{ mol/g}, \quad (2)$$

$$Z = \frac{(H_{TOT} - 10^{-pH} + 10^{(pH - pK_w)}) \times (V_0 + V_b)}{H_s \times m_s}, \quad (3)$$

where m_s is the solid weight used in the titration system.

The surface acidic constants were determined graphically. Three surface protonation models were considered in this study. The one site one pK_a model (model I), the two sites two pK_a model (model II), and the one site two pK_a model (model III).

Models I and II

For models I and II, we assume that the amphoteric surface hydroxyl groups (≡SOH) only release protons to form negatively charged surface sites (≡SO⁻) as shown in the following equation:

$$\equiv SOH \rightleftharpoons \equiv SO^- + H^+ \quad K_a$$

$$K_a = \frac{[\equiv SO^-][H^+]}{[\equiv SOH]} \text{ and from this } pH = pK_a + \log\frac{[\equiv SO^-]}{[\equiv SOH]}.$$

If we consider the dissociation coefficient of (≡SOH) (α) and the electrostatic effects, the pH formula becomes

$$pH = pK_a + n\log\frac{\alpha}{1-\alpha}, \quad (4)$$

where n is the Henderson–Hasselbach empiric constant and α is expressed by $\alpha = [\equiv SO^-]/([\equiv SOH] + [\equiv SO^-])$. To determine the ≡SO⁻ concentration, we considered the charge balance equation and the Gran plot data:

$$[H^+] + [Na^+] = [Cl^-] + [OH^-] + [\equiv SO^-]$$

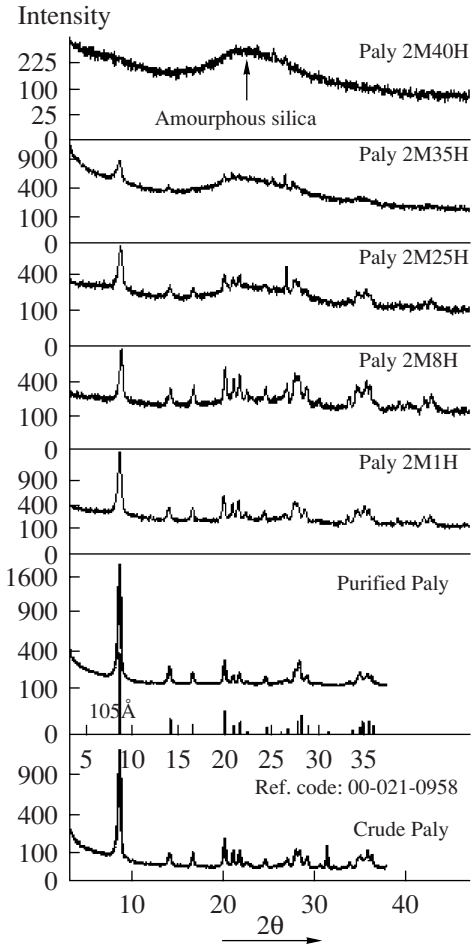

Fig. 2. XRD diffractograms of treated and untreated palygorskite.

$$[Na^+] = \frac{C_b V_b}{(V_0 + V_b)} \text{ and } [Cl^-] = \frac{C_b V_{e_1}}{(V_0 + V_b)}.$$

$$\text{Hence, } [\equiv SO^-] = \frac{(V_b - V_{e_1})C_b}{(V_0 + V_b)} + [H^+] - [OH^-]. \quad (5)$$

By substituting Eq. (1) into Eq. (6), [≡SO⁻] can be expressed by

$$[\equiv SO^-] = -H_{TOT} + 10^{-pH} - 10^{(pH - pK_w)}. \quad (6)$$

By using the Z formula (Eq. [3]), the ≡SO⁻ concentration can be rewritten as follows:

$$[\equiv SO^-] = -\frac{Z \times H_s \times m_s}{(V_0 + V_b)}. \quad (7)$$

The determination of the total surface sites ([≡SO⁻] + [≡SOH]) differs from the surface protonation model.

For the one site-one pK_a model, we assume that the amphoteric surface hydroxyl groups (≡SOH) are homogeneous:

$$[\equiv SOH] + [\equiv SO^-] = -\frac{H_s \times m_s}{(V_0 + V_b)} \quad (8)$$

$$\longrightarrow \alpha = \frac{[\equiv SO^-] \times (V_0 + V_b)}{H_s \times m_s} \quad (9)$$

and, by substituting Eq. (7) into Eq. (9), we obtain

$$\alpha = -Z. \quad (10)$$

For the two sites two pK_as model, we assume the existence of two types of sites: (a) weak acidic sites with a concentration of sites $[W_a]$ that dissociate at pH < 7, and (b) weak basic sites with a $[W_b]$ site concentration that dissociate at pH > 7:

$$\equiv S_I OH \rightleftharpoons \equiv S_I O^- + H^+ \quad K_{a1};$$

$$\equiv S_{II} OH \rightleftharpoons \equiv S_{II} O^- + H^+ \quad K_{a2}.$$

Moreover, when the interface between the clay mineral and water has different acidic sites, the successive dissociation of these sites can be defined by their dissociation coefficients α_1 and α_2 corresponding to pK_{a1} and pK_{a2}, respectively:

$$\alpha_1 = \frac{[\equiv SO^-]}{[W_a]} \quad \alpha_2 = \frac{[\equiv SO^-] - [W_a]}{[W_b] + [W_a]},$$

where $[W_a]$ is the concentration of weakly acidic sites between pH 5–7 determined by

$$[W_a] = \frac{(V_e - V_{e_1})C_b}{(V_0 + V_b)}, \quad (11)$$

$[W_b]$ is the concentration of weakly basic sites at pH > 7 determined by

$$[W_b] = \frac{(V_{e_2} - V_e)C_b}{(V_0 + V_b)}, \quad (12)$$

and V_e is the equivalence point determined by the maximum of the differential curve $d\text{pH}/dV$. From Eqs. (7), (11), and (12), α_1 and α_2 can be calculated.

Finally, by extrapolating the linear regression pH vs. $\log\alpha/(1-\alpha)$ curve to zero $\log\alpha/(1-\alpha)$, we can estimate the pK_a value.

Model III

For model III, or the one site amphoteric surfaces model, the reasoning and assumptions will be different. An amphoteric site is bifunctional, it can serve both as an acidic and as a basic functional group. It can undergo protonation and deprotonation:

$$\equiv SOH + H^+ \rightleftharpoons \equiv SOH_2^+ \quad K_{a1};$$

$$\equiv SOH \rightleftharpoons \equiv SO^- + H^+ \quad K_{a2}.$$

The corresponding equilibrium constants are

$$K_{a1} = \frac{[\equiv SOH][H^+]}{[\equiv SOH_2^+]} \quad K_{a2} = \frac{[\equiv SO^-][H^+]}{[\equiv SOH]}.$$

The mass balance on the surface sites can be written as

$$[\equiv SOH]_{TOT} = [\equiv SOH] + [\equiv SO^-] + [\equiv SOH_2^+]. \quad (13)$$

The charge balance equation is

$$[H^+] + [Na^+] + [\equiv SOH_2^+] = [Cl^-] + [OH^-] + [\equiv SO^-]. \quad (14)$$

The surface charge Q is defined by the difference between the positively and negatively charged sites

$$Q = [\equiv SOH_2^+] - [\equiv SO^-]$$

$$= [Cl^-] - [Na^+] + [OH^-] - [H^+]$$

$$Q = H_{TOT} + [OH^-] - [H^+]$$

$$Q = \frac{Z \times H_s \times m_s}{(V_0 + V_b)}. \quad (15)$$

At $\text{pH} \ll \text{pH}_{PZC}$, we can neglect the deprotonation (the solid surface is positively charged) and equation (13) becomes $[\equiv SOH]_{TOT} = [\equiv SOH] + [\equiv SOH_2^+]$ and $Q = [\equiv SOH_2^+]$.

On the other hand, when $[H^+]$ is very low (at $\text{pH} \gg \text{pH}_{PZC}$) the surface acquires a net negative charge and equation (13) becomes $[\equiv SOH]_{TOT} = [\equiv SOH] + [\equiv SO^-]$ and $Q = -[\equiv SO^-]$

Under these conditions, the K_{a1} and K_{a2} approximate to

$$K_{a1} = \frac{([\equiv SOH]_{TOT} - Q)[H^+]}{Q}$$

$$K_{a2} = -\frac{Q[H^+]}{[\equiv SOH]_{TOT} + Q}.$$

By using Eq. (8) and (15) we obtain

$$K_{a1} = \frac{(1-Z)[H^+]}{Z} \text{ and } K_{a2} = \frac{-Z[H^+]}{1+Z}.$$

From these equations,

$$\text{pH} = pK_{a1} + n\log\left(\frac{1-Z}{Z}\right),$$

$$\text{pH} = pK_{a2} - n\log\left(\frac{1+Z}{-Z}\right).$$

By extrapolating the linear regression curves of the pH versus $\log(1 - Z/Z)$ and versus $\log(1 + Z/-Z)$, we can estimated the pK_{a1} and pK_{a2} values:

Table 1. Chemical compositions of untreated and acid treated samples expressed in the oxide form/100 g of the calcined sample

Samples	SiO_2	Fe_2O_3	MgO	Al_2O_3
Paly	63.69	7.023	14.34	14.26
Paly2M1h	69.72	6.11	12.54	11.96
Paly2M8h	71.4	5.96	11.89	11.09
Paly2M25h	75.37	4.27	11.18	9.55
Paly2M35h	88.08	0.66	4.60	7.08
Paly2M40h	80.90	3.37	8.12	8.01
Paly2M50h	79.58	3.79	5.76	8.57

$$K_{a1}K_{a2} = \frac{[\equiv SO^-][H^+]^2}{[\equiv SOH_2^+]}$$

$$pH = \frac{pK_{a1} + pK_{a2}}{2} + \frac{n}{2}\log\frac{[\equiv SO^-]}{[\equiv SOH_2^+]}.$$

Near the pH_{PZC}, [≡SOH] is negligible in comparison with $[\equiv SO^-] + [\equiv SOH_2^+]$. From this approximation, we obtain

$$pH = \frac{pK_{a1} + pK_{a2}}{2} + \frac{n}{2}\log\frac{1 - Z}{1 + Z}. \quad (16)$$

RESULTS AND DISCUSSION

Acid Activation

The X-ray diffractograms of purified and acid treated samples are presented in Fig. 2. The untreated palygorskite has sharp strong reflexions at 10.5, 6.4, 5.4, 4.5, 3.68, and 3.23 Å. With increasing treating time, the crystallinity of the palygorskite decreased with the concomitant formation of an amorphous form. The latter can be observed by the appearance and increase of the broad bands at 16°–30° 2θ. After 35 h of treatment, only these bands are observed, indicating the complete destruction of the clay.

The acid treatment caused a progressive decrease of the octahedral cations (Al, Mg, and Fe) and a residual enrichment in SiO_2 (Table 1). At the beginning of the acid treatment, the decrease in the octahedral cations is limited, showing the resistance of the palygorskite structure and the difficulties of the opening of the channels. Once the H^+ access becomes easy throughout the structure, the dissolution becomes rapid and reaches its maximum at 35 h. For greater activation times, we note an increase in the octahedral cations, which can be attributed to coprecipitation.

The BET specific surface area gradually increases with the treating time up to 35 h (from 59.7 m^2/g to 437 m^2/g) decreasing thereafter (Table 2). Such behavior has been observed in the past [3, 19, 20]. The initial increase of S_{BET} is attributed to the opening of the structure channels following dissolution of the octahedral sheet and amorphous silica formation, whereas the decrease can be attributed to the condensation of the silanol groups [2]. This confirms that silica contributes to the total amount of the surface area. Moreover, activation increases the total pore volume from 0.3494 to 1.039 cm^3/g due to the development of mesoporosity.

Acid–Base Properties of Acid Treated and Untreated Palygorskite

Determination of the total surface sites. The average Hs values are listed in Table 2. The total surface sites of Tunisian palygorskite determined by the potentiometric method is 0.518 mmol/g, which is comparable to Brazilian palygorskite (0.476 mmol/g) determined by N-butylamine thermodesorption [21].

As expected, the Hs increases with the time of the acid activation to 1.53 mmol/g at 35 h, decreasing slightly thereafter.

The site density values (Ds) show that there is no correlation between the total surface sites (Hs) and the surface site area S_{BET} (Table 2).

Surface charge. To determine the surface charge of our samples versus the pH, we considered the average number of protons that reacted per surface site (Z) determined by equation (3).

Table 2. The surface area, the total surface site surface, the site density, and the point of zero charge of different palygorskite samples

Time, h	0	1	8	25	35	40	50
Hs, mmol/g	0.518	0.758	1.003	1.029	1.527	1.435	1.425
S_{BET}, m^2/g	59.7	127.5	161.6	307.2	437.0	325.3	138.3
Ds* (sites nm^{-2})	5.22	3.58	3.74	2.02	2.1	2.66	6.2
PZC	8.9	7.1	6.8	6.3	5.8	4.5	3.9

* $D_S = \frac{(H_S \times N_A)}{S_{BET} \times 10^{18}}$ (sites nm^{-2}), where N_A is Avogadro's number (6.02×10^{23} mol^{-1}), and S_{BET} is the palygorskite N_2/BET surface area expressed in m^2/g.

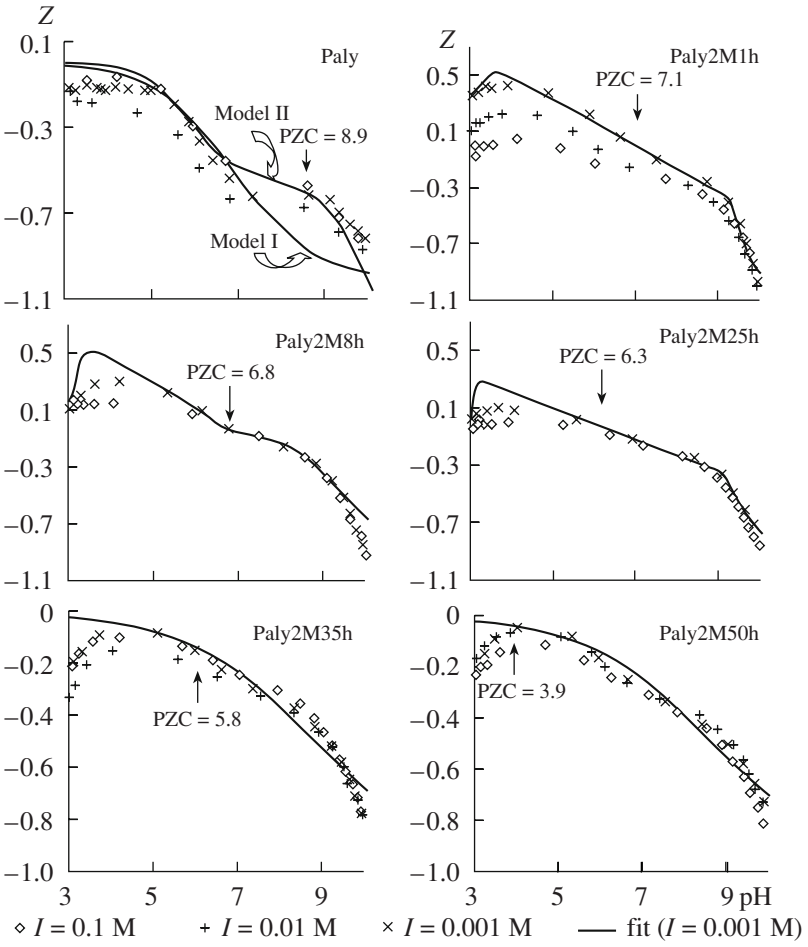

Fig. 3. Potentiometric titration curves for different palygorskite samples for each ionic strength. Fits of the experimental data to the models are shown for suspension samples in 0.001 M NaCl.

Figure 3 shows the evolution of the *Z* versus pH for the different samples. Acid activation modifies the shape of the curves as well as the sign of the surface charge. Moreover, the behavior of the *Z* vs. pH curves is not the same for all the treated samples. The potentiometric titration shows a negatively charged surface in all the pH range (3–11) for the untreated palygorskite and for the samples treated for longer times (Paly2M35h, Paly2M40h, and Paly2M50h). Such behavior is similar to that observed for illite [22] and for amorphous SiO_2 [23]. This means that, within the entire pH range, the deprotonation reaction is predominant. Furthermore, in the case of natural palygorskite, the *Z* plots reach a plateau at *Z* (pH, I) of approximately –0.65, which indicated that more than half of the total surface sites have released their protons. This suggests that the surface is heterogeneous and there are mainly two kinds of surface sites with different hydroxide affinities at the solid–water interface. This plateau is not pronounced for the treated palygorskite samples. When the palygorskite is moderately treated, its surface shows a different behavior. Depending on the pH, its surface can bear a net negative charge, a positive charge, or no charge. Therefore, the ≡SOH groups at external surfaces can be protonated and deprotonated under acidic and alkaline pH conditions, respectively. The acid activation produces new surface sites having different acid–base properties.

Determination of the zero charge (PZC). Curves of the *Z* versus pH at different NaCl concentrations were plotted for different samples. The curves have a common intersection point at the pH that is considered as the point of zero charge (PZC). As shown in Fig. 3 and Table 2, the PZC gradually decreases from about 8.8 in the starting material to about 3.9 in the most heavily treated sample (Paly2M50h). The amount of this shift depended on the acid treatment period. We can conclude that the acid treatment produces a shift of the PZC of the sample toward the PZC of amorphous silica (at about 2–3) [24]. This result is consistent with the fact that the Paly2M50h sample contained 80% amourphous silica and that no residual palygorskite is present.

Determination of the surface acidic constants. To explain the behavior of the surface hydroxyl groups, three surface protonation models were used. The choice

Table 3. pK_a values estimated with different surface protonation models

	pK_a			$pK_{a1} - pK_{a2}$			$pK_{a1} - pK_{a2} - (pK_{a1} + pK_{a2})/2$		
	Model I			Model II			Model III		
	0.1 M	0.01 M	10^{-3} M	0.1 M	0.01 M	10^{-3} M	0.1 M	0.01 M	10^{-3} M
Paly	6.68	6.47	6.85	5.26	5.46	5.89			
				10.13	10.64	10.05			
Paly2M1h							4.9	3.98	3.47
							9.28	9.29	9.42
							7.05 (6.88)	6.64 (6.05)	6.45 (7.00)
Paly2M8h							3.38		3.32
							9.32		9.49
							6.35 (6.70)		6.4 (6.59)
Paly2M25h								3.01	3.11
								9.51	9.37
								6.26 (6.90)	6.24 (5.87)
Paly2M35h	9.04	8.84	8.84						
Paly2M40h	9.18		9.30						
Paly2M50h	8.69	8.91	8.69						

Note: The $\frac{pK_{a1} + pK_{a2}}{2}$ values between the parentheses are obtained from Eq. by extrapolating the linear regression curves of the pH vs. $\log\left(\frac{1-Z}{1+Z}\right)$.

of the models is based on the surface charge results. Model I and II are applied when Z is always negative in the entire pH range. In both models, we considered that only the deprotonation reaction occurrs at the solid surface. Model III is used when the surface sites can undergo protonation and deprotonation. Thus, we tested model I and II for natural palygorskite. Model I was tested for Paly2M35h, Paly2M40h, and Paly2M50h and model III for Paly2M1h, Paly2M8h, and Paly2M25h.

We should note that, for all the previous calculations, a weakly acidic surface functional group (≡XH) accounting for the ion exchange reactions is neglected because palygorskite has a low cation exchange capacity. Moreover, the total number of structural-charge sites that are accessible for Na/H exchange reactions do not exceed 2% of the total CEC [25].

The pK_a values estimated with different surface protonation models are summarized in Table 3, and fits of the experimental data to the models are shown in Fig. 3. For the starting material, we obtained a pK_a value between 6.47–6.85 with the one site one pK_a model and pK_{a1} = 5.26–5.9 and pK_{a2} = 10.05–10.64, respectively, for the two surface acidic constants when we use the two sites two pK_a model. If we compare the pK_a values obtained from the two models, we clearly see that the pK_a in model I is comparable to the pK_{a1} in model II. Model I simplifies the heterogeneous palygorskite surface as a system with uniform acid–base properties and simulates the surface acid–base characteristics with the behavior of the stronger surface sites. However, model II gives a better description of the experimental data than model I. Unlike the natural palygorskite, model I is suitable for samples treated for a long time (more than 25 h). The pK_a values obtained from this model are 8.7–9.3. Application of model III for acid treated samples for a period of less than 35 h yielded two pK_a values: pK_{a1} in the range of 3–4 and pK_{a2} at about 9.5. If we compare these results with the pK_a values of silanol and aluminol groups found in the literature (Table 4),

Table 4. Surface dissociation constants for some aluminium and silica of kaolinite compounds found in the literature

	pK_{a1}	pK_{a2}	References
AlOH	2.9	9.84	[26]
SiOH	1.0	4.0	[27]
AlOH	7.9	9.1	[27]
SiOH	2.4	6.5	[28]
AlOH-Basal	3.4	8.4	[29]
AlOH-edges	6.5	8.5	[29]
SiOH		8.23	[30]
AlOH-edges	2.33	5.28	[30]

we can conclude that, in the natural palygorskite, there are two kinds of surface sites: aluminol ($pK_a \approx 5$) and silanol sites ($pK_a \approx 10$). The acid treatment progress disrupts the 2 : 1 structure and produces incomplete tetrahedra and octahedra at the edges. Opening of channels allows the H^+ access to the acidic basal AlOH sites ($pK_a \approx 3.4$) stronger than the edges AlOH sites ($pK_a \approx 6.5$). Beyond 25 h of acid treatment, acid activated palygorskite behaves as amorphous silica ($pK_a \approx 9$).

CONCLUSIONS

The potentiometric titration showed that the acid treatment produced an increase in the total surface site number, a shift of the PZC of the sample toward the PZC of amorphous silica depending on the acid treatment period, and changes of the surface charge properties. Thus, the modification of palygorskite by acid activation creates new active sites and increases its catalytic properties (such as its activity, selectivity, and thermal stability) and adsorption capacity.

Application of the three surface protonation models leads to reasonable descriptions of the surface properties and their evolution with the acid treatment.

REFERENCES

1. Gonzalez, F., Pesquera, C., Blanco, C., Benito, I., Mendioroz, S., and Pajares, J.A., Structural and Textural Evolution of Al- and Mg-Rich Palygorskites, I. Under Acid Treatment, *Applied Clay Science*, 1989a, vol. 4, pp. 373–388.
2. Gonzalez, F., Pesquera, C., and Benito, I., Mechanism of Acid Activation of Magnesic Palygorskite, *Clays and Clay Minerals*, 1989b, vol. 37, no. 3, pp. 258–262.
3. Myriam, M., Suarez, M., and Martin-Pozas, J.M., Structural and Textural Modifications of Palygorskite and Sepiolite under Acid Treatment, *Clays and Clay Minerals*, 1998, vol. 46, no. 3, pp. 225–231.
4. Corma, A., Mifsud, A., and Sanz, E., Kinetics of the Acid Leaching of Palygorskite Influence of the Octahedral Sheet Compositions, *Clay Miner.*, 1990, vol. 25, pp. 197–205.
5. Araujo Melo, D.M., Ruiz, J.A.C., Melo, M.A.F., Sobrinho, E.V., and Schmall, M., Preparation and Characterization of Terbium Palygorskite Clay as Acid Catalyst, *Microporous and Mesoporous Materials*, 2000, vol. 38, pp. 345–349.
6. Araujo Melo, D.M., Ruiz, J.A.C., Melo, M.A.F., Sobrinho, E.V., and Martinelli, A.E., Preparation and Characterization of Lanthanum Palygorskite Clays as Acid Catalysts, *J. Alloys and Compounds*, 2002, vol. 344, pp. 352–355.
7. Joy, B., Ghosh, S., Padmaja, P., and Lalithambika, M., A Facile 1,2 Proton Migration of Chalcone Epoxyde Using Acid Activated Palygorskites, *Catralysis Communications*, 2005, vol. 6, pp. 573–577.
8. Noh, S.J. and James Schwartz, A., Estimation of the Point of Zero Charge of Simple Oxides by Mass Titration, *J. Colloid and Interface Sci.*, 1989, vol. 130, pp. 157–164.
9. Hayes, K.F., Redden, G., Ela, W., and Leckie, J.O., Surface Complexation Models: An Evaluation of Model Parameter Estimation Using FITEQL and Oxide Mineral Titration Data, *J. Colloid Interface Sci.*, 1991, vol. 142, no. 2, pp. 448–469.
10. Zhuang, J. and Yu, G.R., Effects of Surface Coatings on Electrochemical Properties and Contaminant Sorption of Clay Minerals, *Chemosphere*, 2002, vol. 49, pp. 619–628.
11. Schroth, B.K. and Sposito, G., Surface Charge Properties of Kaolinite, *Clays and Clay Minerals*, 1997, vol. 45, no. 1, pp. 85–91.
12. Avena, M. and de Pauli, C.P., Proton Adsorption and Electrokinetics of an Argentinean Montmorillonite, *J. Colloid and Interface Sci.*, 1998, vol. 202, pp. 195–205.
13. Kriaa, A., Hamdi, N., and Srasra, E., Determination of Point of Zero Charge of Tunisian Kaolinites by Potentiometric and Mass Titration Methods, *Analytical Chemistry: An Indian Journal*, 2005, vol. 2, issue 1.
14. Neeman, A. and Singer, A., Rheological Properties of Aqueous Suspension of Palygorskite, *Soil. Sci. Soc. Am. J.*, 2000, vol. 64, pp. 427–436.
15. Alkan, M., Demirbas, O., and Dogan, M., Electrokinetic Properties of Sepiolite Suspensions in Different Electrolyte Media, *J. Colloid Interface Sci.*, 2005, vol. 281, pp. 240–248.
16. Gran, G., Determination of the Equivalence Point in Potentiometric Titration. Part II, *Analyst*, 1952, vol. 77, p. 661.
17. Bailey, S.W., *Structures of Layer Silicates: In Cristal Structures of Clay Minerals and Their X-ray Identification*, Brindley, G.W. and Brown G., Eds. (Mineralogical Society, London, 1980), pp. 2–123.
18. Solgic, Z. and Marjanovic-Krajovan, Y., Méthode Rapide d'Analyse de SiO_2, Fe_2O_3, Al_2O_3, TiO_2, CaO et MgO Dans une Bauxite: Analyse Rapide de Calcaire et de Dolomite, *Chimie Analytique*, 1968, vol. 50, pp. 122–127.
19. Vicente, M.A., Lopez-Gonzalez, J.D., and Banares M.A., Acid Activation of a Spanish Sepiolite: Physicochemical Characterization, Free Silica Content and Surface Area of Products Obtained, *Clay Miner.*, 1994, vol. 29, pp. 361–367.

20. Suarez, M., Flores, L.V., Vicente M.A., and Martin-Pozas, J.M., Acid Activation of Palygorskite with HCl: Development of Physico–Chemical, Textural and Surface Properties, *Applied Clay Sci.*, 1995, vol. 10, pp. 247–258.
21. Ruiz, J.A.C., Melo, D.M.A., Souza, J.R., and Alcazar, L.O., Determination of Total Acid in Palygorskite Chemically Modified by n-Butylamine Thermodesorption, *Material Research*, 2002, vol. 5, pp. 173–178.
22. Du, Q., Sun, Z., Forsling, W., and Tang, H., Acid-Base Properties of Aqueous Illite Surfaces, *J. Colloid Interface Sci.*, 1997, vol. 187, pp. 221–231.
23. Dove, P.M. and Craven, C.M., Surface Charge Density on Silica in Alkali Alkaline Earth Chloride Electrolyte Solutions, *Geochim. Cosmochim. Acta,* 2005, vol. 69, no. 21, pp. 4963–4970.
24. Sverjensky, D.A., Prediction of Surface Charge on Oxides in Salt Solutions: Revisions for 1 : 1 (M^+L^-) Electrolytes, *Geochim. Cosmochim. Acta*, 2005, vol. 69, no. 2, pp. 225–257.
25. Wanner, H., Albinsson, Y., Karnland, O., Wieland, E., Wersin, P., and Charlet, L., The Acid/Base Chemistry of Montmorillonite, *Radiochimica Acta*, 1994, vols. 66/67, pp. 157–162.
26. Schindler, P.W., Liechti, P., and Westall, J.C., Adsorption of Copper Cadmium and Lead from Aqueous Solution to the Kaolinite/Water Interface, Nethelands, J.C., *J. Agric. Sci.*, 1987, vol. 35, p. 219.
27. Carrol-Webb, S.A. and Walther, J.V., A Surface Complex Reaction Model for the pH-Dependence of Corundum and Kaolinite Dissolution Rates, *Geochim. Cosmochim. Acta*, 1988, vol. 52, p. 2609.
28. Motta, M.M. and Mizanda, C.F., Molibdate Adsorption of Kaolinite, Montmorillonite, and Illite: Constant Capacitance Modelling, *Soil Sci. Soc. Amer. J.*, 1998, vol. 53, p. 380.
29. Wieland, E. and Stumm, W., Dissolution Kinetics of Kaolinite in Aqueous Solutions at 25°C, *Geochim. Cosmochim. Acta*, 1992, vol. 56, p. 3339.
30. Brady, P.V., Cygan, R.T., and Nagy, K.Z., Molecular Controls on Kaolinite Surface Charge, *J. Colloid. Interface Sci*., 1996, vol. 183, p. 356.

ISSN 1068-3755, Surface Engineering and Applied Electrochemistry, 2008, Vol. 44, No. 5, pp. 410–414. © Allerton Press, Inc., 2008.
Original Russian Text © M.K. Bologa, E.G. Sprinchan, Al.M. Bologa, 2008, published in Elektronnaya Obrabotka Materialov, 2008, No. 5, pp. 79–84.

ELECTRICAL TREATMENT OF BIOLOGICAL OBJECTS AND FOODSTUFFS

Recovery of Lactulose Products and Protein–Mineral Concentrate

M. K. Bologa, E. G. Sprinchan, and Al. M. Bologa

Institute of Applied Physics, Academy of Sciences of Moldova, ul. Academiei 5, Chisinau, MD-2028 Republic of Moldova
E-mail: mbologa@phys.asm.md

Received March 13, 2008

Abstract—The necessity of milk whey treatment was substantiated taking into account the ecological situation and the vitality of preparation of protein–mineral concentrate (PMC) and lactulose-containing products. The electrophysical method of PMC preparation was examined and used. The protein fractions, particularly, their amino acid composition and digestion by proteolytic enzimes (characteristic of the pepsin-pancreatic index); the products of peroxide lipid oxidation; and the composition of nitrogen-containing compounds were investigated. The investigation results and the ways to optimize the proposed combined method of processing of lactose-containing raw material with a high lactulose content with a simultaneous decrease in the energy consumption were presented.

DOI: 10.3103/S1068375508050128

The problem of methods that guarantee healthy and well-balanced nutrition and the ways of their solution are attracting growing attention worldwide. Quality improvements of foodstuffs and elaboration of new technologies, including the rational and wasteless consumption of secondary resources, are attracting the growing attention of researchers. In these circumstances, a purposeful change of the characteristics, quality, and productivity becomes the general rule.

In particular, probiotics (live cultures of bifidobacteria and lactobacilli) and prebiotics (bioactive dietary fibers that stimulate the growth and activity of bifidobacteria) entering the human organism with foodstuffs compensate for the deficiency of useful bacteria and help to maintain the bacterial equilibrium [1]. Lactulosa, a product of the advanced processing of dairy products, is one of the most widespread and recognized prebiotics. In its natural form, it is present only in human milk; in all other cases, lactose is the main carbohydrate, which, in turn, almost completely passes into the whey during processing. The traditional methods of preparing lactulosa from milk sugar (lactose is its nearest isomer) are the most efficient. The biochemical properties of lactulose are rather well studied. Mainly lactic acid and, to a lesser degree, acetic and formic acids, as well as ethanol, are the end products of lactulose metabolism [2].

Two ways of lactose isomerization into lactulose are known. The first one is related to the reaction of transformation of aldoses into ketoses (the Lobry–de Bruyn–van Alberda–van Ekenstein reaction, or L–A transformation) with the formation of intermediate enol forms of lactose and epilactose in base solutions. Alkaline reagents are usually used as catalysts in this reaction. The second isomerization way is the Amadori rearrangement, which follows with formation and hydrolysis of lactulosilamine. Under the action of catalysts (acids or bases), lactose interacts with ammonia and aromatic or aliphatic amines with lactosamine formation, which is then subjected to rearrangement. For industrial production of lacto-lactulose syrups, the method is generally used that is based on the lactose intramolecular rearrangement in alkaline media according to L–A transformation [3].

Two properties of lactulose make it a unique remedy for eliminating dysbacteriosis. Lactulose is a strong specific stimulator of the vital activity of bifidobacteria, promoting their fast reproduction, and it can reach the places where bifidobacteria are situated, since the human organism does not contain enzymes able to decompose lactulose [4].

More than 60 medical preparations are known that were developed on the basis of lactulose where the lactoluse property is used as a powerful bifido factor, which is an effective remedy to restore the normal gut microflora and eliminate toxic ammonia. Lactose isomerization into lactulose with electroactivation of its solutions is considered to be a promising method [5].

Investigations of the electrolysis of various aqueous systems in a diaphragm electrolyser have revealed the phenomenon of polarization energy conservation of the electrode, which considerably changes the reactivity of the medium. This phenomenon is called the electrochemical activation of liquid media [6]. Its main point

is that it is possible to substantially change the rate and selectivity of chemical reactions, mainly in liquids and gases subjected to preliminary electrochemical action in the zone of one of the polarized inert electrodes.

It was shown experimentally that, after the activation action is stopped, the substance (for a definite time period) usually resides in a metastable state, which can be retained for a long time if energy exchange with the ambient medium is absent. The electroactivated liquid medium in some cases changes not only the rate of chemical reactions but their direction as well. The electroactivated medium in its metastable state is a nonequilibrium system and retains its abnormal properties during the slow relaxation to the state of stable thermodynamic equilibrium.

The electrochemical activation is technically performed by the action on an aqueous solution in the polarized electrode zone, for example, of a diaphragm electrolyser. However, unlike electrolysis and electrodialysis, the electrochemical activation is not an end chemical process; it is intended to regulate the reactivity of the physicochemical properties of liquids in technological processes with the aim to optimize them and to improve their efficiency.

The treatment of the liquid at electroactivation is usually performed in the zone of the main electrode, while, in the zone of the electrode with opposite polarity (the auxiliary electrode), the minimal possible flow of the activated liquid (0.1–1% of the flow in the zone of the main electrode) is sustained or the zone is filled with a special buffer liquid that neutralizes the reaction products near the auxiliary electrode [7].

Under the action of the electrochemical processes near the electrodes, the composition and properties of the solutions change. As a result, near the cathode, an alkaline medium (catholyt) forms and, near the anode, an acid medium (anolyt) forms. Decomposition of water and dissociative substances (salts) is the basis of the electrochemical reactions. The hydroxide ions that form in the catholyt perform as proton acceptors in the reaction of the lactose isomerization. The excessive internal potential energy of the activated solution intensifies the reaction of transformation of lactose into lactulose. Lactose is the best but an expensive raw material for lactulose production. Application of milk whey that contains 4.0–4.7% milk sugar (lactose) is much more cost effective. Whey is most promising as a solution for electroactivation, since it contains a relatively high quantity of mineral substances and possesses the necessary properties for fast and effective accumulation of active charged particles when an electric current passes through it. The data are known to be related to the reagentless isomerization process performed in the curd whey by the electroactivation method. The whey was placed in the cathode cell, and tap water was placed in the anode cell. The industrial methods of lactulose preparation are based on alkaline lactose isomerization [8].

Moreover, it is known that protein fractions are not present in the whey in the form of real protein solutions, since, in the primary technological processes (curd and cheese production), a partial hydrolysis of protein molecules into amino acids occurs. To produce the primary products, various microorganism cultures are used, which are also protein substances by their nature. The whey needs proper processing. It is important to mention that the biological and chemical oxygen demands (BOD and COD) of whey are high and directly lead to the loss of flora and fauna in the environment [9].

Whey refers to a group of relatively cheap lactose-containing raw materials that meets the demands for production of both lactulose and valuable bifidogenic additives. The authors propose a method for the recovery of the lactose product with the simultaneous production of a protein–mineral concentrate. With this aim, the electroactivation of milk whey in a flow diaphragm electrolyser was used with the subsequent concentrate separation in the field of the mass forces [10].

The main parameters that control the process are as follows: the electric current density, the composition of the anodic solution, the rate of the liquid supply to the cells, and the diaphragm type. The combination of these factors determines the rate of the increase in the temperature and the active acidity in the cathode cell, as well as the diaphragm state and the electric voltage, and influences the quantity and composition of the recovered concentrate. The determined regimes allow one to decrease the protein content in the whey by 60–65% and that of calcium ions and phosphor-containing ions by 94–96%. Not less than 90% of the carbohydrates and almost all the potassium and sodium ions remain in the produced raw material [11].

The calcium–phosphate salts that are contained in the concentrate composition, along with proteins, determine its biological value. The electrophoresis data in a polyacrylamide gel confirm the presence of all the fractions that were present in the initial milk whey (IW). The amino acid analysis of the proteins confirms the presence of the main essential amino acids (Table 1).

The obtained concentrate does not contain the products of peroxide lipid oxidation (first of all, malonic aldehyde), which determine the carcinogenic properties of the product (Table 3). The presence of such nitrogen compounds as creatine, creatinine, urea, etc., in the processed whey can be a prerequisite, along with the residual protein, to increase the external bifidogenity of the subsequently isomerized lactulose end product (Table 4).

The electrophoresis results in a polyacrylamide gel confirm the presence of the all protein fractions in the concentrate that are present in the initial milk whey,

Table 1. Amino acid composition of the IW and PMC (in percent of the total amino acid content)

No.	Amino acids	IW pH 4.65	PMC pH 7.3	PMC pH 8.8	PMC pH 9.05	PMC sum
1	Asparagine	12.70	11.10	10.60	10.27	4.14
2	Serine	5.99	8.10	7.80	8.13	2.98
3	Glutamine	19.14	22.58	21.98	23.38	76.29
4	Proline	5.21	4.86	4.68	4.52	2.15
5	Glycine	1.85	1.95	1.89	1.65	0.65
6	Alanine	3.04	5.19	5.19	4.94	1.65
7	Histidine	3.41	2.05	1.99	2.01	0.49
8	Arginine	2.75	3.16	3.50	3.20	0.55
9	Threonine	4.97	5.03	4.88	4.77	2.15
10	Valine	2.75	3.52	3.41	3.19	0.94
11	Isoleucine	3.13	3.09	2.98	3.01	0.75
12	Leucine	11.96	10.69	10.86	11.33	3.01
13	Tyrosine	2.82	2.95	3.14	2.64	0.64
14	Phenylalanine	3.98	4.71	4.42	4.36	0.73
15	Lysine	8.94	7.36	8.21	8.35	1.84

Table 2. Comparative characteristics of the pepsin–pancreatic index

Foodstuff proteins	Pepsin-pancreatic index (PPI)
PMC	58
IW	79
Caseine	73*, 68*, 78*
Milk	90*, 84*
Gluten	40*, 84*
Gelatine	25*

* Source—[12, 13].

whose composition exceeds many proteins of animal and vegetal origin by the content of essential amino acids.

The whey proteins possess the greatest rate of decomposition among the whole proteins. The pepsin–pancreatic index (58) determined in vitro under the action of proteolytic enzimes (pepsin, trypsin, and chymotrypsin) confirms the high nutritive value of the protein component of the concentrate (Table 2).

The lactose isomerization into lactulose in this case amounts to 30–35%.

The method optimization was performed in several directions. First, the diaphragm type was varied (the usual canvas dam was changed to an ion-exchange MK-40 dia-

Table 3. Characteristics of the peroxide lipid oxidation

Sample characteristics	Lipids (%)	Diene and triene conjugates (opt. dens. unit)	Malonic dialdehyde (nmol/100mg)
Initial whey	20.96	0.754–0.129	15.67 ± 0.81
Protein–mineral concentrate	3.11	0.588–0.011	15.44 ± 0.929

Table 4. Nitrogen-containing compound

No.	pH	Urea nitrogen (mmol/l)	Creatinine (mol/l)	Uric acid (mg/dl)
IW	4.65	1.733	423.1	1.049
1	5.65	3.096	493.5	1.514
2	6.50	2.105	473.1	1.497
3	7.05	1.141	242.6	0.214
4	8.05	0.960	227.5	0.074
5	10.00	1.021	359.3	1.025
6	11.00	0.556	397.3	0.343
7	11.30	0.260	213.2	0.008
8	11.45	0.370	376.1	0.090
9	11.50	0.150	356.4	0.081
10	11.60	0.130	460.7	0.076
AC	2.90	0.650	346.2	0.136
CC	10.65	0.112	281.5	0.432

Note: **AC** and **CC** are the sum contents of the anode and cathode cells, respectively.

phragm). Second, the anodic liquid was simultaneously renewed. In this case, the voltage decreases approximately by a factor of two (Fig. 1) and the quantity of the recovered protein in the PMC increases to 70% (Fig. 2).

Moreover, a combined method of processing of the lactulose-containing raw materials was used that provided a lactulose percentage in the end product of up to 45–50% (Fig. 3) and diminished the energy costs.

Thus, the proposed reagentless and low-temperature method of the electrophysical recovery of the protein–mineral concentrate can be included in a wasteless cycle of milk whey utilization with the aim to produce

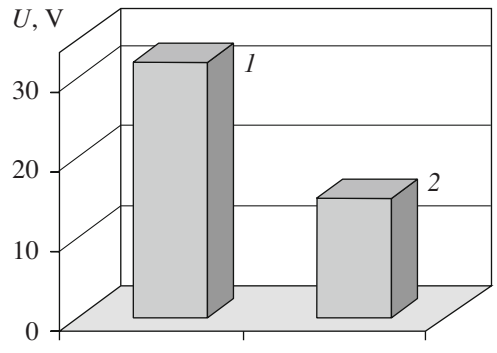

Fig. 1. Voltage dependence for various diaphragm types. (*1*) Canvas dam, (*2*) MK-40 ion-exchange diaphragm.

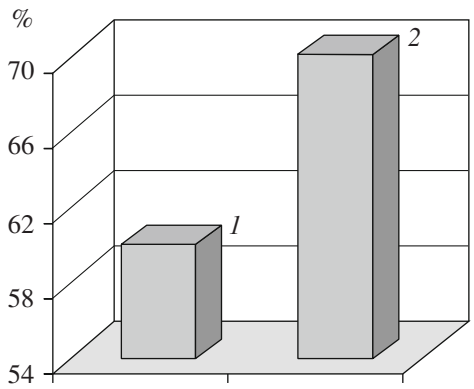

Fig. 2. Protein content in the protein–mineral concentrate. (*1*) Proposed method; (*2*) method with a selective calcium ion supply.

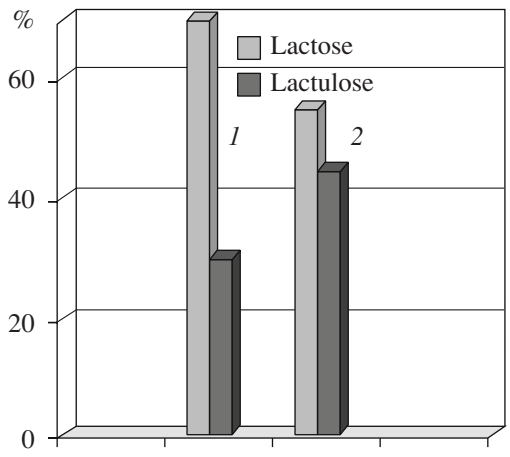

Fig. 3. Change in the lactose and lactulose content as dependent on the method. (*1*) Electroactivation; (*2*) combined method.

a protein–mineral concentrate and a lactulose-containing product.

REFERENCES

1. Khramtsov, A.G., Ryabtseva, S.A., and Polishchuk, D.O., Development of the Technology of Whole Dairy Products with Addition of Lactulose Concentrate. *Vestn. SevKavGTU, Ser. "Prodovol'stvie"*, 2003, no. 1(6).
2. Khramtsov, A.G., Evdokimov, I.A., Ryabtseva, S.A., Polovyanova, A.V., Kozlova, E.A., and Ereshova, V.D., Lactulose Application in the Milk Industry. *Sb. Nauchn. Tr. SevKavGTU, Ser. "Prodovol'stvie"*, 2005, no. 1.
3. Khramtsov, A.G., Sinel'nikov, B.M., Evdokimov, I.A., Ryabtseva, S.A., and Serov, A.V. Physicochemical Properties, Biological Value and Medical Application of Lactulose, *Vestn. SevKavGTU, Ser. "Prodovol'stvie"*, 2003, no. 1(6).
4. Khramtsov, A.G., Ryabtseva, S.A., and Zhurba, L.N., Isomerization Regularities of Lactose into Lactulose in a Cheese Whey, *Vestn. SevKavGTU, Ser. "Prodovol'stvie*, 2003, no.1(6).
5. Khramtsov, A.G., Brykalov, B.A., Ryabtseva, S.A., and Tkachenko, V.N., Investigation of Some Apects of Lactulose Marketing, *Vestn. SevKavGTU, Ser. "Prodovol'stvie"*, 2003, no. 1(6).
6. Bakhir, V.M., *Elektrokhimicheskaya aktivatsiya* (Electrochemical Activation), Moscow: VINIIIMT, 1992, part 2, 657 p.
7. Leonov, B.I., Prilutzkii, V.I., and Bakhir, V.M., *Fiziko-khimicheskie aspekty biologicheskogo deistviya elektrokhimicheski aktivirovannoi vody* (Physicochemical Aspects of Biological Action of Electrochemically Activated Water), Moscow: VNIIIMT, 1999.
8. Khramtsov, A.G., Ryabtseva, S.A., and Suyuncheva, B.O. Investigation of the Isomerization Process of Lactose into Lactulose at the Electroactivation of Milk Whey, *Vestn. SevKavGTU, Ser. "Prodovol'stvie"*, 2004, no. 1(7).
9. Sinel'nikov, B.M., Khramtsov, A.G., Evdokimov, I.A., Ryabtseva, S.A., and Serov, A.V., *Laktoza i ee proizvodnye* (Lactose and Its Derivatives), St.-Peterburg: Professiya, 2007.
10. Bologa, M.K., Sprinchan, E.G., and Maksimuk, E.P., Processing Method for the Secondary Milk Raw Material, Application submitted for Patent of the Republic of Moldova, 2008 0081. Registered 2008-03-20.
11. Sprinchan, E.G., Bologa M.K., Salt Composition of Protein-Whey Concentrate Prepared by an Electrocontact Method, *Elektron. Obrab. Mater.*, 2006, no. 6, pp. 57–65.
12. Pokrovskii, A.A., and Ertanov, I,D., Liability of Foodstaffs to the Action of Proteolytic Enzimes, *Vopr. Pitaniya*, 1986.
13. Sazhinov, G.Yu., Quality Evaluation of Foodstaffs for Children, *Pishchevaya Prom-st*., 2001, no. 4, pp. 31–32.

ISSN 1068-3755, Surface Engineering and Applied Electrochemistry, 2008, Vol. 44, No. 5, pp. 415–421. © Allerton Press, Inc., 2008.
Original Russian Text © K.M. Popovich, 2008, published in Elektronnaya Obrabotka Materialov, 2008, No. 5, pp. 85–92.

ELECTRICAL TREATMENT OF BIOLOGICAL OBJECTS AND FOODSTUFFS

The Influence of Natural Antioxidants on the Oxidative Stability of Iodine-Fortified Sunflower Oil in the Process of Storage

K. M. Popovich

Technical University of Moldova, 168 Stefan chel Mare's Boulevard, Kishinev, MD-2068, Republic of Moldavia
E-mail: cristina_popovici@mail.md

Received April 18, 2008

Abstract—The task of obtaining oils with heightened antioxidative properties by incorporating natural antioxidative spice plant components into the receipt composition has been solved in order to decrease the intensity of possible oxidative reactions and increase the shelf life of iodine-fortified sunflower oil. It has been shown that natural antioxidants exert an effective influence on the stabilization of the investigated oils; i.e., the intensity of accumulation of primary and secondary oil oxidation products is inhibited.

DOI: 10.3103/S106837550805013X

INTRODUCTION

The deficiency of iodine in food is one of the major problems of the world community, which is reflected in documents of the U.N.O. and in the governmental enactments of many countries [1–6].

About 13% of the world's population suffers from an iodine deficiency and 85% of the people living in the Republic of Moldavia are subject to the risk of development of iodine-deficient disorders (IDDs), as evidenced by the data of research conducted by specialists of UNICEF.

Taking into consideration that the creation of fortified foodstuffs is an urgent trend in eliminating the deficiency of iodine in food [11–17], we have developed technology for obtaining iodine-fortified sunflower oil and also investigated all its organoleptic and physicochemical indices.

To decrease the intensity of possible oxidative transformations and to increase the shelf life of the investigated oil, the task was posed to obtain iodine-fortified oil with increased antioxidant properties at the expense of incorporating into its composition natural antioxidants, namely, antioxidative spice plant components.

THE THEORETICAL ANALYSIS

Despite the fact that synthetic antioxidants are widely distributed in the world with the view of stabilizing vegetable oils, there are a number of works that testify to the inexpediency of their application [18, 19]. Taking into consideration the need for natural antioxidants, we have tried to use spice plants for this purpose.

The capability of antioxidants to hamper the oxidation process is determined by the fact that their composition includes weakly bound mobile hydrogen or functional groups that actively react with molecular oxygen or with free radicals that form in the oxidation process [20]. This condition is fulfilled in the case of phenols and aromatic amines [21, 22].

A new group of antioxidants that belong compositionally to aromatic diketones has recently been revealed [23]. The antioxidative action of this group of compounds is determined by the presence of a weekly bound hydrogen atom in the second position [24]. The literature lacks for data about the energy of the detachment of this hydrogen atom. Another requirement imposed on antioxidants is their high lipophility [25, 26].

The solubility of these components was investigated using the data of the literature with a view to determine the optimal conditions of their extraction (Table 1).

EXPERIMENTAL

The scheme shows the technological scheme for producing the iodine-fortified stabilized sunflower oil at the expense of spice plant extracts.

It was ascertained that the quantity of spice plants equal to 0.4–0.6 g/100 g is optimal for the iodine-fortified sunflower oil for achieving stable and minimal degrees of oxidation. Consequently, this concentration of the antioxidant permits the possible oxidative influence of iodine to be eliminated and allows the shelf life of the iodine-fortified sunflower oil to be prolonged.

The oxidative stability of the obtained iodine-fortified oils with spice plant extracts was investigated according to the value of the accumulation of primary and secondary oxidation products in the compared oil samples over 12 months at a temperature of 4–6°C.

The content of primary oxidation products was estimated using the peroxide values [28] and the quantity of hydroperoxides. Monohydroperoxides were

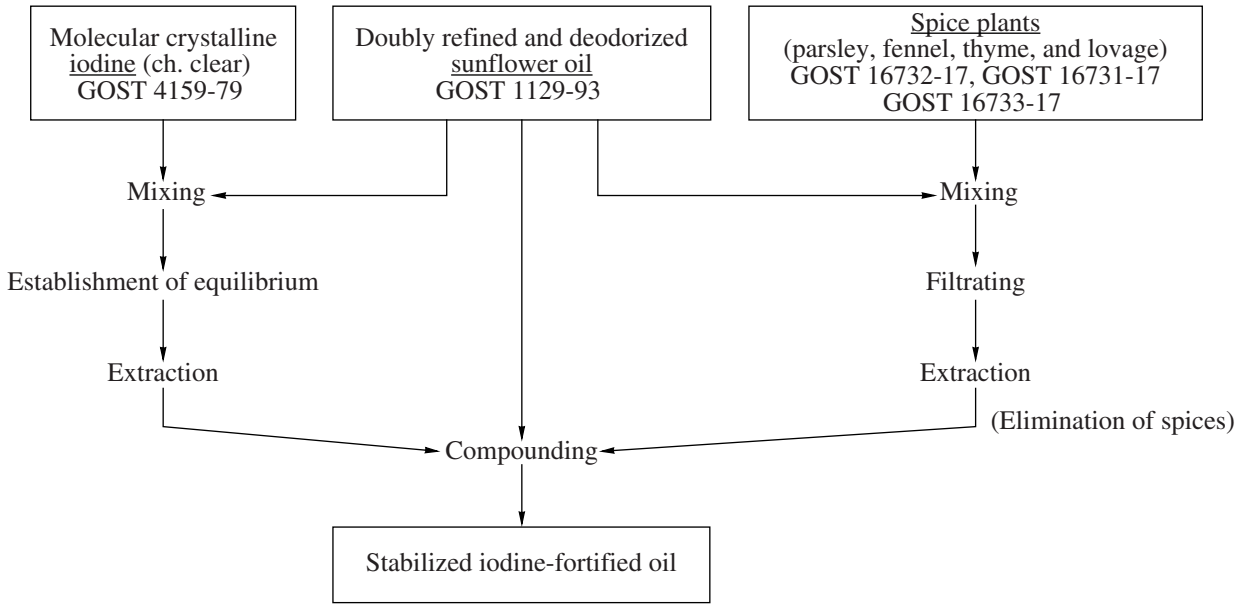

The scheme presents the main technological processes of producing stabilized iodine-fortified sunflower oil.

detected by a spectral method of analysis ($\lambda = 510$ nm) according to the procedure of Shanta and Decker [29].

The formation and intensity of the accumulation of the secondary oxidation products in the investigated oils were characterized by the *p*-anisidine [30] and tiobarbituric [31] values.

The reliability of the experimental data was estimated by methods of mathematical statistics with finding an average interval value from three parallel experiments at a confidence probability of 95% [32].

RESULTS AND DISCUSSION

Oxidative and hydrolytic decomposition is observed in the process of storing vegetable oils. The presence and depth of the process of oil oxidation and hydrolysis is characterized by the content of free fatty acids in oils, i.e., the acid value (AV).

The growth of the acid value or intensity in the formation of free fatty acids in the compared oils has a linear character (Fig. 1).

The presence of free fatty acids in fresh samples that did not undergo the storage process can be explained by the fact that fatty acids are normal intermediate metabolites of the adipose tissue.

The acid values of the sunflower oil samples without iodine and spice plant extracts and those of the oil samples with the iodine content of 1 μg I/ml do not essentially differ after 12 months of storage, averaging 0.316 mg KOH/g of oil. It should be noted that the acid value of these two investigated samples approached the limit of the admissible values (0.35 mg KOH/g of oil) stipulated by the GOST 1129-93 standard for sunflower oil.

Consequently, as has already been shown [33–35], molecular iodine incorporated into the composition of sunflower oil with the view of increasing its biological

Table 1. The solubility of antioxidative spice plant components

The name of the component	Solubility, g/100g		
	in water	in alcohol	in ethers
β-carotene	nonsoluble	easily soluble	easily soluble
Quercetin	0.006	0.029	1.419
Caffeic acid	soluble	easily soluble	easily soluble
Ferule acid	soluble	easily soluble	easily soluble
Terpenes:			
carvone	1.32	easily soluble	easily solubl
A-pinene	nonsoluble	easily soluble	easily soluble
Ascorbic acid	33.3	easily soluble	nonsoluble

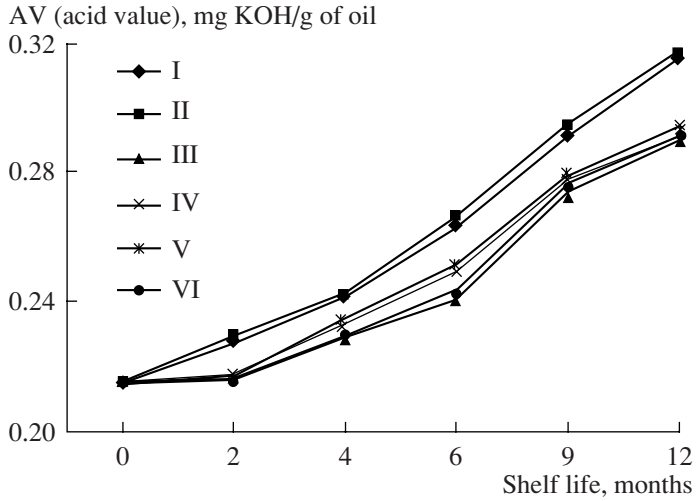

Fig. 1. The change in the AV of the compared oil samples in the course of storage. I—oil without iodine and spice plant extracts; II—oil with an iodine content (1 μg I/ml); and III, IV, V, and VI—oils with an iodine content (1 μg I/ml) and with spice plant extracts (parsley, fennel, thyme, and lovage, respectively).

value is fixed by the double bonds of oil fatty acids with the formation of stable π complexes.

The π-complexes formed between iodine and the double bonds of triglyceride fatty acids slow down the processes of oxidation and hydrolysis that take place in the investigated oils in the course of storage.

When comparing the acid values of the oil group with the iodine content of 1 μg I/ml and with the spice plant extracts, one can note that free fatty acids accumulate to a lesser extent in a sample containing a parsley extract as an antioxidative component and that the acid values are within the range of 0.215–0.291 mg KOH/g of oil. Meanwhile, the acid value of a sample with a fennel extract already amounted to 0.294 mg KOH/g of oil after 12 months of storage. This being the case, the acid value remained within the limits of the above-indicated GOST standard in all the samples investigated.

According to the theory of N.N. Semenov, the oxidation of oil must be considered as a chain reaction that develops through the formation and conversion of free radicals. The essence of the chain reaction mechanism is that chain reactions appear and develop through the formation and inactivation of free radicals. Free radicals are fatty acid molecules. One of the atoms of which has a free valence; therefore, they are chemically active and easily attach oxygen. Moreover, they attach oxygen to the place of the free valence of a radical with the formation of peroxides, rather than to the double bonds of fatty acids (as the theory of Bakh–Engler states). The formed free peroxide radical is subsequently a leading component in the oxidation chain, since all the remaining oxidation products are formed through it.

The presence and quantity of peroxides and hydroperoxides in vegetable oils are known to determine the level of the oil storage stability. Table 2 shows the dynamics of the accumulation of these compounds in the compared oil samples during storage.

As the presented data show, the summary rate of oxidative reactions that lead to the formation of peroxides and hydroperoxides in the course of storage for 12 months is lower for the group of stable oils with the iodine concentration of 1 μg I/ml and with extracts of spice plant components (it varies from 7.8 to 9.2 mEq/kg of oil for peroxides and from 0.071 to 0.116 mM for hydroperoxides) than in the initial oil (from 8.4 to 9.9 mEq/kg of oil for peroxides and from 0.079 to 0.128 mM for hydroperoxides).

When comparing the oil samples without and with the iodine content (1 μg I/ml), one should note that the degree of the accumulation of the primary oxidation products in these oils does not depend on the presence of iodine in the composition of the investigated oil or is within the same limits, varying from 8.4 mEq/kg of oil before storage to approximately 10.0 mEq/kg after 12 months of storage and from 0.079 to 0.128–0.129 mM for peroxides and hydroperoxides, respectively.

Figure 2 visually illustrates the intensity of the processes of the formation of the primary oxidation products (peroxides and hydroperoxides) in the investigated oils depending on the duration of storage.

The shelf life of the oil samples is plotted on the abscissa. The height of each column corresponds to the quantitative expression of the peroxide accumulation for a concrete sample at a given index of shelf life.

As one can note from Fig. 2, the dependence between the content of peroxides and the shelf life has an autoaccelerated character. The growth of the peroxide accumulation takes place at the first stage, and, at the second stage, the accumulation has a constant value. The duration of the first stage characterizes the persistence of the oxidized system, which is apparently

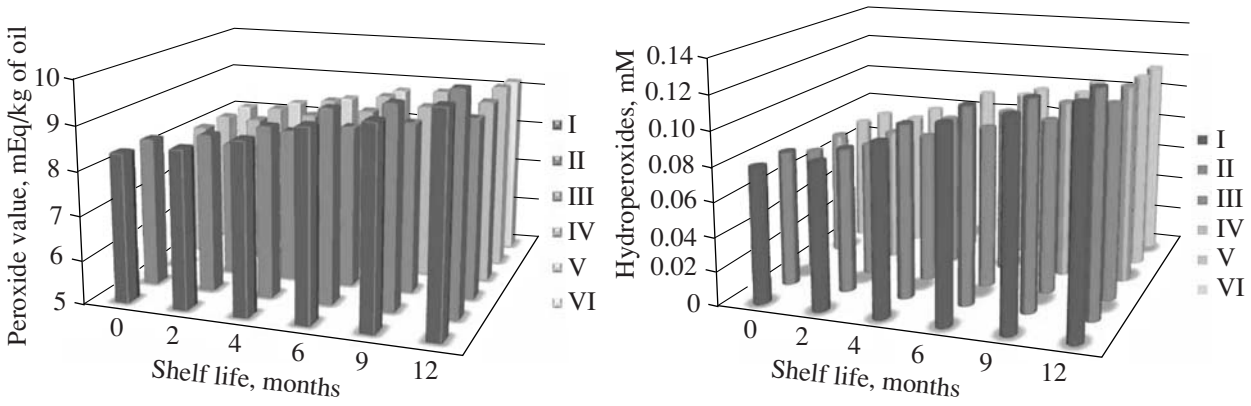

Fig. 2. The dynamics of the accumulation of peroxides and hydroperoxides in the compared oil samples during storage. I—oil without iodine and spice plant extracts; II—oil with an iodine content (1 μg I/ml); and III, IV, V, and VI—oils with an iodine content (1 μg I/ml) and with spice plant extracts (parsley, fennel, thyme, and lovage, respectively).

determined by the properties of the system itself and also by the presence of various spice plant components that slow down the processes of oxidative oil destruction.

Since the samples from the oil group with an iodine content (1 μg I/ml) and with spice plant extracts differ from the oil samples without and with an iodine content (1 μg I/ml) only by containing the antioxidative spice plant components, the difference in the time necessary to achieve a constant value of the peroxide accumulation in the investigated samples is determined to a greater extent by this factor. It is probable that a greater part of the antioxidative spice plant components contained in the oils with spice plant extracts is spent within 6 months of storage, after which these samples are oxidized analogously to the oil samples without spice plant extracts.

It was ascertained based on the obtained results that the increase in the shelf life of the oil group with the iodine content (1 μg I/ml) and with the spice plant extracts was achieved due to the lower rate of the accumulation of peroxides and hydroperoxides in the investigated oils in the first months of storage.

Peroxide and hydroperoxide compounds are known to be unstable. They decompose in the storage process with the formation of the secondary products of vegetable oil oxidation, more stable carbonyl compounds—aldehydes, ketones, and their derivatives with carbonic chains of various lengths.

Table 2. The dynamics of the accumulation of peroxides and hydroperoxides in the compared oil samples

Shelf life, months	Oil without iodine and spice plant extracts		Oil with an iodine content (1 μg I/ml)		Oil with an iodine content (1 μg I/ml) and parsley extract		Oil with an iodine content (1 μg I/ml) and fennel extract		Oil with an iodine content (1 μg I/ml) and thyme extract		Oil with an iodine content (1 μg I/ml) and lovage extract	
	Peroxides, mEq/kg of oil	Hydroperoxides, mM	Peroxides, mEq/kg of oil	Hydroperoxides, mM	Peroxides, mEq/kg of oil	Hydroperoxides, mM	Peroxides, mEq/kg of oil	Hydroperoxides, mM	Peroxides, mEq/kg of oil	Hydroperoxides, mM	Peroxides, mEq/kg of oil	Hydroperoxides, mM
0	8.4 ± 0.1	0.079 ± 0.004	8.4 ± 0.1	0.079 ± 0.003	7.8 ± 0.2	0.071 ± 0.004	8.1 ± 0.1	0.073 ± 0.003	8.1 ± 0.1	0.074 ± 0.005	8.1 ± 0.1	0.072 ± 0.003
2	8.6 ± 0.2	0.085 ± 0.003	8.6 ± 0.2	0.084 ± 0.006	8.1 ± 0.2	0.078 ± 0.003	8.4 ± 0.1	0.078 ± 0.005	8.4 ± 0.1	0.079 ± 0.003	8.3 ± 0.1	0.078 ± 0.004
4	8.9 ± 0.1	0.099 ± 0.007	8.9 ± 0.2	0.101 ± 0.004	8.5 ± 0.1	0.086 ± 0.006	8.6 ± 0.1	0.089 ± 0.004	8.7 ± 0.1	0.088 ± 0.008	8.5 ± 0.1	0.091 ± 0.005
6	9.3 ± 0.1	0.112 ± 0.004	9.4 ± 0.1	0.114 ± 0.005	8.7 ± 0.1	0.094 ± 0.005	8.8 ± 0.1	0.096 ± 0.006	8.9 ± 0.2	0.099 ± 0.009	8.8 ± 0.2	0.096 ± 0.004
9	9.5 ± 0.1	0.119 ± 0.005	9.6 ± 0.1	0.121 ± 0.003	8.9 ± 0.1	0.101 ± 0.003	9.0 ± 0.2	0.104 ± 0.004	9.1 ± 0.2	0.103 ± 0.003	9.0 ± 0.1	0.103 ± 0.005
12	9.9 ± 0.2	0.128 ± 0.007	10.0 ± 0.1	0.129 ± 0.003	9.1 ± 0.2	0.113 ± 0.003	9.2 ± 0.2	0.116 ± 0.004	9.3 ± 0.2	0.115 ± 0.006	9.2 ± 0.1	0.114 ± 0.006

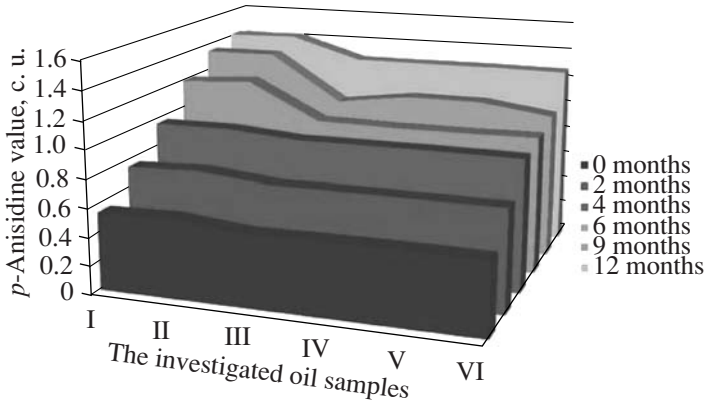

Fig. 3. The change of the *p*-anisidine value in the compared oil samples during storage. I—oil without iodine and spice plant extracts; II—oil with an iodine content (1 μg I/ml); and III, IV, V, and VI—oils with an iodine content (1 μg I/ml) and with spice plant extracts (parsley, fennel, thyme, and lovage, respectively).

If peroxides and hydroperoxides do not exert an influence on the change in the organoleptic indices of oils, aldehydes and ketones that form at the following stages of oxidation are carriers of an unpleasant taste and smell of oxidized vegetable oil.

Figure 3 shows the kinetics of the change in the intensity of the accumulation of such aldehydes as 2,4-decadienal and 2-octenal in the compared vegetable oils, which is expressed by the amount of the *p*-anisidine value.

It was ascertained that the quantity of aldehydes that accumulated in the first four months of storage did not essentially differ for all the investigated samples from the corresponding indices of the compared samples, varying from 0.5123 to 0.5492 c. u. (in fresh samples) and from 0.9331 to 0.9714 c. u. (after four months of storage). It is probable that the processes of the formation and accumulation of the secondary oxidation products (aldehydes) in the vegetable oil samples did not take place intensively in the first months of their storage, which is likely to be determined by the properties of the system itself.

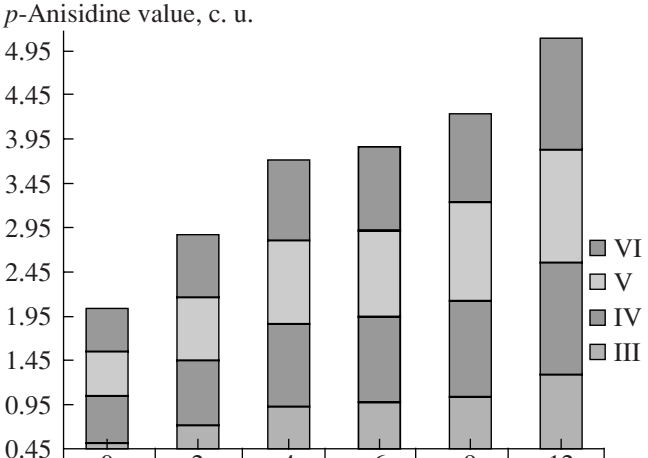

	0 months	2 months	4 months	6 months	9 months	12 months
VI	0.5179	0.9343	1.0353	1.7241	0.9793	1.2791
V	0.5219	0.9371	1.1043	1.7251	0.9723	1.2834
IV	0.5203	0.9359	1.1021	1.7261	0.9704	1.2807
III	0.5123	0.9331	1.0341	1.7232	0.9786	1.2786

Fig. 4. The influence of antioxidative spice plant components on the storage stability of the compared oils with an iodine content (1 μg I/ml): III—parsley; IV—fennel; V—thyme; VI—lovage.

The incorporation of the spice plant extracts in the composition of the oils with the iodine content of 1 μg I/ml exerts an effective influence on the processes of stabilization of the investigated oils. Thus, the *p*-anisidine value of the oil without iodine and spice plant extracts came to 1.4216 c. u. after 12 months of its storage, and this value of the oils with the iodine content and spice plant extracts decreased and varied from 1.2786 to 1.2834 c. u.

When comparing the antioxidative properties of the spice plant extracts (parsley, fennel, thyme, and lovage) incorporated into the oil samples, one should note that the antioxidative components of the parsley and lovage extracts exert the greatest influence on inhibiting the processes of oil oxidation (Fig. 4).

This regularity is also traced for the acid and peroxide values of the corresponding oil samples. The greater stability of the oils with the parsley and lovage spice plant extracts can be explained by the more effective stabilizing action of the antioxidative components of these spice plants.

CONCLUSIONS

1. The technology has been developed for obtaining iodine-fortified oil with antioxidative properties that are due to the antioxidative spice plant components contained in this oil. The stable iodine-fortified oil with the prophylactic action can be used as a salad dressing

with the view of imparting a pleasant specific aroma of spice plants to various cold courses and snacks.

2. The processes have been studied of the formation and accumulation of the primary oxidation products in the investigated oil samples. The following has been ascertained:

—The accumulation of free fatty acids in the oil group with the iodine content (1 μg I/ml) and with spice plant extracts runs less intensively after 12 months of storage, being within the range of 0.291–0.294 mg KOH/g of oil; meanwhile, the acid value of the oil sample without iodine came to 0.315 mg KOH/g of oil.

—The summary rate of the oxidative reactions that lead to the formation of peroxides and hydroperoxides during storage is lower for the stable oil group with the iodine content (1 μg I/ml) than for the oil without the iodine and spice plant extracts and the oil group with the iodine content (1 μg I/ml) and without the spice plant extracts.

3. The incorporation of the spice plant extracts into the composition of the oils with the iodine content (1 μg I/ml) exerts an effective influence on the processes of stabilization of the investigated oils; i.e., it inhibits the intensity of the accumulation of the secondary oxidation products in the compared oil samples.

REFERENCES

1. Assessment of Iodine Deficiency Disorders and Monitoring Their Elimination: A Guide for Program Managers, ICCIDD, UNICEF, WHO, Sec. Ed., 2005.
2. Review of Progress towards Sustainable Elimination of Iodine Deficiency in Thailand, ICCIDD, UNICEF, 2004.
3. Monitoring Universal Salt Iodization Programes. UNICEF/PAMM/ICCIDD/WHO, 2005, p. 100.
4. Pandav, C., Worthwhile Investment in Health. Economic Evaluation of IDDs Control Program in Skim. Delhi: Oxford University Press, 2007.
5. Progress towards the Elimination of Iodine Deficiency Disorders (IDD), WHO, UNICEF and ICCIDD, *WHO/Euro/NUT/*, 2006.
6. Hotăarâre cu privire la aprobarea programului naţional de eradicare a tulburarilor prin deficit de iod pina in anul 2010, Monitorul official al RM, 1 iunie 2007.
7. Starea de nutritie in Republica Moldova. Raport UNICEF, 1996–2000, p. 38.
8. Conferinţa "Deficienţa de vitamine şi minerale. Evaluarea prejudicilor şi auditul protecţiei pentru Moldova 2006. Scurtă expunere pentru factori de deciuie", Chişinău, Decembrie 2006.
9. Conferinţa Naţionala de Nutriţie, Republica Moldova, Chişinău, 28 iunie 2007.
10. Alimentaţia şi nutriţia umană în Republica Moldova. Constatări şi recomandări, UNICEF, Biroul pentru Moldova, 2000.
11. Abraham, B., Webb, K.L., Interim Evaluation of the Voluntary Iodine Fortification Program. Canberra: Australian Food and Nutrition Monitoring Unit, Commonwealth of Australia, 2006.
12. Food Standards Australia New Zealand. 2004a. Initial Assessment Report - Proposal P230 Iodine Fortification, Canberra: FSANZ.
13. Honein, M.A., Paulozzi, L.J, Mathews, T.J et al., Impact of Iodine Fortification of the US Food Supply on the Occurrence of Neural Tube Defects, *JAMA 285:2981–2986*, 2006.
14. Liu, S., West, R., Randell, E., Longerich, L., O'Connor, K. S., Scott, H., Crowley, M., Lam, A., Prabhakaran, V., McCourt, C., A Comprehensive Evaluation of Food Fortification with Iodine, *BMC Pregnancy and Childbirth 4:20*, 2006.
15. Ray, J G., Iodine Food Fortification in Canada, *Nutrition Review 62:S35*, 2006.
16. Stanley, F., Eastman, C, Mann, J., Binns, C., The Effectiveness of Mandatory Fortification as a Public Health Strategy to Increase Nutrient Intakes with Reference to Iodine and Folate, 2005, p. 24.
17. Winger, R.J., Koening, J., Je Lee, S. Wham and House, D.A., Technological Issues with Iodine Fortification of Foods, *Final Report for New Zealand Food Safety Authority*, 2005.
18. Budagyan, F.E. and Smirnova, L.I., The Influence of Phenol Antioxidants on Assimilability of Melted Pig Fat, *Voprosy pitaniya*, 2005, vol. 21, no 2, pp. 47–50.
19. Bukhman, N.D., The Influence of Antioxidant on Nutritive Value of Fat, *Voprosy Pitaniya*, 2006, vol. 21, no 1, pp. 68–72.
20. Faria, J.A.F., A Gas Chromatographic Reactor for Measuring the Effectiveness of Antioxidants for Polyunsaturated Lipids, *J. Amer. Oil Chem. Soc.*, 2005, vol. 59, no 12, pp. 533–535.
21. Lillard, D.A., Chemical Changes Involved in the Oxidation of Lipids in Foods, in *Lipids as a Source of Flavour*, Washington, 2005, pp. 68–80.
22. Denisov, E.T., *Konstanty skorosti gomologicheskikh zhidkofaznykh reaktsii* (Rate Constants of Homologous Liquid-Phase Reactions), Moscow: Nauka, 1995, p. 711.
23. Gagarina, A.B., Pisarenko, L.M., and Emanuel, N.M., Kinetic Characteristic of Inhibiting Action of 2-Phenyldandione-1,3 in Chain Oxidation Process, *Dokl. AN SSSR*, 1987, vol. 212, no 3, pp. 653–656.
24. Moiseev, V.V. and Poluektov, I.T., 2-Aryldandiones-1,3: a New Class of Radical-Active Compounds, *Uspekhi Khimii*, 1994, vol. 48, no 3, pp. 471–491.
25. Cornell, D.G., Nielbiss, E.D., and Pallansch, M.J., Partition Coefficients of Some Antioxidants in Butter Oil–Water Model Systems, *J. Dairy Sci*, 2007, vol. 53, no 11, pp. 529–535.
26. Effectiveness in Intermediate Moisture Content Model Systems, *J. Food. Sci.*, 2006, vol. 39, no 3, pp. 479–483.
27. *Spravochnik po rastvorimosti* (Solubility Reference Book), Moscow-Leningrad: AN SSSR, 1967, vol. 1, p. 1870.
28. GOST 26593-85: Method for Determining Peroxide Value of Edible Oils and Fats.
29. Shanta, N.C. and Decker, E.A., Rapid, Sensitive, Iron-Based Spectrophotometric Methods for Determination of Peroxides Values of Food Lipids, *J. AOAC*, 1994, 77, pp. 421–424.

30. IUPAC, Standard Methods for the Analysis of Oils, Fats and Derivatives., *Method Number 2.504*, 7*th ed*., Determination of the *p*-Anisidine Value (*p*-A/V.), *Blackwell Scientific Publications*, Boston, MA and Oxford, UK, 1987.
31. Bird, R.P. and Draper, H.H., Comparative Studies on Different Methods of Malonaldehyde Determination, *Methods Enzymol.*, 1984, 105, pp. 184–191.
32. Snedecor, G.W. and Cochran, C.W., Statistical methods, *Ames*, IA, 8*th ed*., Iowa State University Press, 1989, pp. 343–438.
33. Popovici, C., Haritonov, S., Deseatnicov, O., Sturza, R., Study of the Incorporation of Iodine in Vegetal Oils, *Journal of the University of Chemical Technology and Metallurgy*, Bulgaria: UCTM, 2006, vol. 41, no 4, pp. 449–456, ISSN 1311-7629.
34. Deseatnicov, O., Sturza, R., Haritonov, S., Popovici, C., Issledovanie fizico-himicheskih svoistv obogashennogo iodom podsolnechnogo masla, *Elektron. Obrab. Mater.*, 2006, no 4, pp. 73–78, ISSN 0013-5739.
35. Sturza, R., Deseatnicov, O., Popovici, C., Brevet de invenție. Procedeu de obținere a uleiului de fioarea-soarelui cu valoare biologică sporită. Nr. Hotărârii de acordare 5111 din 2007.04.12, Nr. depozit: a 2006 0186.
36. STAS 1129- 93, Ulei de fioarea soarelui. Condiții tehnice.

ISSN 1068-3755, Surface Engineering and Applied Electrochemistry, 2008, Vol. 44, No. 5, pp. 422–423. © Allerton Press, Inc., 2008.
Original Russian Text © F.P. Grosu, M.K. Bologa, 2008, published in Elektronnaya Obrabotka Materialov, 2008, No. 5, pp. 93–95.

INFORMATION

About the Monograph by A.I. Grigor'ev Entitled "Ball Lightning"

F. P. Grosu and M. K. Bologa

DOI: 10.3103/S1068375508050141

The monograph is devoted to the problem of ball lightning, which unites numerous other concepts embracing the whole spectrum of physical phenomena connected with electrical storm discharges and, possibly, those of other so far not fully understood nature.

According to many observations and physical conceptions, ball lightning (BL) originates from the plasma bunches of common streak lightning (SL), and, hence, at the moment of outbreak, the BL temperature may be dozens or even hundreds of thousands of degrees, as that of streak lightning. Then, while cooling, it may acquire a temperature comparable with that of room conditions in the quite common cases when it gets indoors and "behaves peacefully," i.e., causes no burns, fires, or other disasters. This temperature range of electrical discharge bunches has not been embraced yet in laboratory conditions, not to mention BL's extraordinary stability, whose lifetime may exceed dozens of seconds, which is many times longer than in the physical experiments of its modeling.

The enigmatic forms of BL manifestation, i.e., St. Elmo's fire (SEF)[1]; tomb or marsh lights; and its ability to penetrate through windowpanes without making holes or switch on electric bulbs, etc., point to its extreme complexity, which is one of the reasons why the BL phenomenon still remains mysterious and unexplored.

On the other hand, one cannot generate adequate BLs under laboratory conditions, which further impedes its exploration. In this situation, the only possibility of "approaching" the object of research is targeted natural observations and (or) results of surveys of BL eye witnesses.

However, in these conditions, there is a need for systematizing the statistical data according to qualitative and quantitative features, for making so-called "zero hypotheses" about their distribution laws, for criterion checkups, etc. It is only at first glance that the BL problems may seem idle. They were the object of research of highly prominent scientists and Nobel Prize winners, for example, in the USSR—Academician P.L. Kapitsa.

We think that the author of the reviewed monograph, professor A.I. Grigor'ev, a well-known physicist in many fields and, first of all, electrical discharges and the stability of electric systems similar to BL, is fully aware of the complexity of the undertaken research because he is rather cautious in proposing his own BL models. Instead, he conducts statistical systematization and processing of BL observation data with appropriate physical comments supported with mathematical calculations. The author writes that "the physical issues of BL are more generally formulated and the list of these issues is expanded." To achieve the set aims, he has collected over six thousand descriptions and observations of BL. He points directly or indirectly to which line of physical research one should follow.

The book consists of a foreword, seven chapters, an afterword, and bibliographical references (53 titles).

In the foreword, the author notes that "following the example of the most prominent French physicist Francois Arago," who named this type of atmospheric electrical discharge ball lightning, BL got in sight of science without losing its the status of an obscure natural phenomenon."

The author states that, since the existing "average portraits" of BL are quite far from the original, whose characteristic feature is extreme variability of properties, attempts at BL physical modeling are doomed to failure. Therefore, the monograph cites numerous BL descriptions in natural conditions and focuses on BL properties not included into the standard average portraits.

The first chapter entitled "Common Ball Lightning" is devoted to observations in natural conditions. It cites the data of 16 BL descriptions by size, shape, color, brightness, and lifespan. These data have been "translated" into the language of mathematics as formulae, graphs, polygons, or observation frequency histograms for this or that property by geographical areas of the USSR and the Netherlands. It is shown that the statistical distributions are close to that of Wolf numbers.

The second chapter is focused on the issues related to BL origination according to the results of 51 descriptions. The data are systematized in the form of tables from which one can clearly see the general picture of BL birth circumstances. According to 1138 descriptions, in 66% of cases, BL appears on metal conductors. In streak lightning channels, it appears in ~8% of cases; at the spot of SL strokes, in ~8% of cases; and, in clouds, in ~4% of cases. In other cases (~14%), one simply recorded an outbreak of BL.

[1] SEF appears on ship's masts, church crosses, tree branches, etc., in stormy weather as a result of corona discharge. In contrast to BL, its physical nature has been explained.

Summing up the results of this section, the author notes that:

> … despite the outward dissimilarity of outbreaks in streak lightning channels, in clouds, and on metal conductors, it seems fairly obvious that the act of BL birth is based on this or that form of electrical discharge in the atmosphere. In the first case, one simply has to deal with a known form of discharge and a well-studied plasma state of a substance as, for example, in the case of BL birth in a discharge channel or at the spot of a streak lightning stroke and in the other cases with a non-standard and unexplored discharge form as in the case of a BL outbreak on sockets, telephones, loudspeakers, or other unusual situations.

The third chapter is devoted to the "End of BL Life." The respective information on 5128 descriptions systematized in the form of a table shows that most often BL "leaves the field of vision" in about 40% of cases. In approximately 26% of cases, BL blows up, and, in ~14% of cases, it "goes out quietly." The probability shares of other cases of BL "decease" are relatively small: it "went to the Earth in ~8% of cases," "went down onto the conductor in ~6%," "broke up into sparks in ~5%," and "provoked blow up in ~1%."

The chapter gives detailed stories of the eye witnesses of each of the seven listed possibilities of BL dying out; in particular, it describes the cases when BL disappears with a slight clap as well as cases of explosions causing serious damage.

The fourth chapter entitled "Windowpanes are Not Obstacles for BL" appears to be the most "intriguing." It cites descriptions of unbelievable cases when, penetrating through a windowpane, BL makes no holes in the pane. For example, "…no holes were left in the windowpane that the ball went through…" or "…a glowing ball went into the room directly through the pane of the closed window … and disappeared with a deafening bang…"

Summing up the results of this chapter, the author of the book notes that the question about the physical mechanism of BL penetration through panes without damaging them is still unanswered. It is absolutely obvious that the possibility of answering this question is closely connected with identifying the nature of the substance that BL consists of. If one manages to establish that the main element of the BL structure is electrical and magnetic fields or their combinations and BL glow is explained only by the reaction of the gas medium to the existence of these fields, then this will remove the problem of BL penetration through panes.

Now we can only asks ourselves the following questions: "What is there inside BL that provides for its stability? What is the structure of this type of electricity?" These issues are the focus of the fifth chapter entitled "Some BL Properties," whose first section is entitled A Glance Inside BL.

According to many descriptions, inside BL there are sparkling dots, balls, strings, etc. Sometimes one gets an impression that BL consists of numerous "balls," and this could be an extremely fascinating hypothesis. However, the existing hypotheses as to the structure of BL cannot embrace and explain the whole spectrum of its physical properties.

The same chapter considers the questions of BL radiation. According to 588 descriptions out of 2070, in most cases, BL radiated no heat (~15% of cases). In ~6% of cases, it caused burning of inflammable substances; in 3%, it radiated heat; in 2%, it caused fire; and, in 1%, it caused burns among the witnesses.

A more interesting and exotic property of BL is its capability of emitting electromagnetic waves in the microwave and radio wave regions. This is interesting because it enables one to make certain conclusions about its structure, because the length of the studied wave may enable one to judge about the charges and other physical properties of the emitting particles. The book contains descriptions of BL affecting the operation of radio sets; however, these data are insufficient to affirm with certainty that BL emits in the radio region. At the same time, according to a great number data sources, BL is electrically charged. The author also describes other, more exotic BL properties, for example, "…it does not drown in water and burn in fire." BL can sometimes be confused with St. Elmo's fire (SEFs) as well as with other types of lights. In this view, the author devoted a whole chapter—the sixth one—to SEF and its features in common with and distinct from BL. Some people describes cases when SEF appears on rifle bayonets in the form of cold flame tips in contrast to BL.

This chapter cites histograms, tables, and photographs, which show the explicit differences between SEF and BL. This differentiation is very important for creating an adequate physical model of BL. To avoid confusion, the author considers other forms of lights that are completely unusual, for example, those over tombs or marshes, and gives physical explanations for these phenomena so that they are not confused with BL.

The seventh and closing chapter is devoted, as follows from its very title "Emotions, Statistics, and Mistakes of BL Observers," to the human factor and the errors of the average statistical data on BL and the correlations between its individual properties. At the end of the chapter, the author warns the reader "be prepared for meeting with BL" hinting both at its dangerousness and giving precautions and suggesting correct behavior in the case of a possible meeting.

It is difficult to fully state on a few pages all the advantages and possible drawbacks of the reviewed book, but, in conclusion, we can say that its publication is an important event not only in the physics of ball lightning, electrical discharges, and plasma states but also in physics in general.

The book will act as an excellent springboard for those who wish to seriously work in the field of plasma and ball lightning physics. The book is written in quite comprehensible and, at the same time, academic language. In some places, it is read as fiction written by a well-known physicist–theoretician. All honor to him.